

Voice communication system for a spacesuit simulator

Design and performance estimation of the system with
additional analysis of the usability on Mars

Omar Filip El Sendiouny

A thesis presented for the degree of
Bachelor of Science



Vienna University of Technology
The Faculty of Electrical Engineering and Information Technology
Institute of Telecommunications

supervised by
Univ.Prof. Ing. Dipl.-Ing. Dr.-Ing. Christoph Mecklenbräuker

reviewed by
Mag.rer.nat. Dr.rer.nat. Gernot Grömer

Vienna, April 2021

Voice communication system for a spacesuit simulator

Design and performance estimation of the system with additional analysis of the usability on Mars

Omar Filip El Sendiouny

Abstract

In this thesis, a voice communication system with an associated self-sufficient energy distribution system for a spacesuit simulator is designed and its performance is examined. For this purpose, the plane earth signal budget is used to show that the minimum fade margin of the voice communication system is sufficiently large to meet the range requirements and a **MATLAB** simulation is developed which estimates the daily electrical energy yield of the self-sufficient energy distribution system for different mission locations on Earth. The latter is based on the angular relationships between the Sun and Earth, a model of a PV generator and a model of a LiFePO₄ battery. The performance estimation of the voice communication system has shown that a sufficiently large fade margin could be achieved if a repeater radio infrastructure is used. Regarding the self-sufficient energy distribution system, the developed **MATLAB** simulation showed that it can be used to supply the repeater radio infrastructure for different mission locations on Earth when sufficient solar radiation is available. In addition, this thesis examines how the designed system must be adapted so that it can be used on the surface of Mars. Investigations showed, that the Martian Ionosphere can be used as a reflector for electromagnetic waves in the very high frequency band during the day. Thus allowing global communication. Another important finding of this investigation was that the temperature dependence of the electrical devices involved must not be neglected if such a system is to be planned for Mars.

Dedication

To my grandfather, in loving memory.

Declaration

I declare that the work in this bachelor thesis titled “Voice communication system for a spacesuit simulator” has been carried out by me at the Vienna University of Technology in the Faculty of Electrical Engineering and Information Technology at the Department of Telecommunications. The information derived from the literature has been duly acknowledged in the text and a list of references provided. No part of this bachelor thesis was previously presented for another degree or diploma at this or any other institution.

Omar Filip El Sendiouny

Date

Acknowledgements

I would like to sincerely thank Christoph Mecklenbräuker and Gernot Grömer for making this thesis possible and giving me the opportunity to become part of such an fascinating project.

I would also like to thank Javier Roldán, Sebastian Sams, Michael Müller and Matthias Mair for allowing me to work alongside them on this project. I was able to learn a lot through their experience and expertise.

My thanks also go to Sophie Gruber, Franziska Usel and Nadja Keplinger who supported us in a number of organizational tasks related to the project.

Furthermore I would like to thank Benedikt Stingl, Nina Sejkora, Stefanie Gar-nitschnig and all other colleagues from the OeWF Suit-laboratory in Innsbruck, who welcomed me with open arms from the first day of my arrival.

Finally, I want to thank the sponsors and supporters of this project Robert Neumann, Markus Neuner and Maria Holzknecht.

Contents

List of Figures	VIII
List of Tables	XII
Listings	XIV
Abbreviations	XV
Symbols	XVII
1 Introduction	1
1.1 About the thesis	1
1.1.1 Motivation	1
1.1.2 Backup voice communication system	2
1.2 Aim	3
1.2.1 Literature review	3
1.2.2 Deliverables	3
1.2.3 Thesis Structure	5
2 Methodology	7
2.1 Electrical energy distribution	7
2.2 Wind energy	8
2.3 Solar energy	9
2.3.1 Angular relationships	11
2.3.2 Solar irradiation on the Earth's surface	13
2.3.3 Photovoltaic energy yield	15
2.3.4 Photovoltaic generator alignment	18
2.3.5 Modeling the solar energy curve	20
2.3.6 Photovoltaic generators	22
2.3.7 MPP tracking solar charging controllers	27
2.3.8 Electrochemical energy storage	29
2.3.9 Cable losses	37
2.3.10 Martian application	38
2.4 Voice communication system	41
2.4.1 Load for the electrical energy distribution	41
2.4.2 Free space signal budget	42
2.4.3 Plane earth signal budget	44
2.4.4 Martian application	45

3 Results	47
3.1 System design	47
3.1.1 Base station radio infrastructure	49
3.1.2 Repeater radio infrastructure	53
3.1.3 Serenity radio system	55
3.1.4 Safety officer radio	57
3.1.5 On-site support crew radio	57
3.2 Link budget estimation	58
3.2.1 Communication links and fade margin	59
3.2.2 Additional coverage area around the base station	60
3.3 Self-sufficient energy distribution system	61
3.3.1 Photovoltaic generator model	61
3.3.2 LiFePO₄ battery model	67
3.3.3 Performance estimation	72
4 Conclusion and critical reflection	81
4.1 Conclusion	81
4.1.1 Voice communication system	81
4.1.2 Self-sufficient energy distribution system	82
4.1.3 Martian application	82
4.2 Critical refelction	83
4.2.1 Voice communication system	83
4.2.2 Self-sufficient energy distribution system	84
A Austrian Space Forum	A1
A.1 History	A1
A.2 Serenity spacesuit simulator	A3
B Mathematical basics	A4
B.1 Integral of the Gaussian bell curve	A4
B.2 Newton-Raphson method	A6
C MATLAB and MAPLE source codes	A8
C.1 MATLAB simulation of the self-sufficient energy distribution system .	A8
C.2 MAPLE source code for the Jacobian matrix	A21
References	R1

List of Figures

1.1	Part one of the flowchart of this thesis. It illustrates which steps were taken in order to achieve the deliverables.	4
1.2	Part two of the flowchart of this thesis. It illustrates which steps were taken in order to achieve the deliverables.	5
2.1	Turbine that converts kinetic energy from wind into electrical energy. The dashed circle represents the area A_W that is perpendicular to a flowing gas.	8
2.2	Angular relationship between the Sun and Earth. (Recreated from: [11])	9
2.3	Basic structure of an electrical stand-alone system which is supplied with electrical energy by a photovoltaic generator. The energy is stored in an electrochemical energy storage device.	10
2.4	Angular relationship of the Sun's altitude γ_S and azimuth α_S with the corresponding celestial hemisphere of an observer. In this figure the Sun already passed the solar noon. (Recreated from: [11])	12
2.5	Solar resource map of the long term average global horizontal irradiation of Austria. (Image credit: [28], [34])	14
2.6	Solar resource map of the long term average direct normal irradiation of Austria. (Image credit: [28], [34])	15
2.7	Solar radiation on an inclined photovoltaic generator with the angle β . (Recreated from: [11])	16
2.8	Illustration of the incidence angle θ of the solar rays with respect to the normal to A_{PV} . (Recreated from: [18])	16
2.9	Illustration of the latitude φ_Z on Earth at which the Sun is at its zenith for $t_S = 12h$. By comparing the latitude of the installation site of a photovoltaic generator it can be determined how it must be aligned, so that the electrical energy yield can be maximized.	20
2.10	Model of the Sun's radiation flux Φ_G onto the energy-converting area of a photovoltaic generator as a Gaussian function of the solar time t_S . It is assumed that the Sun's irradiance is symmetrical around solar noon, and that the photovoltaic generator is aligned so that its energy-converting area is perpendicular to the Sun's rays at solar noon.	20
2.11	Electrical equivalent circuit of a photovoltaic generator. It consists of N_C photovoltaic cells connected in series. (Recreated from: [11]) . .	22
2.12	Simplified standard model of a photovoltaic cell. (Recreated from: [11], [13])	23

2.13	Modeled current-voltage characteristic of a photovoltaic generator, depending on the radiation flux Φ_G and the photovoltaic cell temperature ϑ_C . (Recreated from: [11], [13])	24
2.14	Monthly averages of temperature and precipitation data for the Hohe Warte in Vienna, Austria. (Image credit: [54])	27
2.15	Electrical power output of a photovoltaic generator as a function of U_{PV} . It is further dependent on the photovoltaic cell temperature ϑ_C and the radiation flux Φ_G . (Recreated from: [11])	28
2.16	The basic structure of a maximum power point tracking solar charging controller. (Recreated from: [11])	29
2.17	R_{int} model of a LiFePO ₄ battery (electrochemical energy storage device). (Recreated from: [61], [67])	31
2.18	Typical behavior of the open-circuit voltage U_0 of a LiFePO ₄ battery depending on the SOC. SOC ₁ to SOC _{N_{MP}} represent the measuring points for the discharging and charging experiment. (Recreated from: [11], [14], [60]–[62])	32
2.19	Behavior of the battery voltage $U_B(t)$ when it is first discharged with I_D and then charged with I_C . From the resulting voltage drop $\Delta U_D(t_{D,on})$ and voltage rise $\Delta U_C(t_{C,on})$, the R_{int} model's electrolyte resistances $R_{e,D}$ and $R_{e,C}$ can be calculated. The turquoise curve represents the behavior of the modeled battery voltage. (Recreated from: [15], [60], [62], [65]–[67], [69])	33
2.20	Measurement setup for the discharge experiment.	34
2.21	An example of the behavior the battery voltage $U_B(t)$, battery current $I_B(t)$ and battery charge $Q_B(t)$ of a LiFePO ₄ battery when it is charged with a constant current I_C and then with a constant voltage U_{full} over a longer period of time. At $t_C + t_V$ the battery charger switches from U_{full} to U_{float} to keep the battery in a fully charged state. (Recreated from: [14], [70], [71])	35
2.22	Measurement setup for the charge experiment.	36
2.23	<i>“Diurnal variation of global G_h, beam G_{bh} and diffuse G_{dh} irradiance on a horizontal Mars surface at Viking Lander VL1.”</i> (Image and caption credit: [16])	38
2.24	<i>“Diurnal variation of global G_h, beam G_{bh} and diffuse G_{dh} irradiance on a horizontal Mars surface at Viking Lander VL1.”</i> (Image and caption credit: [16])	39
2.25	<i>“Diurnal variation of global G_h, beam G_{bh} and diffuse G_{dh} irradiance on a horizontal Mars surface at Viking Lander VL1.”</i> (Image and caption credit: [16])	39
2.26	Illustration of the plane earth signal budget. (Recreated from: [2], [5], [6])	44
3.1	Proposed topology for the designed voice communication system.	47
3.2	Top view of the mission area covered by the voice communication system.	48
3.3	Schematic structure of the base station radio infrastructure.	49

3.4 Attenuation of the Messi & Paoloni Ultraflex 7 coaxial cable for 20°C. For the frequency $f_{\sim} = 158,950\text{MHz}$, the attenuation is around 7,2471dB/100m. (Recreated from: [80])	52
3.5 Schematic structure of the self-sufficient energy distribution system of the repeater radio infrastructure.	53
3.6 Schematic structure of repeater radio infrastructure.	54
3.7 Schematic structure of the Serenity radio system.	55
3.8 Anthropometric dimensional data for the american female and male. (Image and caption credit: [82], [85])	57
3.9 Modeled current-voltage characteristic of the AE Solar AE195SMM6-36 PV generator, depending on the total irradiance onto its inclined surface E_G . The PV cell temperature $\vartheta_C = 25^\circ\text{C}$ is assumed to be constant.	63
3.10 Modeled current-voltage characteristic of the DAS Energy DAS145PF PV generator, depending on the total irradiance onto its inclined surface E_G . The PV cell temperature $\vartheta_C = 25^\circ\text{C}$ is assumed to be constant.	63
3.11 Modeled power-voltage characteristic of the AE Solar AE195SMM6-36 PV generator, depending on the total irradiance onto its inclined surface E_G . The PV cell temperature $\vartheta_C = 25^\circ\text{C}$ is assumed to be constant.	64
3.12 Modeled power-voltage characteristic of the DAS Energy DAS145PF PV generator, depending on the total irradiance onto its inclined surface E_G . The PV cell temperature $\vartheta_C = 25^\circ\text{C}$ is assumed to be constant.	64
3.13 Modeled current-voltage characteristic of the AE Solar AE195SMM6-36 PV generator, depending on its PV cell temperature ϑ_C . The total irradiance onto its inclined surface $E_G = 1000\text{Wm}^{-2}$ is assumed to be constant.	65
3.14 Modeled current-voltage characteristic of the DAS Energy DAS145PF PV generator, depending on its PV cell temperature ϑ_C . The total irradiance onto its inclined surface $E_G = 1000\text{Wm}^{-2}$ is assumed to be constant.	65
3.15 Modeled power-voltage characteristic of the AE Solar AE195SMM6-36 PV generator, depending on its PV cell temperature ϑ_C . The total irradiance onto its inclined surface $E_G = 1000\text{Wm}^{-2}$ is assumed to be constant.	66
3.16 Modeled power-voltage characteristic of the DAS Energy DAS145PF PV generator, depending on its PV cell temperature ϑ_C . The total irradiance onto its inclined surface $E_G = 1000\text{Wm}^{-2}$ is assumed to be constant.	66
3.17 Recorded time courses of $U_B(t)$ and $I_D(t)$ during the discharging experiment for $\text{SOC}_n = 0, 50$. The device under test was the Offgridtec Smart-Pro 12,8V 50Ah LiFePO ₄ battery.	69
3.18 Recorded time courses of $U_B(t)$ and $I_C(t)$ during the charging experiment for $\text{SOC}_n = 0, 50$. The device under test was the Offgridtec Smart-Pro 12,8V 50Ah LiFePO ₄ battery.	69

3.19	Open-circuit voltages $U_{0,C}(\text{SOC}_n)$, $U_0(\text{SOC}_n)$ and $U_{0,D}(\text{SOC}_n)$ obtained from the discharging and charging experiment carried out on the Offgridtec Smart-Pro 12,8V 50Ah LiFePO ₄ battery.	70
3.20	Electrolyte resistances $R_{e,D}(\text{SOC}_n)$ and $R_{e,C}(\text{SOC}_n)$ obtained from the discharging and charging experiment carried out on the Offgridtec Smart-Pro 12,8V 50Ah LiFePO ₄ battery.	71
3.21	Time course of $I_C(t)$ over time during the CV charging phase of the Mean Well ENC-180-12 battery charger. The charged device was the Offgridtec Smart-Pro 12,8V 50Ah LiFePO ₄ battery.	71
3.22	Monthly averages of temperature and precipitation data for Mitzpe Ramon, Southern District, Israel (Negev Desert). (Image credit: [54])	74
3.23	Solar resource map of the long term average global horizontal irradiation of Israel. (Image credit: [28], [34])	79
3.24	Solar resource map of the long term average direct normal irradiation of Israel. (Image credit: [28], [34])	80
A.1	Visible geological similarities between the Martian surface and an analog Martian environment on Earth.	A2
A.2	Serenity spacesuit simulator design study. (Image credit: OeWF/Bernhard Kaliauer Design Studio)	A3
B.1	Shifted Gauss bell.	A4
B.2	Newton-Raphson method to approximate the zero crossing of a function.	A7

List of Tables

1.1	Requirements for the voice communication systems of the Serenity spacesuit simulator.	2
2.1	Albedo values (refelctivity) for different surfaces [11], [20], [36], [37]. . .	17
2.2	Parameters for the standard test conditions of a photovoltaic generator [11].	24
2.3	Conditions under which the NOCT is measured [11].	26
3.1	Excerpt from the data sheet of the Motorola Mototrbo DM 2600 mobile radio. [75]	50
3.2	Excerpt from the data sheet of the Daiwa CN-501VN cross needle VSWR & power meter.[77]	51
3.3	Excerpt from the data sheet of the Diamond SP1000 lightning arrester. [78]	51
3.4	Excerpt from the data sheet of the Diamond BC-101 VHF fixed station antenna.[79]	51
3.5	Excerpt from the data sheet of the Messi & Poloni Ultraflex 7 coaxial cable. [80]	52
3.6	Excerpt from the data sheet of the Motorola Mototrbo SLR 1000 repeater. [76]	54
3.7	Excerpt from the data sheet of the Motorola Mototrbo SL 2600 handheld radio. [81]	56
3.8	Excerpt from the data sheet of the Motorola Mototrbo DP 3601 handheld radio. [86]	58
3.9	Specifications of the designed voice communication system when all participants transmit at maximum power.	59
3.10	Specifications of the designed voice communication system when all participants are limited to a maximum transmission power of $P_T = 5W$	59
3.11	Results of the plane earth signal budget calculation for the designed voice communication system when all participants transmit at maximum power.	59
3.12	Results of the plane earth signal budget calculation for the designed voice communication system when all participants are limited to a maximum transmission power of $P_T = 5W$	59
3.13	Excerpt from the data sheet of the AE Solar AE195SMM6-36 PV generator at STC [87].	61
3.14	Excerpt from the data sheet of the DAS Energy DAS145PF PV generator at STC [88].	62

3.15 Excerpt from the data sheet of the Offgridtec Smart-Pro 12, 8V 50Ah LiFePO ₄ battery [63].	67
3.16 Laboratory equipment required to carry out the discharging and charging experiment with the Offgridtec Smart-Pro 12, 8V 50Ah LiFePO ₄ battery.	67
3.17 Calculated results from the discharging and charging experiment carried out on the Offgridtec Smart-Pro 12, 8V 50Ah LiFePO ₄ battery.	70
3.18 Excerpt from the user manual of the Victron Energy BlueSolar MPPT 75/10 solar charging controller [90].	72
3.19 Input for the MATLAB simulation of the self-sufficient energy distribution system for the Negev Desert in Israel.	73
3.20 Input for the MATLAB simulation of the self-sufficient energy distribution system for Vienna, Austria.	74

Listings

3.1	Output of the MATLAB simulation in appendix C.1 regarding the installation of the PV generator for the mission inputs in the table 3.19.	75
3.2	Output of the MATLAB simulation in appendix C.1 regarding the daily energy yield of the PV generator for the mission inputs in the table 3.19.	76
3.3	Output of the MATLAB simulation in appendix C.1 regarding the installation of the PV generator for the mission inputs in the table 3.20.	77
3.4	Output of the MATLAB simulation in appendix C.1 regarding the daily energy yield of the PV generator for the mission inputs in the table 3.20.	78

Abbreviations

AA	Analog astronaut
ALB	Albedo
AM	Air mass
BER	Bit error rate
BSt	Base station
CC	Constant current
Ch1	Channel 1
Ch2	Channel 2
CV	Constant voltage
DGI	Direct generator irradiance
DHI	Direct horizontal irradiance
DIFG	Diffuse generator irradiance
DIFH	Diffuse horizontal irradiance
DNI	Direct normal irradiance
EEC	Electrical equivalent circuit
EIRP	Effective isotropic radiated power
EVA	Extravehicular activity
GHI	Global horizontal irradiance
GPS	Global positioning system
HUT	Hard upper torso
IP	Ingress protection
ISO	Isotropic
LOS	Line of sight
MPP	Maximum power point
NASA	National Aeronautics and Space Administration
NOCT	Nominal operating cell temperature
OeWF	Austrian Space Forum

Abbreviations

OPS	Operations
OSS	On-site support
PEPL	Plane earth path loss
PTT	Push-to-talk
PV	Photovoltaic
REP	Repeater
RGI	Reflected generator irradiance
RX	Receiving
SCC	Solar charging controller
SER	Serenity
SOC	State of charge
STC	Standard test conditions
STRUC	Structures
TC	Temperature coefficient
TM	Transversal magnetic
TX	Transmitting
UHF	Ultra high frequency
UTC	Coordinated universal time
VHF	Very high frequency
VSWR	Voltage standing wave ratio
WLAN	Wireless local area network

Symbols

a	duty cycle in (%)
A	area in (m^2)
ALB	albedo in (1)
c_0	speed of light in (ms^{-1})
c_P	performance coefficient in (1)
C_D	discharge rate in (h^{-1})
d	day in (d); distance in (m)
e	elementary charge in (As)
E	irradiance in (Wm^{-2})
EIRP_{dBW}	effective isotropic radiated power in (dBW)
f_{\sim}	frequency in (Hz)
G	gain in (1) or (dBi)
h	height in (m)
h_s	solar hour angle in ($^{\circ}$)
I	current in (A)
k_B	Bolzmann constant in (WsK^{-1})
k_P	Peukert constant in (1)
L	loss in (1) or (dB)
m	mass in (kg); ideality factor in (1)
mon	month in (1)
N_C	number of photovoltaic cells in (1)
N_d	number of days in (1)
N_{MP}	number of measuring points for the charging and discharging experiment of a battery in (1)
N_{SC}	number of secondary cells of a battery in (1)
NOCT	nominal operating cell temperature in ($^{\circ}\text{C}$)
P	power in (W) or (dBW)

Symbols

Q	charge in (Ah)
ΔQ	charge difference in (Ah)
r	radius in (m)
R	resistance in (Ω)
S	sensitivity of a photovoltaic cell in (AW^{-1})
SOC	state of charge of a battery in (1)
t	time in (h)
Δt	time difference in (h)
T	kinetic energy in (Wh)
TC	temperature coefficient in ($\%^{\circ}\text{C}^{-1}$)
U	voltage in (V)
ΔU	voltage difference in (V)
v	velocity in (ms^{-1})
VSWR	voltage standing wave ratio in (1)
W	energy in (Wh) or (eV)
ΔW_{gap}	band gap of a semiconductor in (eV)
Z_h	equation of time in (h)
Z_{sys}	system impedance in (Ω)
α	temperature coefficient in ($^{\circ}\text{C}^{-1}$)
α_s	azimuth of the Sun in ($^{\circ}$)
β	angle of inclination of a photovoltaic generator with respect to the ground in ($^{\circ}$)
γ_s	altitude of the Sun in ($^{\circ}$)
δ	declination of the Sun in ($^{\circ}$)
ε_0	dielectric constant for free space in ($\text{AsV}^{-1}\text{m}^{-1}$)
ε_r	relative dielectric constant in (1)
λ	longitude in ($^{\circ}$)
λ_0	reference meridian in ($^{\circ}$)
λ_\sim	wavelength in (m)
η	efficiency in (1)
θ	angle of incidence in ($^{\circ}$)
ϑ	temperature in ($^{\circ}\text{C}$)
Θ	phase difference in (rad)
ρ	complex coefficient for vertical polarization in (1)

ϱ	gas density in (kgm^{-3}); specific resistance in ($\Omega\text{mm}^2\text{m}^{-1}$)
σ	conductivity in (Ω^{-1})
τ_B	time constant of $Q_B(t_C \leq t < t_C + t_V)$ in (h)
φ	latitude ($^\circ$)
Φ	radiation flux in (W)
ψ	angle of incidence in ($^\circ$)
ω	angular frequency in (s^{-1})

1 Introduction

When we talk about communication we often mean the transfer or exchange of information between two subjects or groups. What sounds so simple takes on a new meaning when one understands how we managed to overcome immense distances to get closer together.

Since life evolved on Earth, communication has always been present. For example nerve cells use electrical or chemical synapses to communicate, animals communicate through a variety of different methods including pheromones and sounds and humans mainly communicate through the advantageous construct of language [1].

Due to the limitation to communicate over long distances our ancestors invented different techniques to exchange information. One of the oldest known methods of such communication is that of smoke signals which were used to send messages in form of binary information. Much later, with the discovery of electricity, a new era for human communication began when Samuel Finley Breese Morse perfected line telegraphy in the 1830s [2]. Suddenly we were able to instantly exchange complex information over immense distances. From that point on, communication, or more precisely telecommunication, got more and more important and has developed rapidly in recent centuries.

Nowadays telecommunication is an integral part of everyday life. A phone call connects us over several thousand kilometres, scientists can share their research through the vast network of the Internet globally and space probes, like NASA's Voyager 1 and Voyager 2, send us data and images from places, a few centuries ago, we never thought we could ever explore.

For the future we can only dream. But with new knowledge, new technologies emerge.

1.1 About the thesis

This thesis about a voice communication system for a spacesuit simulator was not only proposed to design and build a working backup system for the Serenity spacesuit simulator of the Austrian Space Forum (OeWF), but also to continue humanity's ventures to explore the planet Mars and to add a tiny bit to the long history of telecommunication and space exploration. More about the OeWF and the Serenity spacesuit simulator can be found the appendix A.

1.1.1 Motivation

The voice communication system described in this thesis is closely related to amateur radio systems. This brings an enormous advantage in the form of a solid market

for components and the availability of knowledge from experienced amateur radio operators.

Over the years, amateur radios remained popular due to their reliability and independence from cellular networks and the Internet. Large communities enthusiastically take care of this independent infrastructure around the globe. But not only amateur radio operators use this infrastructure, emergency services such as the red cross, the police and fire departments as well as armed forces use professional radio equipment. It is therefore still considered a crucial infrastructure.

This thinking can be applied to Serenity's backup voice communication system as well. The infrastructure that is used consists of commercially available equipment which can be procured, maintained, repaired and set up easily. Due to its close relation to amateur radio systems it can be used for local emergencies apart from the missions of the OeWF. In addition to these points, the repeater radio infrastructure of Serenity's backup voice communication system is designed to be completely self-sufficient which allows it to be operated in the field without an external power supply. This enables use in remote areas as well as on construction sites, for corporate communication, for disaster relief and for everyday communication by amateur radio operators.

1.1.2 Backup voice communication system

Analog astronauts rely on many critical subsystems, like the voice communication system, to keep them safe and protected while performing simulations. This system is so to speak the lifeline of the analog astronauts which helps them to keep in touch with each other, their safety officers and the base camp crew. For completeness it is noted that the safety officers are trained emergency first responders and the base camp crew monitors and coordinates analog Mars field locally

To guarantee flawless missions, a robust communication system is required. Therefore, the OeWF developed a primary voice communication system which is currently used in the Aouda spacesuit simulator. With several upgrades this system will be used in the Serenity spacesuit simulator as well. It is based on a wireless *local area network* (WLAN) with a range of 15km including a field infrastructure [3]. Should this link fail, a dangerous situation for the analog astronauts can arise. In order to prevent such a situation, it is crucial to add redundancy in the form of a second, completely independent, voice communication system that serves as a backup.

To keep up with the primary WLAN based voice communication system, the OeWF decided to redesign and improve the backup voice communication system for the second generation of its spacesuit simulators. Serenity's backup voice communication system has to be more powerful and reliant than Aouda's. To achieve this goal, the OeWF came up with the requirements listed in the table 1.1.

Requirements	
Range (diameter of square)	15km
Dimensions	Must fit inside the HUT.
Operating temperature within the HUT	5°C to 45°C
Combined mass within the HUT	1000g

Table 1.1: Requirements for the voice communication systems of the Serenity spacesuit simulator.

The backup voice communication system must cover at least a mission area that is created by a square with a diagonal of 15km. With regard to the Serenity spacesuit simulator, its designed backup radio system must fit into its *hard upper torso* (HUT). Within the HUT it must function for the specified operating temperatures and the combined mass of the primary and backup radio systems must not exceed 1000g.

1.2 Aim

The aim of this thesis is to design the backup voice communication system, which from now on will simply be referred to as voice communication system, for the Serenity spacesuit simulator and to carry out a performance estimation based on the design. This must be accomplished while taking into account the requirements mentioned in the table 1.1. Since a repeater radio infrastructure for the voice communication system is necessary to meet the range requirement, a suitable self-sufficient energy distribution system is also designed alongside the voice communication system. A performance estimation is carried out for this system as well. In addition, it will be investigated how the designed voice communication system must be adapted so that it can be used on the Martian surface.

1.2.1 Literature review

Planning voice communication systems is explained in detail in various literatures. Depending on the application, different frequencies and directional characteristics of the antennas involved are used [2], [4]–[7]. For voice communication, however, frequencies in the *very high frequency* (VHF) and *ultra high frequency* (UHF) bands are mostly used in combination with omnidirectional antennas, as the participants of the voice communication system usually move freely within a local covered area [5]. Depending on the required planning accuracy, either a performance estimation is carried out with the plane earth signal budget, or with more complex calculations that take the ground roughness, objects in the beam path between the transmitter and the receiver and atmospheric effect into account [2], [5], [7], [8].

There are also numerous books for planning energy distribution systems. The books [9], [10], for example, provide an overview of how various forms of energy can be converted into electrical energy. Then works like [11]–[13] can be used to read into the energy conversion method that is ultimately used to supply a load with electrical energy. Apart from that, the works [14], [15] describe how the electrical energy can be stored if this is necessary.

Regarding the planning of a voice communication and an energy distribution system on Mars, publications such as [16]–[19] can be used.

1.2.2 Deliverables

This subsection now summarizes the deliverables of the thesis.

1. Design the backup voice communication system for the Serenity spacesuit simulator.
2. Design a self-sufficient energy distribution system for the repeater radio infrastructure of the backup voice communication system.

3. Provide a performance estimation of the voice communication system.
4. Provide a performance estimation of the self-sufficient energy distribution system.
5. Investigate the usability of the designed voice communication and energy distribution system on Mars.

The flowcharts in the figures 1.1 and 1.2, illustrate which steps were taken to achieve these.

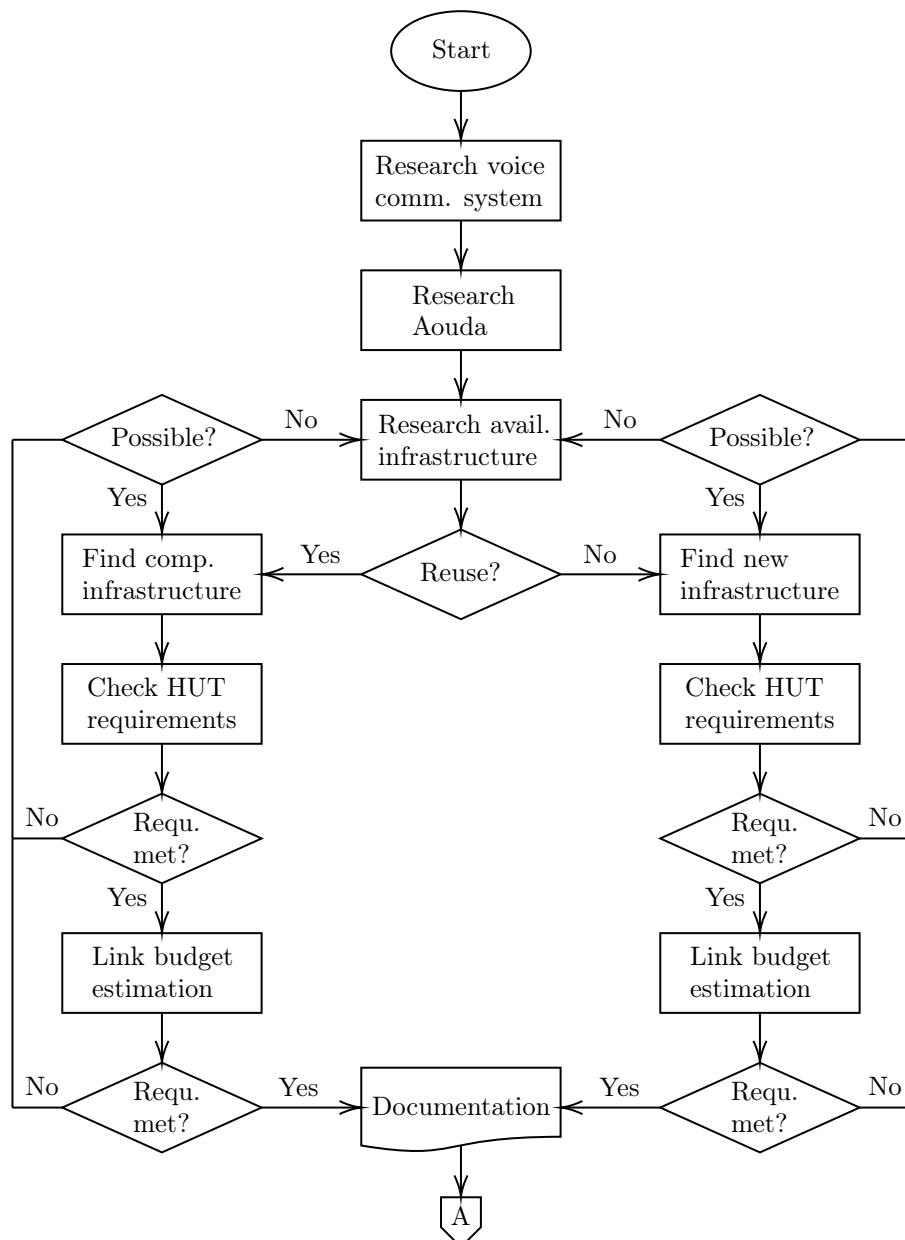


Figure 1.1: Part one of the flowchart of this thesis. It illustrates which steps were taken in order to achieve the deliverables.

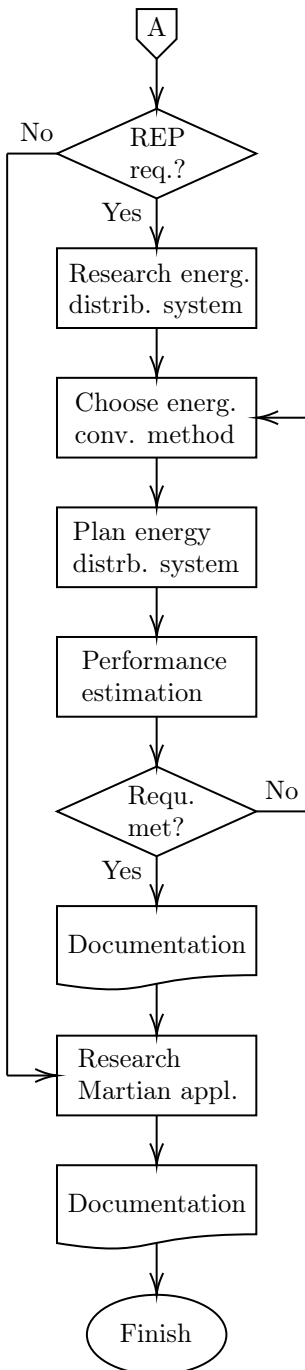


Figure 1.2: Part two of the flowchart of this thesis. It illustrates which steps were taken in order to achieve the deliverables.

1.2.3 Thesis Structure

The first part of this thesis contains the **Methodology** in which the mathematical fundamentals for the system design and the performance estimations of the self-sufficient energy distribution and the voice communication system are explained. This is followed by the **Results**, presenting the system design and the results of the performance estimations. Finally, the **Conclusion and critical reflection** summarizes and interprets the results and provides a critical reflection of this thesis. The appendices contain information about the OeWF and the Serenity spacesuit

simulator, mathematical basics and the developed **MATLAB** simulation for the performance estimation of the self-sufficient energy distribution system.

2 Methodology

In the following sections, the basics of electrical energy distribution and telecommunications necessary for this project are discussed. Since the self-sufficient voice communication system is being developed for use in Mars analog regions on Earth, the focus is on developing a model so that the use of the system in said regions can be simulated. The simulation results are then used to verify the designed system and therefore the requirements. At the end of each section it will be discussed how the developed model of the surface bound communication system on Earth has to be adapted, so that it can be used on the Martian surface instead.

2.1 Electrical energy distribution

A self-sufficient voice communication system consist of at least one or more electrical consumers that must be supplied with electrical energy. This requires a close examination of the system's electrical energy distribution, which includes an energy source, the energy conversion with a suitable electrical generator, internal electrical energy losses and – if necessary – an electrical energy storage device.

The decision to design a self-sufficient voice communication system was made due to a number of reasons. First, it makes the system independent of its location. This of course only applies if the system is operated in a location where there is a source of energy that can be converted by its electrical generator. As a result, it can operate without any external electrical energy source, which offers independence from a local power grid or other on-site electrical generators, such as fuel combustion generators.¹

This already leads to the second and third reason regarding the environmentally harmful way in which electrical energy is generated by burning fossil fuels and the impracticality of fuel combustion generators. With consideration for the planet Earth and its sensitive ecosystem, as well as for future generations, the technologies available today must be used in such a way that the environmental impact of the use of the voice communication system is minimal. Furthermore, looking ahead to future Mars missions, the third reason arises from the fact that its just not a feasable option to bring fuel combustion generators – and the infrastructure required – to the Martian surface [11], [20].

Based on these reasons it was decided to supply the self-sufficient voice communication system from renewable energy sources, such as wind energy, hydroelectric energy, solar energy, bioenergy from biomass, tidal energy etc. Hydroelectric and

¹During some of their previous missions the OeWF used diesel generators at the base camp to supply electrical consumers.

tidal energy were quickly disregarded because there are no bodies of water on the Martian surface. And since the OeWF conducts Mars analog missions on Earth it is not likely that simulation will take place in locations where there are bodies of water that could provide these sources of energy. Bioenergy from biomass can be disregarded due to similar reasons.

2.2 Wind energy

A brief investigation of wind energy showed that the *mechanical rotor power* $P_R = dT_W/dt$ in (W) can be determined from the time derivative of the kinetic energy T_W in (Wh) of a flowing gas – which makes up the atmosphere of a planet and is also known as wind – with the *mass* m_{gas} in (kg), the uniform and constant *flow velocity* v_W in (ms^{-1}), the *density* near the ground² ϱ_{gas} in (kgm^{-3}), the *rotor radius* r_R in (m) and the *performance coefficient*³ c_P in (1). The area $A_W = r_R^2 \pi$ in (m^2) must be perpendicular to the flowing gas. Taking into account the *efficiency* of the mechanical transmission and the electrical generator η_{mech} in (1), the generated *electrical power* P_{el} in (W) can be calculated. A summary of this can be seen below [9], [10], [12], [21]:

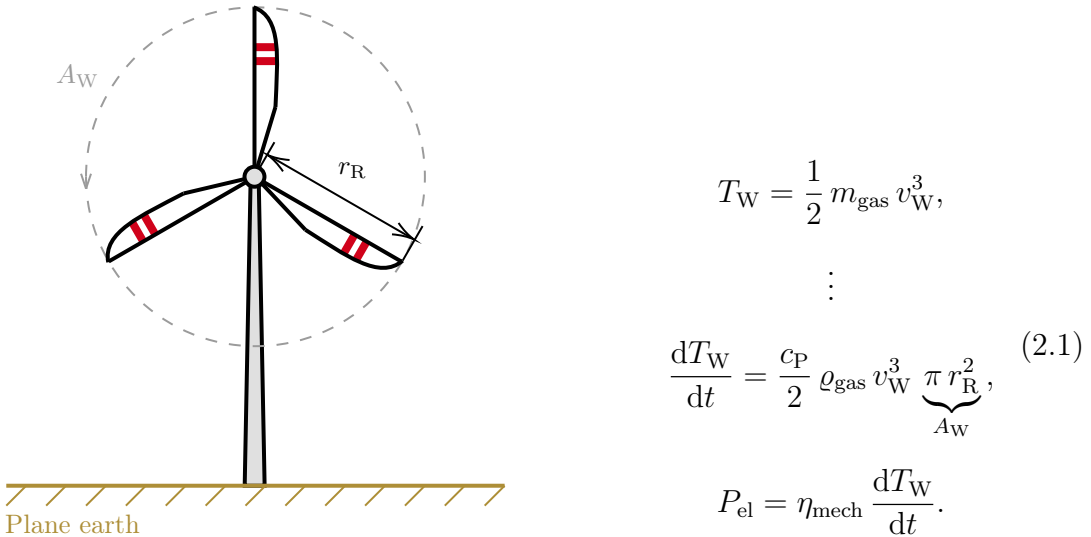


Figure 2.1: Turbine that converts kinetic energy from wind into electrical energy. The dashed circle represents the area A_W that is perpendicular to a flowing gas.

This method of converting electrical energy however, was rejected mainly due to the unpredictability of v_W .⁴ In order to bridge times when no wind blows, a large energy storage device would have to be required, which would be charged in times of strong wind. But due to the high acquisition costs of a large energy storage

²This only applies if the change in gas density at the height of the rotors of the wind turbine is negligible compared to the ground.

³Modern wind turbines reach a performance coefficient ranging from 0,35 to 0,45. According to Betz's law, the ideal performance coefficient is 0,5926.

⁴The direction from which the wind comes is irrelevant for most small-scale wind turbines, as they are rotatably mounted on a mast.

devices, and the relative short duration of the OeWF's missions, this approach is not practical. Another important aspect that led to the rejection of this method is the fact that mean wind speeds are highly dependent on the location and in most parts of the world, 10m above the ground, these are usually between 5ms^{-1} to less than $2,5\text{ms}^{-1}$ as shown in maps provided by [22]. In addition it must be added, that the gas density of air on the Earth's surface $\varrho_{\text{gas},E} = 1,217\text{kgm}^{-3}$ is a lot higher than the gas density on the Martian surface $\varrho_{\text{gas},M} \approx 0,020\text{kgm}^{-3}$ – which is mainly made up of carbon dioxide (CO_2) – and that the wind speeds on Mars, measured by NASA's Viking Landers VL1 and VL2, range from 2ms^{-1} to 7ms^{-1} during summer, 5ms^{-1} to 10ms^{-1} during fall and 17ms^{-1} to 30ms^{-1} during dust storms. It can therefore be seen that – compared to Earth – the greatest negative influence on P_R is the density of the Martian atmosphere [23], [24].

2.3 Solar energy

The Sun constantly emits a *radiation flux* of around $\Phi_S = 3,845 \cdot 10^{26}\text{W}$ into space. Without any doubt it is the greatest source of renewable energy in our solar system. To determine the *solar irradiance* E_S in (Wm^{-2}) that arrives at the top of Earth's atmosphere, the mean distance between the Sun and Earth $r_{SE} = 149,597870 \cdot 10^6\text{km}$ – which is often referred to as *astronomical unit* (AU) – needs to be taken into account as shown in the equation (2.2) [11], [13], [20], [25].

$$E_S = \frac{\Phi_S}{4\pi r_{SE}^2} = \frac{3,845 \cdot 10^{26}\text{W}}{4\pi \cdot (1,49597870 \cdot 10^{11}\text{m})^2} = 1367,21 \frac{\text{W}}{\text{m}^2} \quad (2.2)$$

Figure 2.2 provides an illustration of the Sun and the Earth with consideration of the angular relationships, in which δ is the *declination* of the Sun in ($^\circ$), φ is the local *latitude* of an observer on Earth in ($^\circ$) and γ_S is the *altitude* of the Sun in ($^\circ$) at said latitude. The incident rays on the hemisphere facing the Sun (separated by the dashed line in figure 2.2) can be assumed to be parallel to each other due to the enormous distance between the Sun and Earth [11], [13], [18], [25].

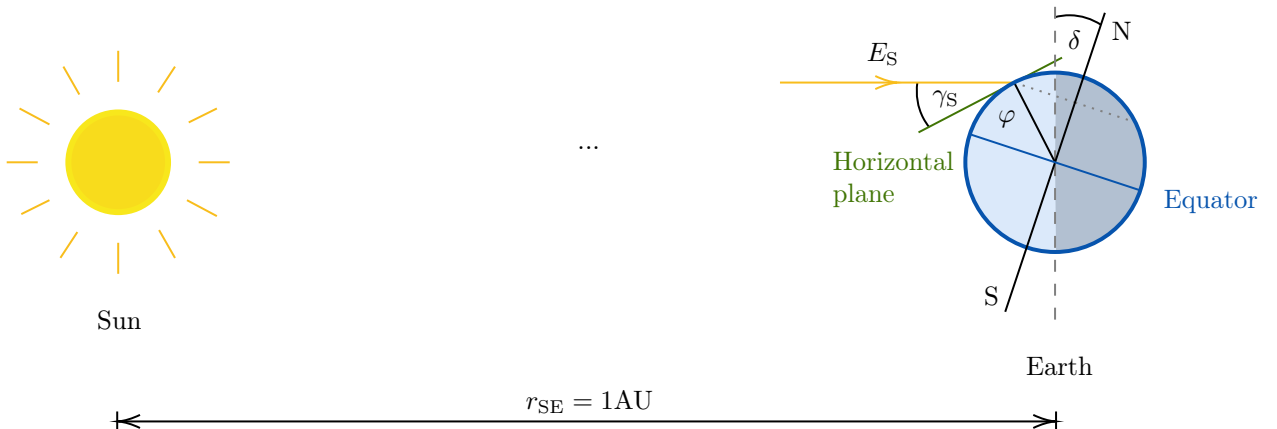


Figure 2.2: Angular relationship between the Sun and Earth. (Recreated from: [11])

A great advantage of solar energy is that its source, the Sun, is highly predictable. This results in the fact, that the electrical energy supply of the self-sufficient voice

communication system can be planned relatively well, as shown in the following subsections. In theory, it can be installed in almost any location where solar rays reach the surface of the Earth. A high modularity of photovoltaic (PV) generators – which are used to convert solar energy into electrical energy – furthermore allows the system to be scaled up by connecting them in series for a higher voltage, or in parallel for a higher current. In both cases the power delivered by the connected PV generators is increased. In addition, PV generators have a very long service life of at least 30 years on Earth. This is due to their structure. Furthermore, compared to wind turbines, they do not have any moving mechanical parts which can be worn down over time. Finally, PV generators have a high power-to-weight ratio, which is preferred for mobile systems [9], [11], [18].⁵

Basic stand-alone systems, as shown in figure 2.3, mainly require a PV generator, a *solar charging controller* (SCC) and an electrochemical energy storage device. In this case the electrochemical energy storage device is a rechargeable battery with a *number of secondary cells* N_{SC} in (1). The SCC is responsible for the charging process of the battery and the electrical supply of the load R_L in (Ω). As illustrated

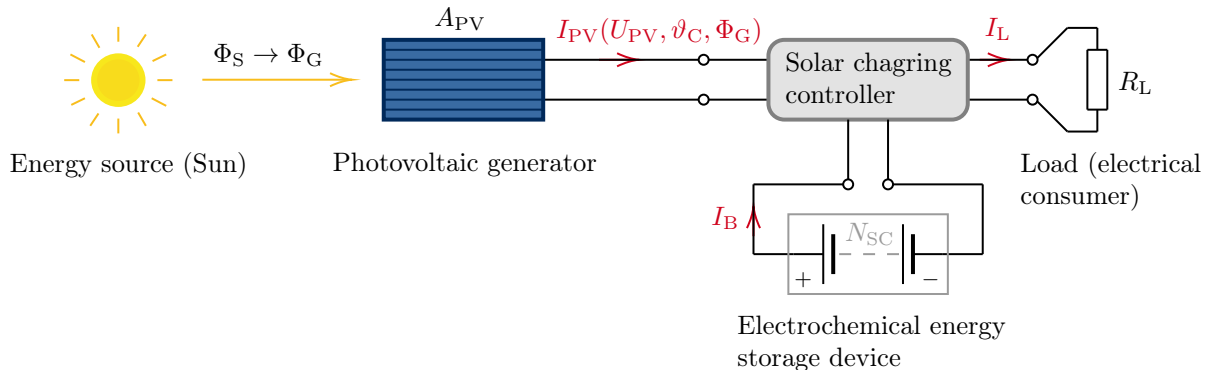


Figure 2.3: Basic structure of an electrical stand-alone system which is supplied with electrical energy by a photovoltaic generator. The energy is stored in an electrochemical energy storage device.

in figure 2.3, the radiation flux Φ_G in (W) onto the PV generator's energy-converting area A_{PV} in (m^2) can be converted into electrical energy. This results in the PV generator current $I_{PV}(U_{PV}, \vartheta_C, \Phi_G)$ in (A). In addition to the radiation flux Φ_G , this current depends on the PV generator voltage⁶ U_{PV} in (V) and the temperature of the PV cells – of which the PV generator consists – ϑ_C in ($^\circ C$), as this temperature plays an important role in the power output of a PV generator. For both, the PV generator and the load, the upper electrical connection (circle) represents the positive electric potential, from which the reference directions for the electrical currents directly follow. I_B in (A) is the *battery current* and I_L in (A) is the *load current*. [11], [20], [26].

With regard to future Mars missions the authors of the articles [16]–[18] found out, that even during prolonged Martian dust storms – when the Martian atmosphere

⁵The self-sufficient voice communication system is referred to as mobile because the OeWF will conduct missions in different Mars analog regions on Earth, which requires it to be installed in different locations and therefore be shipped frequently.

⁶ $I_{PV}(U_{PV})$ defines the current-voltage characteristic of a PV generator.

becomes almost opaque – a PV generator could still convert electrical energy, due to the diffuse component of sunlight. This is supported by empirical data measured with PV generators on Earth as shown in the book [11] and by solar resource maps for Earth’s surface provided by [27]–[29]. The authors of the article [18, p. 1] furthermore state: “*Solar energy is likely to be an important power source for surface-bound operations on Mars.*”, which is another reason why solar energy was selected as a renewable energy source to supply the self-sufficient voice communication system.

In the following subsections the modeling of the self-sufficient energy distribution system of the voice communication system on Earth will be explained. The last subsection adapts these findings to a Martian application.

2.3.1 Angular relationships

Before the energy yield of a PV generator can be calculated, it is essential to introduce a few important angles – of which some were already mentioned – and define how they are counted in this thesis.

The local latitude φ at the equator is 0° and it is counted positive towards the north and negative towards the south with a range of $[-90^\circ, 90^\circ]$, and the local *longitude* λ in $(^\circ)$ is 0° at the reference meridian λ_0 in $(^\circ)$ which passes through the Greenwich Observatory in the United Kingdom. λ is counted positive east and negative west of Greenwich with a range of $(-180^\circ, 180^\circ)$ [13], [18], [25]. For completeness it should be mentioned that the latitude φ and the longitude λ – for a given location on Earth – can be obtained from an atlas or a *global positioning system* (GPS) device.

The Sun’s declination δ indicates how far the Earth’s axis of rotations – which runs through the North and South Poles – leans towards the Sun at solar noon. Its range is $[-90^\circ, 90^\circ]$, although its maximum values for Earth are $-23,45^\circ$ and $23,45^\circ$. δ is counted negative if the North Pole leans away from the Sun and positive if it leans towards the Sun (compare to figure 2.2) [11], [13], [18], [25]. As per [13], the following approximation for δ at a given day of the year, with N_d being the *number of days* since January 1st in (d), *mon* being the *month* in (1) and *d* being the *day* in (d), is sufficient for photovoltaic applications:

$$\delta \approx 23,45^\circ \cdot \sin \left(360^\circ \cdot \frac{284d + N_d}{365d} \right), \quad (2.3)$$

$$N_d \approx 30,3d \cdot (mon - 1) + d. \quad (2.4)$$

The altitude γ_S and the *azimuth* α_S of the Sun in $(^\circ)$, presented in the equations (2.5) and (2.6), describe its position in the sky over the course of the day, with γ_S taking on values within $[0^\circ, 90^\circ]$ and α_S taking on values within $(-180^\circ, 180^\circ]$. How these angles are measured – with the corresponding celestial hemisphere of an observer – is shown in the figure 2.4. For $\gamma_S = 0^\circ$ the Sun is visible at the horizon and for $\gamma_S = 90^\circ$ it is visible at its zenith. For $\alpha_S = 0^\circ$ the Sun is visible exactly in the south. α_S takes on positive values towards the west and negative values towards the east [11], [13], [18], [25].

$$\sin \gamma_S = \sin \varphi \sin \delta + \cos \varphi \cos \delta \cos h_S \quad (2.5)$$

$$\cos \alpha_S = \frac{\sin \varphi \cos \delta \cos h_S - \cos \varphi \sin \delta}{\cos \gamma_S} \quad (2.6)$$

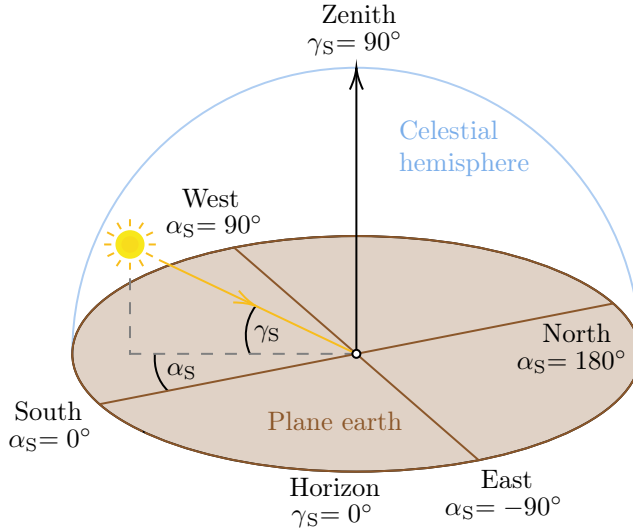


Figure 2.4: Angular relationship of the Sun's altitude γ_S and azimuth α_S with the corresponding celestial hemisphere of an observer. In this figure the Sun already passed the solar noon. (Recreated from: [11])

It must be noted that γ_S and α_S change over the course of the day. By analyzing the equations (2.5) and (2.6), while taking into account that φ does not change because the self-sufficient voice communication system is stationary for the entire mission and that in this thesis δ is modeled with a constant value throughout the day – although it takes on different values for each day of the year – it must be the variable h_S in ($^{\circ}$) that is responsible for these changes. It is called the *solar hour angle* and its value is 0° when the Sun reaches its greatest daily altitude γ_S , which occurs at solar noon. This happens for either $\alpha_S = 0^{\circ}$, $\alpha_S = 180^{\circ}$ or for $\gamma_S = 90^{\circ}$, where α_S is undefined. h_S is counted negative before the solar noon and positive after the solar noon with a range of $(-180^{\circ}, 180^{\circ})$. [11], [13], [18], [25].

For a given *solar time*⁷ t_S in (h), the hour angle h_S can be determined as shown in equation (2.7). The factor $\frac{15^{\circ}}{1\text{h}}$ comes about because the Earth rotates 360° within 24h. Thus the range of the solar time t_S can be derived to $[0\text{h}, 24\text{h})$. Further, the hour angle for the *solar sunrise time* $t_{S,r}$ in (h) and the *solar sunset time* $t_{S,s}$ in (h) can be calculated with the equations (2.8) and (2.9) [11], [13], [18], [25].

$$h_S = (t_S - 12\text{h}) \cdot \frac{15^{\circ}}{1\text{h}} \quad (2.7)$$

$$h_{S,r} = -\arccos(-\tan \delta \tan \varphi), \quad \text{for } |\varphi| < 90^{\circ} - |\delta| \quad (2.8)$$

$$h_{S,s} = \arccos(-\tan \delta \tan \varphi), \quad \text{for } |\varphi| < 90^{\circ} - |\delta| \quad (2.9)$$

In the article [18] a few important cases, regarding the equations (2.8) and (2.9), are mentioned which might be of interest when selecting a location to install the

⁷In most cases the solar time t_S differs from the local time on a wrist watch. For $t_S = 12\text{h}$ (solar noon) the Sun is either exactly in the south, in the north or at its zenith, whereas the Sun might not be exactly in the south, in the north or at its zenith for the *local time* $t_{\text{local}} = 12\text{h}$ on a wrist watch – no matter how accurate it is set to the local time.

self-sufficient voice communication system:

$$\tan \delta \tan \varphi \begin{cases} > 1 & \text{polar night, if } \varphi < -90^\circ + \delta \text{ or } \varphi > 90^\circ + \delta, \\ = \pm 1 & \text{the Sun is only visible at the horizon for an instant,} \\ < -1 & \text{polar day, if } \varphi < -90^\circ - \delta \text{ or } \varphi > 90^\circ - \delta. \end{cases}$$

The solar time t_S can finally be calculated from t_{UTC} in (h), which is the *Co-ordinated Universal Time* (UTC), using the equation (2.10) where $\lambda_0 = 0^\circ$ is the reference meridian for which t_{UTC} applies and Z_h in (h) is the *equation of time* which serves as a correction factor [13], [25].

$$t_S = t_{\text{UTC}} + Z_h + (\lambda - \lambda_0) \cdot \frac{1h}{15} \quad (2.10)$$

$$Z_h \approx 0,123h \cdot \cos \left(360^\circ \cdot \frac{88d + N_d}{365d} \right) - 0,167h \cdot \sin \left(720^\circ \cdot \frac{10d + N_d}{365d} \right) \quad (2.11)$$

2.3.2 Solar irradiation on the Earth's surface

Compared to equation (2.2), determining the Sun's irradiance arriving on the surface of Earth is rather complex.⁸ Precise calculations depend on many different factors such as the changing angular relationship between the Sun and Earth throughout the year, the composition of Earth's atmosphere – which changes the Sun's spectrum due to absorption and scattering effects – and many more [11], [13], [18].

With solar resource maps however, this problem can be circumvented. They are based on satellite and atmospheric solar irradiance models and meteorological data that were designed and collected over several years. By using these maps the compromise is made that the following calculations and estimates are performed with average irradiance values instead of exact ones. Figures 2.5 and 2.6 provided by [27], [28] show the solar resource maps of the long term average global horizontal and direct normal irradiation, from 1994 until 2018, of Austria. The scale below the maps shows daily and annual total irradiation in (kWhm^{-2}) [31]–[33].

It can be clearly seen that the values for both the global horizontal and the direct normal irradiation tend to be higher in the south and lower in the north of Austria. This can be partly explained by a greater latitude φ which results in a lower altitude of the Sun γ_S during the winter months on the northern hemisphere ($\delta < 0$). Because of this, the Sun's incoming rays need to penetrate a thicker atmosphere and it is visible above the horizon for a shorter period of time over the course of the day. For locations in the south, such as the region around Klagenfurt, daily global horizontal irradiation totals of up to $3,50\text{kWhm}^{-2}$ and direct normal irradiation totals of up to $3,55\text{kWhm}^{-2}$ and higher can be expected, whereas locations in the north, such as the region around Linz, only reach daily global horizontal irradiation totals of around $3,25\text{kWhm}^{-2}$ and daily direct normal irradiation totals of around $2,9\text{kWhm}^{-2}$. Another notable feature are valleys bordered by mountains in the south. In these valleys, and on the bounding north-facing mountain slopes, the daily

⁸The authors of the article [30] use the Capderou method to model the incident solar radiation on Earth. In the articles [16], [17] this topic is investigated with a different method for the planet Mars.

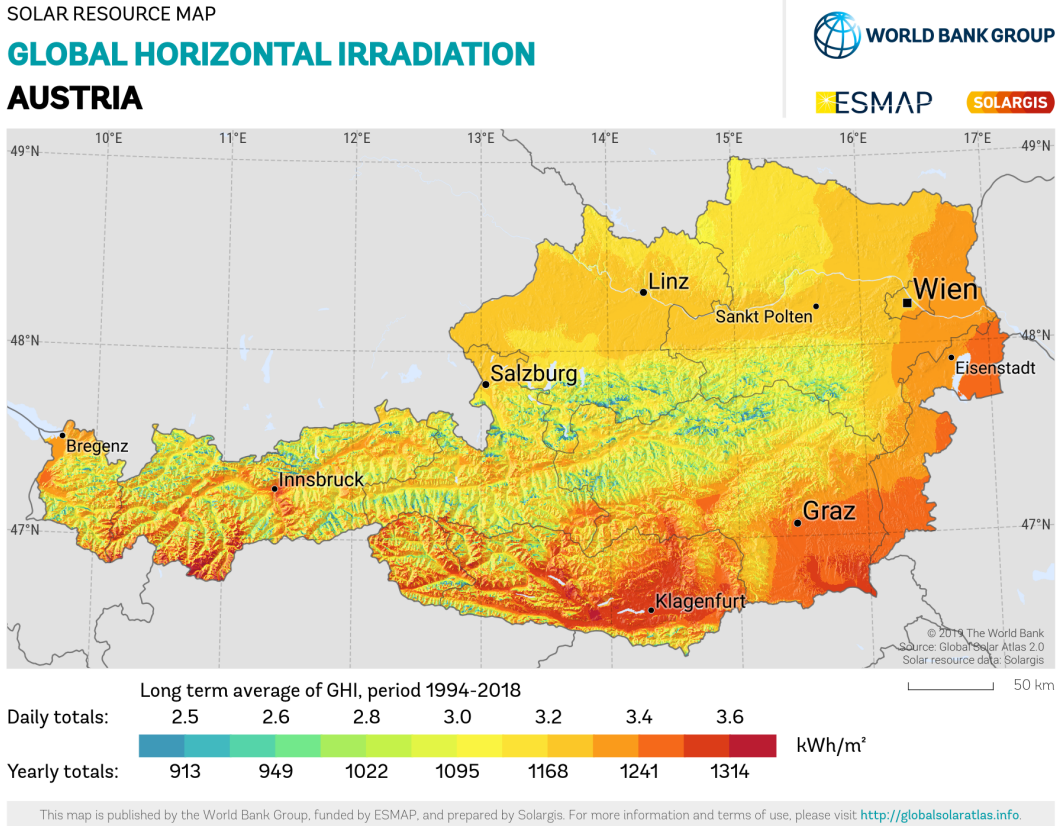


Figure 2.5: Solar resource map of the long term average global horizontal irradiation of Austria. (Image credit: [28], [34])

global horizontal irradiation totals drop to less than $2,5\text{ kWh m}^{-2}$ and the daily direct normal irradiation totals drop even further down to around $1,5\text{ kWh m}^{-2}$. Examples for such valleys can be located all across the Alps and they highlight that locations with geographical features that block the direct path of the sunlight, should be discarded as installation sites for a PV generator [11], [13], [25].

Using such maps, the *global horizontal irradiance* (E_{GHI}) in (W m^{-2}) and the *direct normal irradiance* (E_{DNI}) in (W m^{-2}) – at a given location on Earth – can be determined by dividing the values of the global horizontal and the direct normal irradiation by the time over which they were averaged. For instance by 24h or by $365\text{d} \cdot 24\text{h}$ – depending on which scale is used from the figures 2.5 and 2.6 [11], [33].

The GHI is the sum of *direct horizontal irradiance* (E_{DHI}) in (W m^{-2}) and the *diffuse horizontal irradiance* (E_{DIFH}) in (W m^{-2}) – which is caused by the scattering of sunlight by Earth’s atmosphere – as shown in equation (2.12) [11], [32].

$$E_{\text{GHI}} = E_{\text{DHI}} + E_{\text{DIFH}} \quad (2.12)$$

In comparison to the GHI – which applies to a horizontal surface – the DNI applies to a flat surface element perpendicular to the incoming Sun rays and it only considers the direct irradiance [11], [32]. With simple trigonometry as shown in [11], the relationship between E_{DNI} and E_{DHI} can be written as:

$$E_{\text{DNI}} = E_{\text{DHI}} \frac{1}{\sin \gamma_s}. \quad (2.13)$$

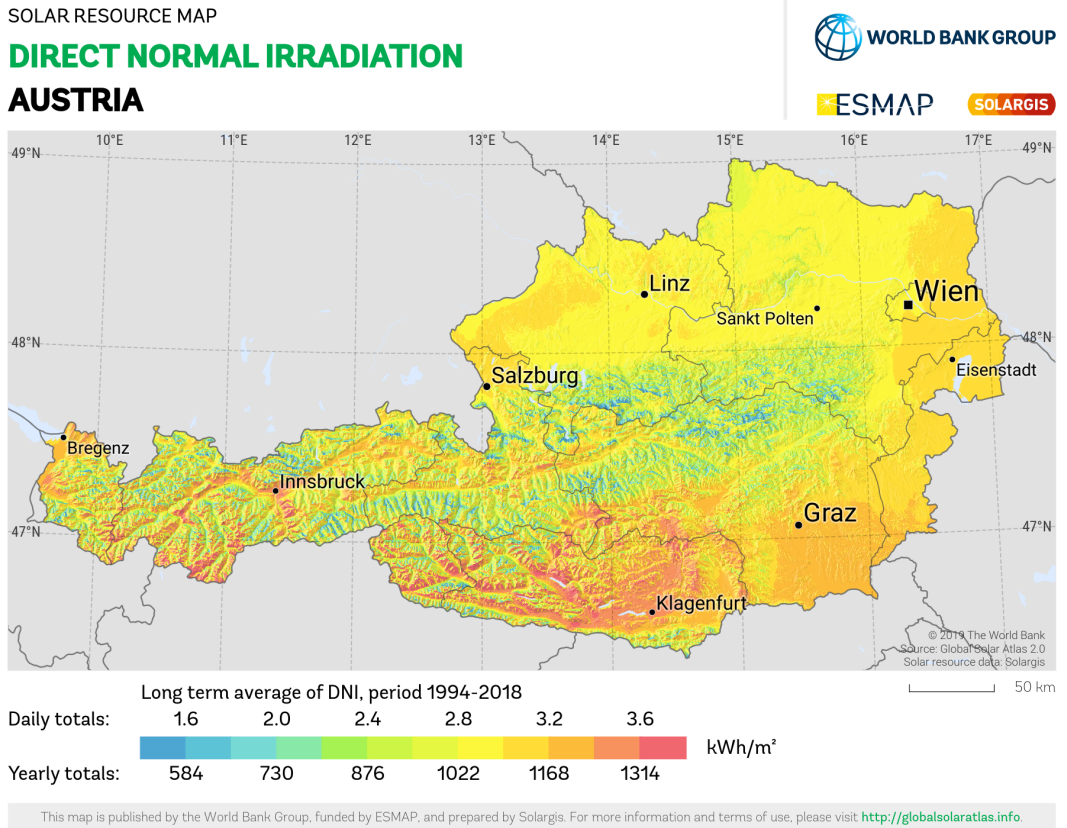


Figure 2.6: Solar resource map of the long term average direct normal irradiation of Austria. (Image credit: [28], [34])

More precise solar resource maps for daily and monthly average global horizontal and direct normal irradiation are provided by [29].

2.3.3 Photovoltaic energy yield

As already mentioned in subsection 2.3.2 the decisive factors to determine the irradiance at a given location on the Earth's surface are the GHI and the DNI. Building on these, the three-component model as described in [11], [18], can be used to calculate the *total irradiance* E_G in (Wm^{-2}) received by an inclined PV generator. The angle of inclination with respect to the ground is β in ($^\circ$). An example for such an inclined PV generator can be seen in the figures 2.7 and 2.8. Figure 2.7 illustrates that the total irradiance received by an inclined PV generator is made up of the sum of the *direct generator irradiance* (DGI) E_{DGI} in (Wm^{-2}), the *diffuse generator irradiance* (DIFG) E_{DIFG} in (Wm^{-2}) and the *reflected generator irradiance* (RGI) E_{RGI} in (Wm^{-2}). The latter is reflected with an *albedo* value ALB in (1) from plane earth onto the PV generator. This relationship can be written as follows [11], [20], [35], [36]:

$$E_G = E_{\text{DGI}} + E_{\text{DIFG}} + E_{\text{RGI}} \quad (2.14)$$

The first component from equation (2.14) can be determined by considering the angle of incidence θ of the solar rays in ($^\circ$) with respect to the normal of the PV generator's energy-converting area A_{PV} , as presented in equation (2.15). Figure 2.8 provides an illustration of the angle θ for which the cosine can be obtained from

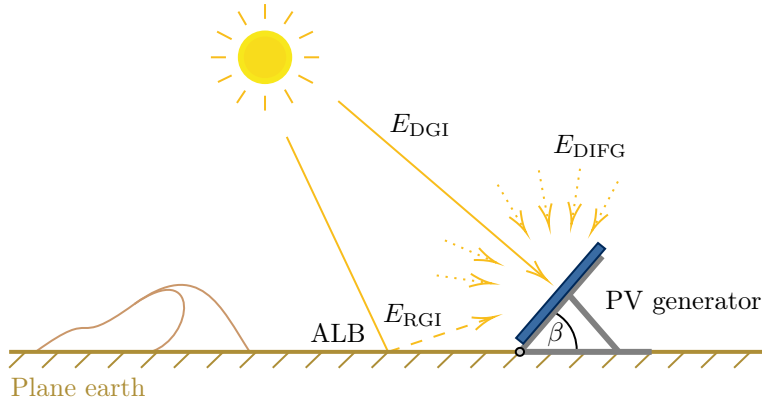


Figure 2.7: Solar radiation on an inclined photovoltaic generator with the angle β . (Recreated from: [11])

equation (2.16).

$$E_{\text{DGI}} = E_{\text{DNI}} \cos \theta \quad (2.15)$$

$$\begin{aligned} \cos \theta = & \sin \delta \sin \varphi \cos \beta - \sin \delta \cos \varphi \sin \beta \cos \alpha_S(t_S = 12\text{h}) \\ & + \cos \delta \cos \varphi \cos \beta \cos h_S + \cos \delta \sin \varphi \sin \beta \cos \alpha_S \cos h_S \quad (2.16) \\ & + \cos \delta \sin \beta \cos h_S \sin \alpha_S(t_S = 12\text{h}) \end{aligned}$$

The angle of incidence θ has a range of $[0^\circ, 90^\circ]$ and $\alpha_S(t_S = 12\text{h})$ represents

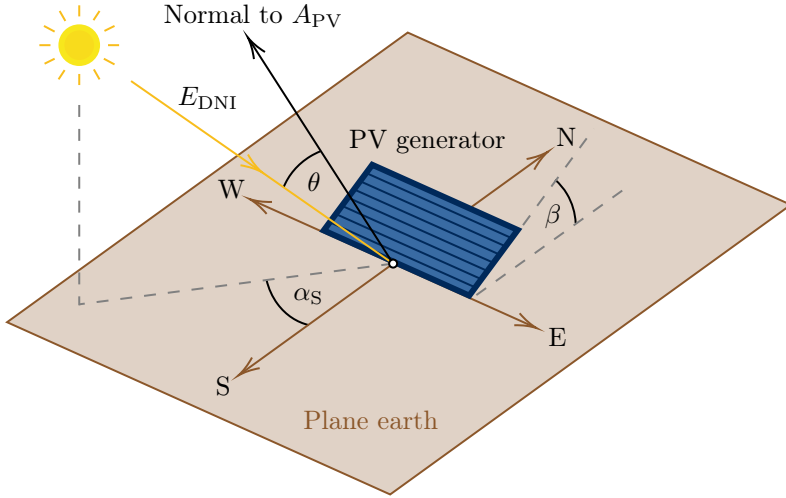


Figure 2.8: Illustration of the incidence angle θ of the solar rays with respect to the normal to A_{PV} . (Recreated from: [18])

the orientation of the normal to A_{PV} . For completeness it must be mentioned that equation (2.5) can be derived from equation (2.16) with $\beta = 0^\circ$, and that in the case $\gamma_S + \beta = 90^\circ$, the Sun's rays are perpendicular to the PV generator's energy-converting area A_{PV} which results in $E_{\text{DGI}} = E_{\text{DNI}}$ [11], [13], [18], [20].

To determine the second component from equation (2.14) the sky is assumed to be isotropic. This means that the DIFH is evenly distributed in the entire celestial hemisphere above the PV generator. The more the PV generator is inclined the smaller the proportion of DIFG in equation (2.17) becomes (compare to figure 2.7)

[11], [18].

$$E_{\text{DIFG}} = E_{\text{DIFH}} \frac{1 + \cos \beta}{2} \quad (2.17)$$

In the book [11] it is expressly pointed out that the isotropic approach used in equation (2.17) is only a rough approximation. This is because the sky is brighter towards the Sun than towards the horizon.⁹

When examining the last component from equation (2.14) it has to be taken into account that different surfaces – on which a PV generator is placed – reflect solar rays differently. In equation (2.18) this is accomplished with the factor ALB – also known as the reflectivity. Similar to equation (2.17) an isotropic approach is used [11], [18], [36], [37].

$$E_{\text{RGI}} = E_{\text{GHI}} \frac{1 - \cos \beta}{2} \cdot \text{ALB} \quad (2.18)$$

Approximate albedo values for various surfaces are listed in table 2.1. The larger the value the more solar rays are reflected. A blackbody for example has an albedo value of 0 while an absolute white surface has an albedo value of 1. The Earth has an average albedo of 0,31 [35]–[37].

Surface	Albedo	Surface	Albedo
Forest	0,05 – 0,18	Sand	0,20 – 0,40
Water	0,06 – 0,10	Grass (July, August)	0,25
Rain forest	0,07 – 0,15	Dry sandy soil	0,25 – 0,45
Coniferous forest	0,09 – 0,15	Uncultivated field	0,26
Dark-colored soil surfaces	0,10 – 0,20	New concrete	0,30
Heathland	0,10 – 0,25	Granite	0,30 – 0,35
Asphalt	0,15	Glacial ice	0,30 – 0,40
Deciduous forest	0,15 – 0,18	Light-colored soil surfaces	0,40 – 0,50
Dry clay soil	0,15 – 0,35	Old snow	0,45 – 0,70
Lawn	0,18 – 0,23	Dry salt cover	0,50
Weathered concrete	0,20	Fresh snow	0,80 – 0,90

Table 2.1: Albedo values (reflectivity) for different surfaces [11], [20], [36], [37].

If the three derived components E_{DGI} , E_{DIFG} and E_{RGI} are now inserted into equation (2.14) while considering the equations (2.12) and (2.13), the total irradiance E_G received by an inclined PV generator, depending on E_{GHI} , E_{DNI} , γ_S , β and ALB, can be obtained:

$$E_G = E_{\text{DNI}} \cos \theta + (E_{\text{GHI}} - E_{\text{DNI}} \sin \gamma_S) \frac{1 + \cos \beta}{2} + E_{\text{GHI}} \frac{1 - \cos \beta}{2} \cdot \text{ALB.} \quad (2.19)$$

Regarding this equation it must be noted that the angles γ_S and θ are time dependent and therefore E_G as well. E_{GHI} and E_{DNI} on the other hand are average values – if taken from solar resource maps – and can therefore be treated as constants. The angle of inclination β as well as the albedo value ALB are also treated as constants. Once the PV generator is installed its inclination angle β will not change for the

⁹More precise equations would be difficult to derive, which would go beyond the scope of this thesis.

entire duration of the mission. This has the consequence that the PV generator's inclined energy-converting area A_{PV} is only perpendicular for one pair of γ_S and α_S at a given time of the day. Even though ALB is treated as a constant, there are situations in which the albedo value of a surface can change over the course of a few hours. For instance, if the PV generator is installed on a freshly snowed uncultivated field and the snow melts away. In this case ALB would change from 0,80 to 0,26. Such situations must be considered while simulating the PV generator's daily energy yield. This can be accomplished by considering the lowest possible albedo value for a given region [11], [17], [18].

As described by [11], [13], the radiation flux Φ_G onto the PV generator's energy-converting area A_{PV} – to be more precise the sum of the energy-converting area of the PV cells – can be calculated as follows:

$$\Phi_G = A_{PV} E_G. \quad (2.20)$$

How to determine the optimal angle of inclination β for a PV generator will be discussed in the next subsection.

2.3.4 Photovoltaic generator alignment

Simply put, the alignment of a stationary PV generator – which does not actively track the Sun throughout the day, but is installed with a fixed orientation of the normal to A_{PV} , with respect to the cardinal directions, and a constant inclination angle β – depends on two basic factors.

The first factor regards the Sun's direct irradiance, which reaches its greatest daily value for clear skies at solar noon ($t_S = 12h$). This is the point in time, in which γ_S reaches its greatest daily value, and thus the Sun's rays have the shortest path through Earth's atmosphere to the surface. The path becomes longer, the smaller γ_S becomes – regardless of whether it is before or after solar noon.¹⁰ Using the air mass (AM) value x , this can be expressed as follows:

$$x = \frac{1}{\sin \gamma_S}. \quad (2.21)$$

For example, for $\gamma_S = 90^\circ$ the Sun is at its zenith. This results in $x = 1$ and therefore its rays have the shortest possible path through Earth's atmosphere to the surface. Since the spectrum of the Sun on the Earth's surface changes, depending on the length of the path of the Sun's rays, this spectrum is called AM 1. The AM 0 spectrum would be outside the Earth's atmosphere which corresponds to the previously mentioned solar constant E_S . [11], [13], [18], [20].

Besides this, the second factor regards the fact that the self-sufficient voice communication system will be in use for the entire duration of a mission. Therefore it requires electrical energy throughout the day.

¹⁰Regarding the optimal inclination angle of a PV generator for clear skies, the authors of [18, p. 7] write:

“For clear days, the solar irradiance is symmetrical around noon and is maximum at true solar noon, $\omega = 0$.”

The angle ω represents the solar hour angle h_S .

Based on these findings it can be said that a stationary PV generator must be aligned in a way, so that its energy-converting area A_{PV} is perpendicular to the Sun's rays when it reaches its greatest daily irradiance value. This occurs when the Sun's rays have the shortest path through Earth's atmosphere. As a result, the normal to A_{PV} must be aligned with the incoming rays for this specific point in time, hence for $t_S = 12\text{h}$. In this case, the daily electrical energy yield of a stationary PV generator can be maximized [11], [13], [18].

As mentioned in subsection 2.3.3, the Sun's rays are perpendicular to the energy-converting area A_{PV} for $\beta = 90^\circ - \gamma_S$. After applying this to equation (2.5) and simplifying it with trigonometric functions, the PV generator's angle of inclinations β at a latitude φ , with Earth's axis of rotation inclined towards the Sun with the angle δ , can be derived as shown in equation (2.22) [11], [13], [18].

$$\beta = |\varphi - \delta| \quad (2.22)$$

The **MATLAB** simulation in the appendix C.1 showed that using the absolute value of β , it can be obtained for every installation site on Earth and for every season of the year. This is also shown by the authors of [38].¹¹

Determining how the normal to A_{PV} must be oriented with respect to the cardinal directions can be accomplished by solving the equations (2.5) and (2.6) for $t_S = 12\text{h}$. With the help of trigonometric functions this results in:

$$\gamma_S = 90^\circ - \varphi + \delta, \quad \text{for } t_S = 12\text{h} \quad (2.23)$$

$$\alpha_S = \arccos \left(\frac{\sin(\varphi - \delta)}{\cos \gamma_S} \right), \quad \text{for } t_S = 12\text{h}. \quad (2.24)$$

For $\alpha_S = 0^\circ$ the Sun is visible in the south and therefore a PV generator must be oriented in a way so that the normal to A_{PV} points towards the south, and for $\alpha_S = 180^\circ$ the Sun is visible in the north and therefore the normal to A_{PV} must point towards the north. When the Sun is at its zenith α_S cannot be solved because $\gamma_S = 90^\circ$. In this case $\varphi = \delta$, from which $\beta = 0^\circ$ follows, and therefore the normal to A_{PV} must point to the Sun's zenith.

A more practical approach to this can be achieved by comparing the latitude of a PV generator's installation site to the latitude φ_Z in ($^\circ$), where the Sun is at its zenith for $t_S = 12\text{h}$, using a GPS device. Figure 2.9 compares the three different cases of the Sun's location in the sky, depending on the installation site of a PV generator, in which φ_S in ($^\circ$) is an installation site to the south and φ_N in ($^\circ$) to the north of φ_Z .

Inserting $\gamma_S = 90^\circ$ and $t_S = 12\text{h}$ into equation (2.5), the latitude φ_Z can be determined – after applying trigonometric functions – to:

$$\varphi_Z = \delta. \quad (2.25)$$

If a PV generator is installed at a latitude south of φ_Z , the normal to A_{PV} must point towards the north, and if it is installed north of φ_Z , the normal to A_{PV} must point towards the south. In case the PV generator is installed at the latitude φ_Z , then $\beta = \varphi_Z - \delta = 0^\circ$ applies, which means that the normal to A_{PV} points to the Sun's zenith. The normal to A_{PV} can be aligned using a simple compass.

¹¹Nevertheless, the result of $\tan \delta \tan \varphi$ must be taken into account.

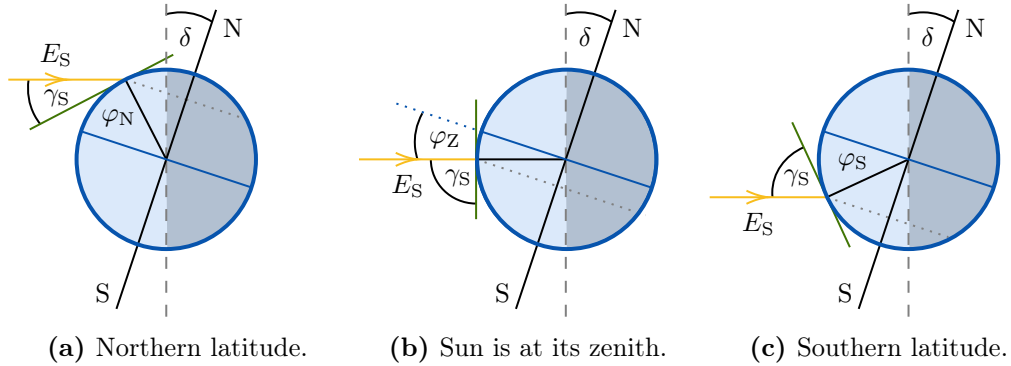


Figure 2.9: Illustration of the latitude φ_Z on Earth at which the Sun is at its zenith for $t_S = 12\text{h}$. By comparing the latitude of the installation site of a photovoltaic generator it can be determined how it must be aligned, so that the electrical energy yield can be maximized.

2.3.5 Modeling the solar energy curve

To further estimate the electrical energy yield of a PV generator which is inclined with the angle β , the Sun's radiation flux Φ_G onto its energy-converting area A_{PV} must be modeled over the course of one day. Since the Sun's irradiance is symmetrical for $t_0 = 12\text{h}$ and the PV generator is assumed to be aligned so that A_{PV} is perpendicular to the Sun's rays for $t_0 = 12\text{h}$, the Sun's radiation flux Φ_G as a Gaussian function of the solar time t_S can be approximated as shown in the figure 2.10. The corresponding Gaussian function can be obtained from equation (2.26):

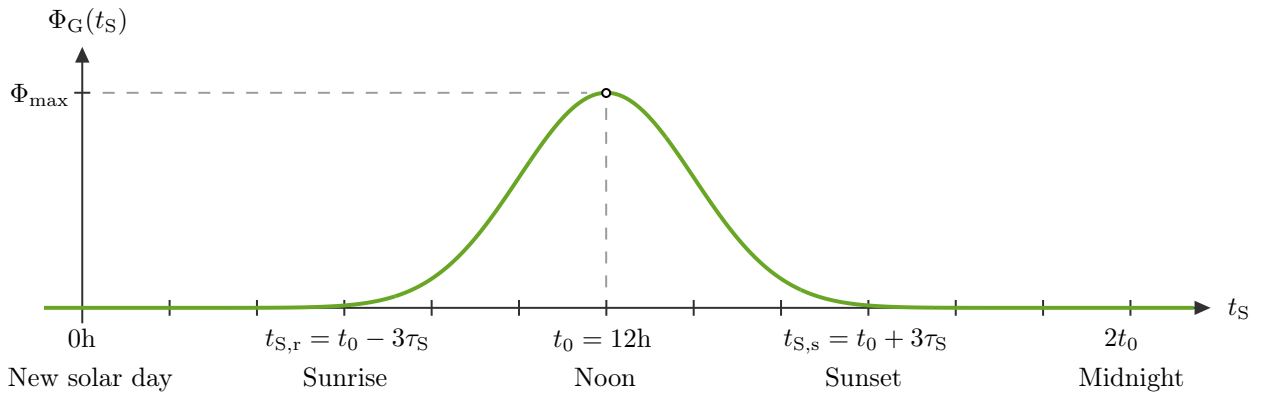


Figure 2.10: Model of the Sun's radiation flux Φ_G onto the energy-converting area of a photovoltaic generator as a Gaussian function of the solar time t_S . It is assumed that the Sun's irradiance is symmetrical around solar noon, and that the photovoltaic generator is aligned so that its energy-converting area is perpendicular to the Sun's rays at solar noon.

$$\Phi_G(t_S) = \Phi_{\max} \exp \left(-\frac{(t_S - t_0)^2}{2\tau_S^2} \right), \quad (2.26)$$

$$\tau_S = \frac{t_0 - t_{S,r}}{3} = \frac{t_{S,s} - t_0}{3}.$$

The area this curve encloses with the solar time axis t_S , from solar sunrise $t_{S,r}$ to solar sunset $t_{S,s}$, is equal to 99,7% of the *daily solar energy* W_G in (Wh) which occurs

on the energy-converting area A_{PV} [2], [18], [39]–[42]:¹²

$$W_G = \frac{1}{0,997} \int_{t_{S,r}}^{t_{S,s}} \Phi_{\max} \exp \left(-\frac{(t_S - t_0)^2}{2\tau_S^2} \right) dt_S = \frac{\Phi_{\max} \tau_S \sqrt{2\pi}}{0,997}. \quad (2.27)$$

A similar approach is used in [43], [44] and in [11], [45], [46] it can be seen that the Sun's total irradiance E_G throughout the day, from which Φ_G derives, behaves similar to a Gaussian curve.¹³

The greatest daily radiation flux Φ_{\max} in (W) onto A_{PV} can be calculated using the equations (2.19) and (2.20) by deriving the following relationship:

$$W_G = \int_{t_{S,r}}^{t_{S,s}} \Phi_G dt_S = A_{\text{PV}} \int_{t_{S,r}}^{t_{S,s}} E_G dt_S. \quad (2.28)$$

Considering that A_{PV} is a constant factor and taking into account the findings from the subsection 2.3.3, the integrals from equation (2.28) can be partly solved as follows:

$$\begin{aligned} \int_{t_{S,r}}^{t_{S,s}} E_G dt_S &= E_{\text{GHI}} \left(\frac{1 + \cos \beta}{2} + \frac{1 - \cos \beta}{2} \cdot \text{ALB} \right) \cdot (t_{S,s} - t_{S,r}) \\ &\quad - E_{\text{DNI}} \underbrace{\frac{1 + \cos \beta}{2} \int_{t_{S,r}}^{t_{S,s}} \sin \gamma_S dt_S}_{\mathbf{I}} + \underbrace{E_{\text{DNI}} \int_{t_{S,r}}^{t_{S,s}} \cos \theta dt_S}_{\mathbf{II}}. \end{aligned} \quad (2.29)$$

Using the equations (2.5) and (2.7), integral **I** can be solved to:

$$\begin{aligned} \mathbf{I}: \int_{t_{S,r}}^{t_{S,s}} \sin \gamma_S dt_S &= \sin \varphi \sin \delta (t_{S,s} - t_{S,r}) \\ &\quad + c_{\varphi,\delta} \left(\sin \left((t_{S,s} - 12h) \cdot \frac{15^\circ}{1h} \right) - \sin \left((t_{S,r} - 12h) \cdot \frac{15^\circ}{1h} \right) \right), \end{aligned} \quad (2.30)$$

with $c_{\varphi,\delta}$ being:

$$c_{\varphi,\delta} = \cos \varphi \cos \delta \cdot \frac{1h}{15^\circ}. \quad (2.31)$$

Integral **II** on the other hand cannot be solved analytically as easy. This is why a sum instead of an integral is used in the **MATLAB** simulation (see appendix C.1) to calculate W_G :

$$W_G = A_{\text{PV}} \sum_{t_S=t_{S,r}}^{t_{S,s}} E_G \Delta t_S. \quad (2.32)$$

¹² $t_{S,r}$ and $t_{S,s}$ were selected this way for simplicity.

¹³How to solve the integral in equation 2.27 from $-\infty$ to ∞ can be found in the appendix B.1.

Using trigonometric functions, E_G can be simplified as shown in the equation (2.33). Depending on the desired accuracy Δt_S in (h) can be smaller or greater. The smaller it is the more accurate W_G can be modeled.¹⁴

$$\begin{aligned} \sum_{t_S=t_{S,r}}^{t_{S,s}} E_G \Delta t_S &= \sum_{t_S=t_{S,r}}^{t_{S,s}} (E_{GHI} - E_{DNI} \sin \gamma_S) \cos^2 \frac{\beta}{2} \Delta t_S \\ &+ \sum_{t_S=t_{S,r}}^{t_{S,s}} \left(E_{DNI} \cos \theta + E_{GHI} \sin^2 \frac{\beta}{2} \cdot ALB \right) \Delta t_S \end{aligned} \quad (2.33)$$

By inserting the calculated W_G from equation (2.32) into equation (2.27) and transforming it, the greatest daily radiation flux Φ_{\max} onto A_{PV} , which in this model occurs for $t_0 = 12h$, can be obtained [17], [18], [39], [40]:

$$\Phi_{\max} = \frac{0,997 \cdot A_{PV}}{\tau_S \sqrt{2\pi}} \sum_{t_S=t_{S,r}}^{t_{S,s}} E_G \Delta t_S. \quad (2.34)$$

2.3.6 Photovoltaic generators

The aim of this subsection is to model the electrical power output P_{PV} in (W) of a PV generator based on the previous findings. Since most commercial PV generators consist of PV cells connected in series, only these are going to be covered. Figure 2.11 shows the *electrical equivalent circuit* (EEC) of such a PV generator with a given number of PV cells N_C in (1). As illustrated, I_{PV} is equal for all PV cells

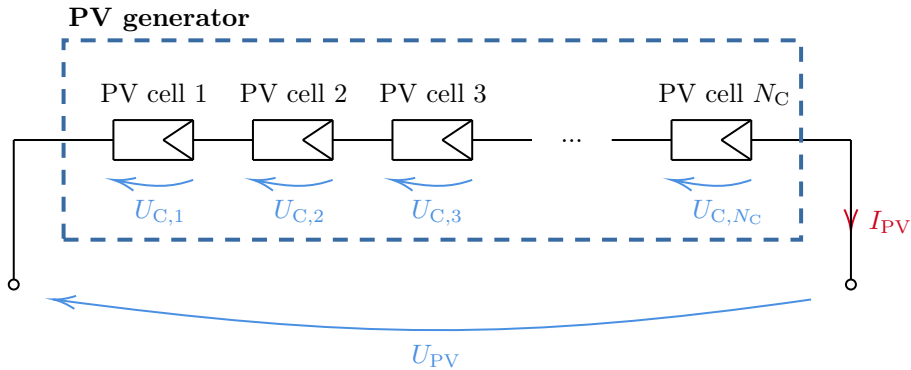


Figure 2.11: Electrical equivalent circuit of a photovoltaic generator. It consists of N_C photovoltaic cells connected in series. (Recreated from: [11])

and U_{PV} is the sum of the *PV cell voltages* U_C in (V). It is assumed that all PV cells have the same voltage U_C and therefore U_{PV} can be written as presented in the equation (2.35). For the sake of simplicity it is furthermore assumed that the PV generator is installed in a way so that no shadowing occurs during the course of the mission [11], [39].

$$U_{PV} = N_C U_C \quad (2.35)$$

¹⁴ Δt_S is one discrete time step of the solar time. It can be calculated from the length len of the Matlab vector that goes from $t_{S,r}$ to $t_{S,s}$: $\Delta t_S = \frac{1}{len}$.

In the next step the PV cells shown in figure 2.11 must be modeled. For this, the simplified standard model¹⁵ is used as there are explicit solutions for U_C and I_{PV} . It represents an ideal PV cell without internal losses. An illustration of this model is provided in figure 2.12 [11], [13].

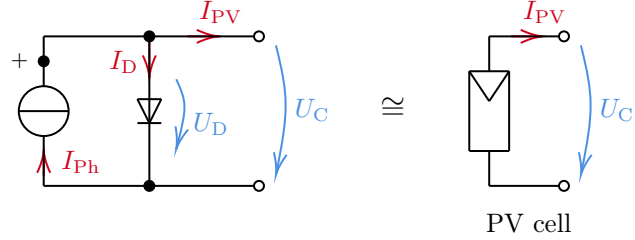


Figure 2.12: Simplified standard model of a photovoltaic cell. (Recreated from: [11], [13])

After applying Kirchoff's first and second law to the simplified standard model, considering the equation (2.35) and taking into account that the PV generator's current-voltage characteristic depends on the PV cell temperature ϑ_C and the radiation flux Φ_G , it can be modeled with the equations (2.36) and (2.37).¹⁶

$$I_{PV}(U_{PV}, \vartheta_C, \Phi_G) = I_{Ph} - \underbrace{I_S \left(\exp \left(\frac{U_{PV}}{m N_C U_T} \right) - 1 \right)}_{I_D} \quad (2.36)$$

$$U_{PV}(I_{PV}, \vartheta_C, \Phi_G) = m N_C U_T \ln \left(\frac{I_{Ph} - I_{PV} + I_S}{I_S} \right) \quad (2.37)$$

The diode's *thermal voltage* $U_T = U_T(\vartheta_C)$ in (V), with $k_B = 1,380649 \cdot 10^{-23} \text{WsK}^{-1}$ being the *Bolzmann constant* and $e = 1,602176634 \cdot 10^{-19} \text{As}$ being the *elementary charge*, can be obtained from the equation (2.38).

$$U_T(\vartheta_C) = \frac{k_B (\vartheta_C + 273, 15^\circ\text{C})}{e} \cdot \frac{1\text{K}}{1^\circ\text{C}} \quad (2.38)$$

m in (1) is the *ideality factor* with the condition $\{m \in \mathbb{R}^+ \mid 2 \geq m \geq 1\}$. It is an empirical value that is used to model the PV cells more precisely.¹⁷ The quantities $I_S = I_S(\vartheta_C)$ in (A) and $I_{Ph} = I_{Ph}(\vartheta_C, \Phi_G)$ in (A) are the diode's *reverse saturation current* and the PV cell's *photocurrent* [11], [13], [39], [47], [48].

Based on the equation (2.36), the modeled current-voltage characteristic can be visualized as shown in the figure 2.13, where $I_{SC}(\vartheta_C, \Phi_G)$ in (A) and $U_{OC}(\vartheta_C, \Phi_G)$ in (V) are the PV generator's *short-circuit current* and *open-circuit voltage*. MPP is the *maximum power point* for which the PV generator provides the greatest electrical power in (W), with $U_{MPP}(\vartheta_C, \Phi_G)$ being the voltage and $I_{MPP}(\vartheta_C, \Phi_G)$ being the current at MPP [11], [13], [39]:

$$P_{MPP}(\vartheta_C, \Phi_G) = U_{MPP} I_{MPP}. \quad (2.39)$$

¹⁵This model can be derived from the PV cell standard model for $R_P \rightarrow \infty$ and $R_S = 0\Omega$.

¹⁶Equation (2.37) can be derived from equations (2.36).

¹⁷For $m = 1$, I_D is Shockley's equation.

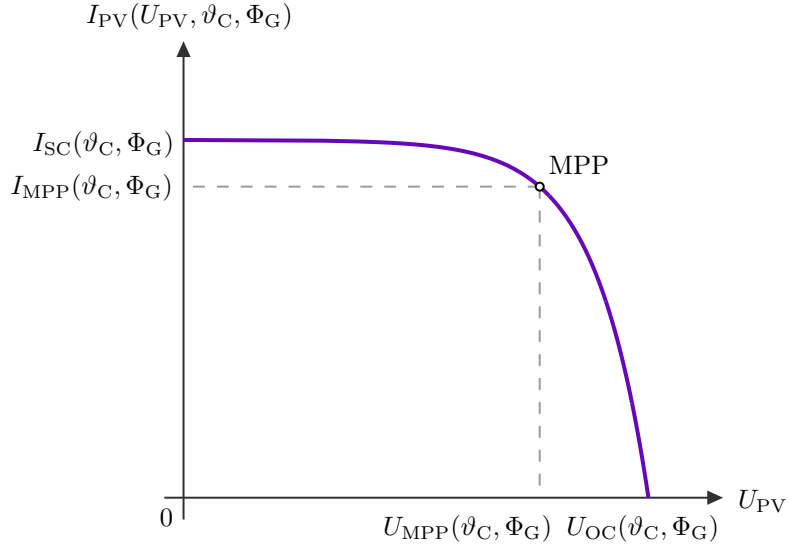


Figure 2.13: Modeled current-voltage characteristic of a photovoltaic generator, depending on the radiation flux Φ_G and the photovoltaic cell temperature ϑ_C . (Recreated from: [11], [13])

The quantity in the simplified standard model that changes with the solar radiation is the photocurrent. It is proportional to the radiation flux Φ_G , with $S = \text{const.}$ in (AW^{-1}) being the sensitivity of the PV cell:

$$I_{\text{Ph}}(\vartheta_{\text{STC}}, \Phi_G) = S \Phi_G. \quad (2.40)$$

From the case $I_{\text{PV}}(0\text{V}, \vartheta_{\text{STC}}, \Phi_{\text{STC}}) = I_{\text{SC,STC}}$, the sensitivity can be obtained as shown in the equation (2.41).

$$S = \frac{I_{\text{SC,STC}}}{\Phi_{\text{STC}}} \quad (2.41)$$

For the *standard test conditions* (STC), listed in the table 2.2, $I_{\text{SC,STC}}$ can be taken directly from the data sheet of a PV generator and Φ_{STC} in (W) can be calculated using the equation (2.20). In this equation, A_{PV} can either be measured or taken from a PV generator's data sheet as well. After substituting equation (2.41) into equation

Standard test conditions for PV generators	
Total irradiance received by the PV generator	$E_{\text{STC}} = 1000 \text{ Wm}^{-2}$
PV cell temperature	$\vartheta_{\text{STC}} = 25^\circ\text{C}$
Solar spectrum	AM 1,5

Table 2.2: Parameters for the standard test conditions of a photovoltaic generator [11].

(2.40) and taking the *temperature coefficient* of the short circuit current $\text{TC}(I_{\text{SC}})$ in ($\%^\circ\text{C}^{-1}$) into account, the photocurrent, depending on the PV cell temperature and the radiation flux, follows to:

$$I_{\text{Ph}}(\vartheta_C, \Phi_G) = \underbrace{I_{\text{SC,STC}}}_{I_{\text{Ph}}(\vartheta_{\text{STC}}, \Phi_G)} \frac{E_G}{E_{\text{STC}}} \left[1 + \frac{\text{TC}(I_{\text{SC}})}{100\%} (\vartheta_C - \vartheta_{\text{STC}}) \right]. \quad (2.42)$$

$\text{TC}(I_{\text{SC}})$ can usually be taken from a PV generator's data sheet.¹⁸ Because $I_{\text{PV}}(0\text{V}, \vartheta_C, \Phi_G) = I_{\text{SC}}(\vartheta_C, \Phi_G)$, $I_{\text{SC}}(\vartheta_C, \Phi_G) = I_{\text{Ph}}(\vartheta_C, \Phi_G)$ applies [11], [13], [47].

¹⁸Typical $\text{TC}(I_{\text{SC}})$ values for Si-PV cells are around $0,06\%^\circ\text{C}^{-1}$.

Now that $I_{\text{Ph}}(\vartheta_C, \Phi_G)$ is known, the diode's reverse saturation current can be calculated from the case $I_{\text{PV}}(U_{\text{OC}}(\vartheta_C, \Phi_G), \vartheta_C, \Phi_G) = 0\text{A}$:

$$I_S(\vartheta_C) = I_{\text{Ph}}(\vartheta_C, \Phi_G) \left(\exp \left(\frac{U_{\text{OC}}(\vartheta_C, \Phi_G)}{m N_C U_T} \right) - 1 \right)^{-1}. \quad (2.43)$$

The open-circuit voltage $U_{\text{OC}}(\vartheta_C, \Phi_G)$ can be derived by subtracting the case $U_{\text{PV}}(0\text{A}, \vartheta_C, \Phi_G)$ from the case $U_{\text{PV}}(0\text{A}, \vartheta_C, \Phi_{\text{STC}})$ while taking the temperature coefficient of the open-circuit voltage $\text{TC}(U_{\text{OC}})$ in ($^{\circ}\text{C}^{-1}$) into account:

$$U_{\text{OC}}(\vartheta_C, \Phi_G) = U_{\text{OC}}(\vartheta_C, \Phi_{\text{STC}}) + m N_C U_T \ln \left(\frac{I_{\text{Ph}}(\vartheta_C, \Phi_G) + I_S(\vartheta_C)}{I_{\text{Ph}}(\vartheta_C, \Phi_{\text{STC}}) + I_S(\vartheta_C)} \right), \quad (2.44)$$

where $U_{\text{OC}}(\vartheta_C, \Phi_{\text{STC}})$ is the temperature dependent open-circuit voltage for the radiation flux Φ_{STC} at STC:

$$U_{\text{OC}}(\vartheta_C, \Phi_{\text{STC}}) = U_{\text{OC,STC}} \left[1 + \frac{\text{TC}(U_{\text{OC}})}{100\%} (\vartheta_C - \vartheta_{\text{STC}}) \right]. \quad (2.45)$$

In addition to $\text{TC}(I_{\text{SC}})$, $\text{TC}(U_{\text{OC}})$ can also be taken from a PV generators data sheet.¹⁹ Equation (2.44) is only valid because the reverse saturation current $I_S(\vartheta_C)$ does not depend on the radiation flux [11], [13], [47], [49].

Since the equations (2.43) and (2.44) are in a non-linear relationship to one another, the Newton-Raphson method must be used to approximate them numerically (see appendix B.2). For this, the functions $f_1(\mathbf{x}_R)$ and $f_2(\mathbf{x}_R)$ are introduced below. In the equation (2.46) an exponential function is used instead of a logarithmic function, since some numerical approximation algorithms do not converge for logarithmic functions.

$$\begin{aligned} f_1(\mathbf{x}_R) &= \exp \left(\frac{U_{\text{OC}}(\vartheta_C, \Phi_G) - U_{\text{OC}}(\vartheta_C, \Phi_{\text{STC}})}{m N_C U_T} \right) \\ &\quad - \frac{I_{\text{Ph}}(\vartheta_C, \Phi_G) + I_S(\vartheta_C)}{I_{\text{Ph}}(\vartheta_C, \Phi_{\text{STC}}) + I_S(\vartheta_C)} = 0 \end{aligned} \quad (2.46)$$

$$f_2(\mathbf{x}_R) = I_S(\vartheta_C) - I_{\text{Ph}}(\vartheta_C, \Phi_G) \left(\exp \left(\frac{U_{\text{OC}}(\vartheta_C, \Phi_G)}{m N_C U_T} \right) - 1 \right)^{-1} = 0\text{A} \quad (2.47)$$

The vector \mathbf{x}_R , shown in the equation (2.48), contains the zero crossings of the functions $f_1(\mathbf{x}_R)$ and $f_2(\mathbf{x}_R)$.

$$\mathbf{x}_R = \left(I_S(\vartheta_C), U_{\text{OC}}(\vartheta_C, \Phi_G) \right)^T \quad (2.48)$$

Furthermore, the vector $\mathbf{f}(\mathbf{x}_R) = \mathbf{0}$, which contains the functions from the equations (2.46) and (2.47), must be introduced for the Newton-Raphson method:

$$\mathbf{f}(\mathbf{x}_R) = \left(f_1(\mathbf{x}_R), f_2(\mathbf{x}_R) \right)^T = \mathbf{0}. \quad (2.49)$$

¹⁹Typical $\text{TC}(U_{\text{OC}})$ values for Si-PV cells are around $-0,40\text{ }^{\circ}\text{C}^{-1}$.

With the help of the Jacobian matrix $\mathbf{J} = \partial\mathbf{f}(\mathbf{x})/\partial\mathbf{x}$ for $\mathbf{x} = \mathbf{x}_R$, the $(n+1)^{\text{th}}$ approximation with $n \in \mathbb{N}$ can be determined as follows:

$$\mathbf{x}_{R,n+1} = \mathbf{x}_{R,n} - \mathbf{J}^{-1}(\mathbf{x}_{R,n}) \mathbf{f}(\mathbf{x}_{R,n}), \quad (2.50)$$

$$\mathbf{J} = \begin{pmatrix} \frac{\partial f_1(I_S(\vartheta_C), U_{OC}(\vartheta_C, \Phi_G))}{\partial I_S(\vartheta_C)} & \frac{\partial f_1(I_S(\vartheta_C), U_{OC}(\vartheta_C, \Phi_G))}{\partial U_{OC}(\vartheta_C, \Phi_G)} \\ \frac{\partial f_2(I_S(\vartheta_C), U_{OC}(\vartheta_C, \Phi_G))}{\partial I_S(\vartheta_C)} & \frac{\partial f_2(I_S(\vartheta_C), U_{OC}(\vartheta_C, \Phi_G))}{\partial U_{OC}(\vartheta_C, \Phi_G)} \end{pmatrix}. \quad (2.51)$$

Starting values for the Newton-Raphson method can be obtained from the expressions in the equation (2.52), if it is accepted that the diode's reverse saturation current I_S is small compared to the photocurrent I_{Ph} , so that $I_S + I_{\text{Ph}} \approx I_{\text{Ph}}$ applies.²⁰

$$U_{OC,0}(\vartheta_C, \Phi_G) = U_{OC}(\vartheta_C, \Phi_{\text{STC}}) + m N_C U_T \ln \left(\frac{I_{\text{Ph}}(\vartheta_C, \Phi_G)}{I_{\text{Ph}}(\vartheta_C, \Phi_{\text{STC}})} \right),$$

$$I_{S,0}(\vartheta_C) = I_{\text{Ph}}(\vartheta_C, \Phi_G) \exp \left(-\frac{U_{OC,0}(\vartheta_C, \Phi_G)}{m N_C U_T} \right), \quad (2.52)$$

for $I_S \ll I_{\text{Ph}}$

With these, the starting vector $\mathbf{x}_{R,0} = (I_{S,0}(\vartheta_C), U_{OC,0}(\vartheta_C, \Phi_G))^T$ for the first iteration can be obtained. Finally, it has to be mentioned that the functions $f_1(\mathbf{x}_R)$ and $f_2(\mathbf{x}_R)$ are continuously differentiable for the required number of iteration steps $n+1$. This is a requirement for the Newton-Raphson method [11], [13], [50]–[53].

The PV cell temperature ϑ_C , depending on the irradiance E_G and the *ambient temperature* ϑ_A in ($^{\circ}\text{C}$), with the *nominal operating cell temperature*²¹ NOCT in ($^{\circ}\text{C}$) and the conditions under which it is measured, $\vartheta_{A,\text{NOCT}}$ in ($^{\circ}\text{C}$) and E_{NOCT} in (Wm^{-2}), can be approximated by assuming that the increase of ϑ_C , compared to the ambient temperature ϑ_A , is proportional to E_G :

$$\vartheta_C \approx \vartheta_A + (\text{NOCT} - \vartheta_{A,\text{NOCT}}) \frac{E_G}{E_{\text{NOCT}}}. \quad (2.53)$$

The parameters under which the NOCT is measured are provided by the table 2.3 and the NOCT is usually listed in the data sheet of a PV generator [11].

Conditions for NOCT measurement	
Total irradiance received by the PV generator	$E_{\text{NOCT}} = 800 \text{ Wm}^{-2}$
Ambient temperature	$\vartheta_{A,\text{NOCT}} = 20^{\circ}\text{C}$
Wind speed	$v_W = 1 \text{ ms}^{-1}$

Table 2.3: Conditions under which the NOCT is measured [11].

Ambient temperatures ϑ_A for different locations on Earth can be obtained from climate charts. For example, figure 2.14 presents monthly averages for the ambient

²⁰These expressions can be derived from the equations (2.44) and (2.43).

²¹Typical NOCT values for c-Si-PV generators are around 45 to 50°C.

temperature in ($^{\circ}\text{C}$) and precipitation in (mm) collected by the Global Historical Climatology Network for the Hohe Warte in Vienna, Austria, between 1997 and 2016. Below the chart, the percentage of missing data regarding the months of the year is presented [54].

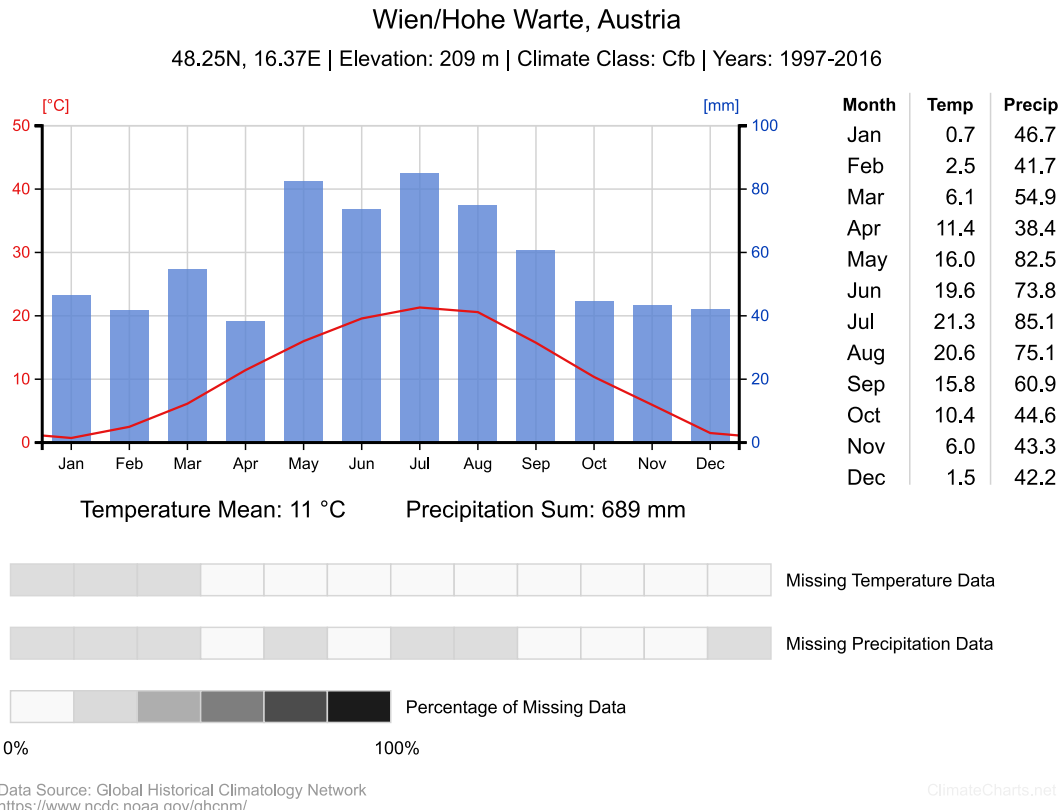


Figure 2.14: Monthly averages of temperature and precipitation data for the Hohe Warte in Vienna, Austria. (Image credit: [54])

Building on the previous findings, the electrical power output of a PV generator can be calculated by using one of the following equations:

$$P_{\text{PV}}(I_{\text{PV}}, \vartheta_{\text{C}}, \Phi_{\text{G}}) = m N_{\text{C}} U_{\text{T}} I_{\text{PV}} \ln \left(\frac{I_{\text{Ph}} - I_{\text{PV}} + I_{\text{S}}}{I_{\text{S}}} \right), \quad (2.54)$$

$$P_{\text{PV}}(U_{\text{PV}}, \vartheta_{\text{C}}, \Phi_{\text{G}}) = U_{\text{PV}} \left[I_{\text{Ph}} - I_{\text{S}} \left(\exp \left(\frac{U_{\text{PV}}}{m N_{\text{C}} U_{\text{T}}} \right) - 1 \right) \right]. \quad (2.55)$$

Typically, P_{PV} is plotted as a function of U_{PV} , which results in a curve as shown in the figure 2.15 [11], [13], [39].

2.3.7 MPP tracking solar charging controllers

The aim of a SCC is to distribute a PV generator's electrical energy to supply one or more electrical consumers and to recharge an electrochemical energy storage device. The latter is required to supply electrical consumers during times without sunlight. SCCs that can track the MPP of a PV generator, thus providing the greatest electrical energy to the load and the electrochemical energy storage device (compare to figure 2.3), determine the current $I_{\text{MPP}}(\vartheta_{\text{C}}, \Phi_{\text{G}})$ and voltage $U_{\text{MPP}}(\vartheta_{\text{C}}, \Phi_{\text{G}})$. This

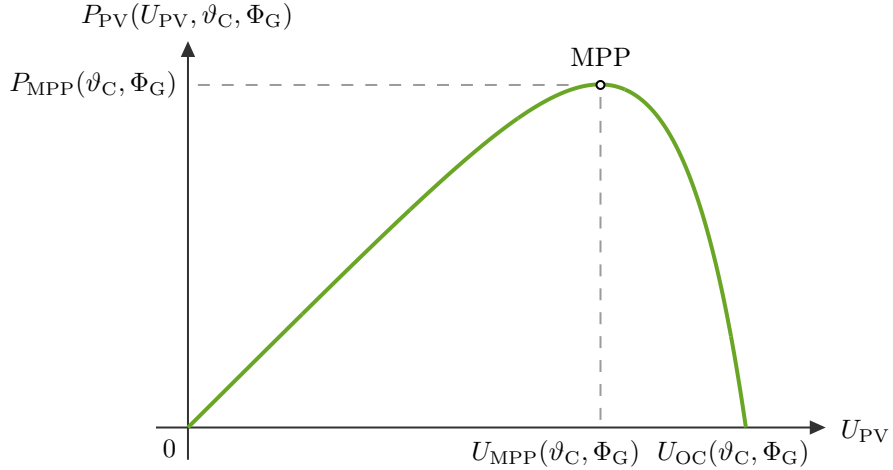


Figure 2.15: Electrical power output of a photovoltaic generator as a function of U_{PV} . It is further dependent on the photovoltaic cell temperature ϑ_{C} and the radiation flux Φ_{G} . (Recreated from: [11])

can be accomplished by analyzing the equation (2.54) from which the derivative of $P_{\text{PV}}(I_{\text{PV}}, \vartheta_{\text{C}}, \Phi_{\text{G}})$, with respect to I_{PV} , results in the equation (2.56).

$$\frac{dP_{\text{PV}}(I_{\text{PV}}, \vartheta_{\text{C}}, \Phi_{\text{G}})}{dI_{\text{PV}}} = m N_{\text{C}} U_{\text{T}} \left(\ln \left(\frac{I_{\text{Ph}} - I_{\text{PV}} + I_{\text{S}}}{I_{\text{S}}} \right) - \frac{I_{\text{PV}}}{I_{\text{Ph}} - I_{\text{PV}} + I_{\text{S}}} \right) \quad (2.56)$$

Since the slope of the curve $P_{\text{PV}}(I_{\text{PV}}, \vartheta_{\text{C}}, \Phi_{\text{G}})$ becomes 0V for its maxima, $I_{\text{PV}} = I_{\text{MPP}}$ applies as shown below:

$$m N_{\text{C}} U_{\text{T}} \left(\ln \left(\frac{I_{\text{Ph}} - I_{\text{MPP}} + I_{\text{S}}}{I_{\text{S}}} \right) - \frac{I_{\text{MPP}}}{I_{\text{Ph}} - I_{\text{PV}} + I_{\text{S}}} \right) = 0\text{V}. \quad (2.57)$$

If now the equation (2.57) is subtracted from the equation (2.37) for the case $U_{\text{PV}}(I_{\text{MPP}}, \vartheta_{\text{C}}, \Phi_{\text{G}}) = U_{\text{MPP}}(\vartheta_{\text{C}}, \Phi_{\text{G}})$, the voltage at MPP can be rewritten as follows [11], [13]:

$$U_{\text{MPP}}(I_{\text{MPP}}, \vartheta_{\text{C}}, \Phi_{\text{G}}) = \frac{m N_{\text{C}} U_{\text{T}} I_{\text{MPP}}}{I_{\text{Ph}} - I_{\text{MPP}} + I_{\text{S}}}. \quad (2.58)$$

In addition to the equation (2.39), $P_{\text{MPP}}(\vartheta_{\text{C}}, \Phi_{\text{G}})$ can directly be obtained from Φ_{G} as presented in the equation (2.59). For this, however, the PV generator's efficiency η_{PV} in (1) and its temperature coefficient $\text{TC}(P_{\text{MPP}})$ in ($\%^{\circ}\text{C}^{-1}$) for the electrical power output at MPP must be known.²² These quantities can be found in the data sheet of a PV generator.

$$P_{\text{MPP}}(\vartheta_{\text{C}}, \Phi_{\text{G}}) = \eta_{\text{PV}} \Phi_{\text{G}} \left[1 + \frac{\text{TC}(P_{\text{MPP}})}{100\%} (\vartheta_{\text{C}} - \vartheta_{\text{STC}}) \right] \quad (2.59)$$

Alternatively, η_{PV} can be calculated by using the equation (2.59) and the table 2.2, while regarding the expression $P_{\text{MPP,STC}} = U_{\text{MPP,STC}} I_{\text{MPP,STC}}$. This is because η_{PV} depends exclusively on the material and the structure of a PV cell. Moreover, it is assumed that the PV cell is ideal and that every photon which hits the semiconductor and fulfills $W_{\text{Ph}} > \Delta W_{\text{gap}}$, is absorbed and leads to an electron which contributes to

²²Typical $\text{TC}(P_{\text{MPP}})$ values for Si-PV cells are around $-0,4$ to $-0,5 \, \%^{\circ}\text{C}^{-1}$.

I_{Ph} . In the mentioned inequality W_{Ph} is the *energy of a photon* in (eV) and ΔW_{gap} is the *band gap* in (eV) of the semiconductor [11], [13].

With the equations (2.39), (2.58) and (2.59), the PV generator's current at MPP can be converted into the following quadratic equation:

$$I_{\text{MPP}}^2 + c_{\text{PV}} I_{\text{MPP}} - c_{\text{PV}} (I_{\text{Ph}} + I_{\text{S}}) = 0 \text{ A}^2, \quad (2.60)$$

with c_{PV} being:

$$c_{\text{PV}} = \frac{\eta_{\text{PV}} \Phi_{\text{G}} \left[1 + \frac{\text{TC}(P_{\text{MPP}})}{100\%} (\vartheta_{\text{C}} - \vartheta_{\text{STC}}) \right]}{m N_{\text{C}} U_{\text{T}}}. \quad (2.61)$$

Finally, $I_{\text{MPP}}(\vartheta_{\text{C}}, \Phi_{\text{G}})$ can be solved to:

$$I_{\text{MPP}}(\vartheta_{\text{C}}, \Phi_{\text{G}}) = \sqrt{\frac{c_{\text{PV}}^2}{4} + c_{\text{PV}} (I_{\text{Ph}} + I_{\text{S}}) - \frac{c_{\text{PV}}}{2}}. \quad (2.62)$$

The PV generator's voltage at MPP can consequently be calculated using the equation (2.36) for the case $U_{\text{PV}}(I_{\text{MPP}}, \vartheta_{\text{C}}, \Phi_{\text{G}})$, or using the equation (2.58).

Due to the fact that real MPP tracking SCCs do not have information about the connected PV generator, a *shunt resistor* R_{shunt} in (Ω) is used to find the MPP. A charging- and MPP-controller inside the SCC then controls the *duty cycle* a in (%) of a DC/DC converter, so that the load and the electrochemical energy storage device are supplied with the greatest electrical energy. An illustration of the basic structure of such a MPP tracking SCC can be seen in the figure 2.16. I_{SCC} in (A) is the current that is consumed by the charging- and MPP-controller [11].

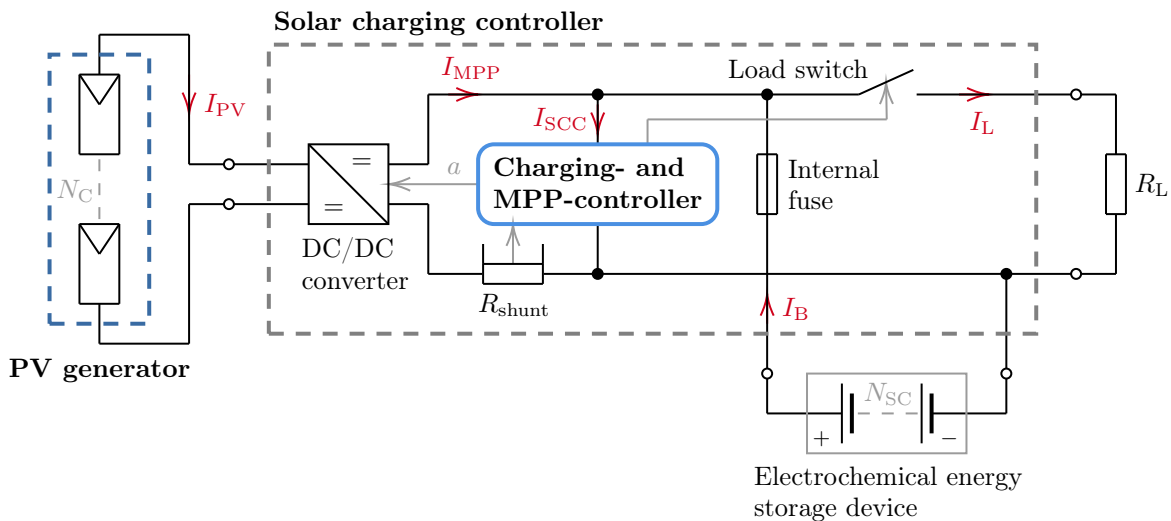


Figure 2.16: The basic structure of a maximum power point tracking solar charging controller. (Recreated from: [11])

2.3.8 Electrochemical energy storage

In order to guarantee a constant supply of electrical energy during times when the PV generator cannot supply the self-sufficient voice communication system, an

electrochemical energy storage device is required. Such storage devices are typically rechargeable batteries – consisting of secondary cells – based on either lithium, sodium, nickel or lead [11], [14], [15].

Nickel-cadmium (NiCd) and *nickel-hydrogen* (NiH₂) batteries have long been used for aerospace applications. However, in recent years they have been increasingly replaced by lithium-ion batteries [26]. This is due to their high energy density and low self-discharge. On the other hand, the main disadvantages of lithium-ion batteries are high acquisition costs, the need for a *battery management system* (BMS) to maintain safe operation and the strong dependency of the battery performance on the ambient temperature ϑ_A . The latter becomes a problem only at extreme ambient temperatures [55]–[59].

In terms of safe operation, *lithium iron phosphate* (LiFePO₄) batteries are among the safest lithium-ion batteries available today. They are furthermore non-toxic²³ and have a very constant cell voltage for different charging states (see linear part in figure 2.18). It is noted that for the *state of charge* SOC = 1 the battery is fully charged and for SOC = 0 it is fully discharged [11], [14], [15], [60]–[63].

Because LiFePO₄ batteries are commercially available and often used with photovoltaic standalone systems, this subsection aims to model the *terminal voltage* $U_B = U_B(\text{SOC})$ in (V) of such a battery for a given current $I_B = I_B(t)$, based on an experimental approach [11], [63]. For this purpose, $I_B(t)$ is defined as shown below:

$$I_B(t) = \begin{cases} I_D(t), & \text{when discharging the battery} \\ -I_C(t), & \text{when charging the battery.} \end{cases} \quad (2.63)$$

Following from the equation (2.91), the SOC of a battery as a function of the discharge or charge *time* t in (h) can be calculated directly from the *Coulomb counting method* in the equation (2.64).

$$\begin{aligned} \text{SOC}(t) &= \text{SOC}_{\text{init}} - \frac{\eta_C}{Q_{\text{tot}}} \int_{0\text{h}}^t I_B(\tau) \, d\tau \\ \text{SOC}(t) &= \text{SOC}_{\text{init}} - \frac{\eta_C}{Q_{\text{tot}}} \sum_{\tau=0\text{h}}^t I_B(\tau) \Delta\tau \end{aligned} \quad (2.64)$$

SOC_{init} in (1) is the *initial SOC* of the battery. It can be calculated by the ratio of the *remaining battery charge* Q_{rem} in (Ah) to the *total available battery charge* Q_{tot} in (Ah) as written in the equation (2.65). η_C is the *coulombic efficiency* in (1) for which $\eta_C = 1$ applies when discharging and $\eta_C \leq 1$ applies when charging [15], [56], [58], [60], [64]. In the proposed model it is assumed that $\eta_C = 1$ applies for both cases [61], [65], [66].

$$\text{SOC}_{\text{init}} = \frac{Q_{\text{rem}}}{Q_{\text{tot}}} \quad (2.65)$$

According to the authors of [15], [55], [67], the total available battery charge Q_{tot} when discharging depends on the *discharging current* I_D in (A). During charging – with the *charging current* I_C in (A) – Q_{tot} is equal to the *nominal battery charge*

²³Compared to, for example, *lithium cobalt oxide* (LiCoO₂) batteries.

Q_{nom} in (Ah). This empirical approximation is summarized in the equation (2.66), in which $k_P \approx 1,05$ is the *Peukert constant* for lithium-ion batteries and Q_{nom} can be taken from the data sheet of a LiFePO₄ battery [15], [55].

$$Q_{\text{tot}} \approx \begin{cases} Q_{\text{nom}} \left(\frac{I_{\text{nom}}}{I_D} \right)^{k_P-1}, & \text{when discharging the battery} \\ Q_{\text{nom}}, & \text{when charging the battery} \end{cases} \quad (2.66)$$

Since Q_{nom} depends on the *discharging rate* C_D in (h^{-1}), which is listed in the data sheet as well, the *nominal battery current* I_{nom} in (A) can be calculated as follows [15], [68]:

$$I_{\text{nom}} = C_D Q_{\text{nom}}. \quad (2.67)$$

From the above it can now be concluded that the *battery charge* as a function of the time $Q_B(t)$ in (Ah) must result in:

$$Q_B(t) = \text{SOC } Q_{\text{tot}}. \quad (2.68)$$

The simplest EEC model of a LiFePO₄ battery is an ideal voltage source. Although this model is easy to implement and compute in simulations, it lacks important properties such as the dynamical behavior of the battery's open-circuit voltage $U_0 = U_0(\text{SOC})$ in (V), electrolyte resistance when discharging $R_{e,D} = R_{e,D}(\text{SOC})$ in (Ω) and electrolyte resistance when charging $R_{e,C} = R_{e,C}(\text{SOC})$ in (Ω). To incorporate these properties and improve accuracy while keeping the model simple, the R_{int} model shown in the figure (2.17) is used. The diodes in this model are assumed to be ideal and are only present to illustrate which resistor is used depending on the sign of I_B [56], [61], [64], [67].

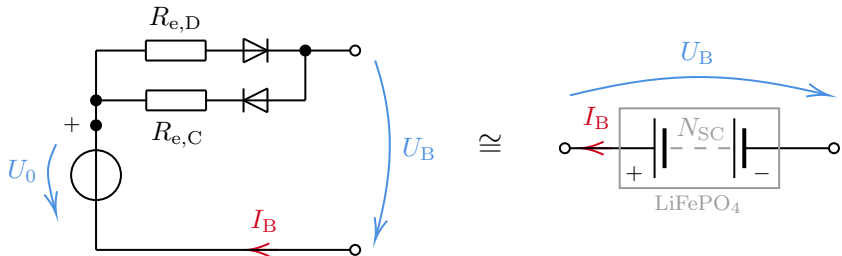


Figure 2.17: R_{int} model of a LiFePO₄ battery (electrochemical energy storage device). (Recreated from: [61], [67])

Figure 2.18 shows the typical behavior of the open-circuit voltage U_0 of a LiFePO₄ battery as a function of the SOC. For the electrolyte resistances $R_{e,D}(\text{SOC})$ and $R_{e,C}(\text{SOC})$, however, it is more difficult to create a generalized function curve. This is due to their varying behavior for different LiFePO₄ batteries [11], [14], [60]–[62].

On this basis, the terminal voltage of the battery U_B as a function of the SOC, and whether it is being discharged or charged, can be obtained after Kirchhoff's second law is applied to the model [56], [61], [64], [67]:

$$U_B(\text{SOC}) = \begin{cases} U_0 - R_{e,D} I_D, & \text{when discharging the battery} \\ U_0 + R_{e,C} I_C, & \text{when charging the battery.} \end{cases} \quad (2.69)$$

At this point it must be made clear that a LiFePO₄ battery is completely discharged when the voltage $U_B = U_{\text{cut-off}}$ is reached and fully charged when the voltage

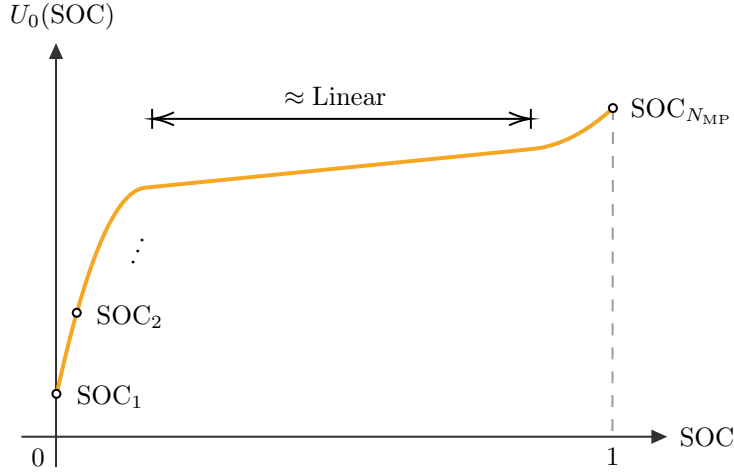


Figure 2.18: Typical behavior of the open-circuit voltage U_0 of a LiFePO₄ battery depending on the SOC. SOC₁ to SOC_{N_{MP}} represent the measuring points for the discharging and charging experiment. (Recreated from: [11], [14], [60]–[62])

$U_B = U_{\text{full}}$ is reached [61], [63].²⁴ If the equations (2.69) and (2.66) are compared, it can be seen that $U_{\text{cut-off}}$ is reached at a later point in time for smaller currents I_D . This shows that the battery can be discharged more deeply, which manifests itself in a larger total available battery charge Q_B [15], [55]. Here, however, the compromise is made that the cut-off voltage in the proposed model varies for different discharging currents.

Figure 2.19 shows the behavior of the battery voltage $U_B(t)$ when it is discharged with a constant current I_D over the time interval $\Delta t_D = t_{D,\text{off}} - t_{D,\text{on}}$ in (h) and then charged with the constant current I_C over the time interval $\Delta t_C = t_{C,\text{off}} - t_{C,\text{on}}$ in (h) [15], [60], [62], [65]–[67], [69]. From the *dropping voltages* $\Delta U_D(t_{D,\text{on}})$ and $\Delta U_C(t_{C,\text{off}})$ or *rising voltages* $\Delta U_D(t_{D,\text{off}})$ and $\Delta U_C(t_{C,\text{on}})$ in (V), the R_{int} model's electrolyte resistances $R_{e,D}$ and $R_{e,C}$ can be calculated as shown in the equations (2.70) and (2.71) [15], [65], [66], [69].

$$R_{e,D}(t) = \left| \frac{\Delta U_D}{I_D} \right| \quad (2.70)$$

$$R_{e,C}(t) = \left| \frac{\Delta U_C}{I_C} \right| \quad (2.71)$$

For comparison, the thin turquoise curve represents the behavior of the R_{int} model for the same discharge and charge currents I_D and I_C . At times $t_{D,\text{on}}$, $t_{D,\text{off}}$, $t_{C,\text{on}}$ and $t_{C,\text{off}}$ it has the same dropping and rising voltages ΔU_D and ΔU_C as $U_B(t)$ [67].

Based on the findings in the articles [55], [57]–[59] it is assumed that U_0 , $R_{e,D}$ and $R_{e,C}$ do not depend on the ambient temperature ϑ_A in the range from 5°C to 45°C. Therefore, the proposed model does not apply to temperatures below 5°C and above 45°C.

In order to complete the R_{int} model, the missing properties $U_0(\text{SOC})$, $R_{e,D}(\text{SOC})$ and $R_{e,C}(\text{SOC})$ must be determined experimentally. For this purpose, two separate experiments must be carried out as explained in the following paragraphs.

²⁴The name *cuf-off voltage* comes from the fact that the BMS turns off the battery to avoid an unsafe state.

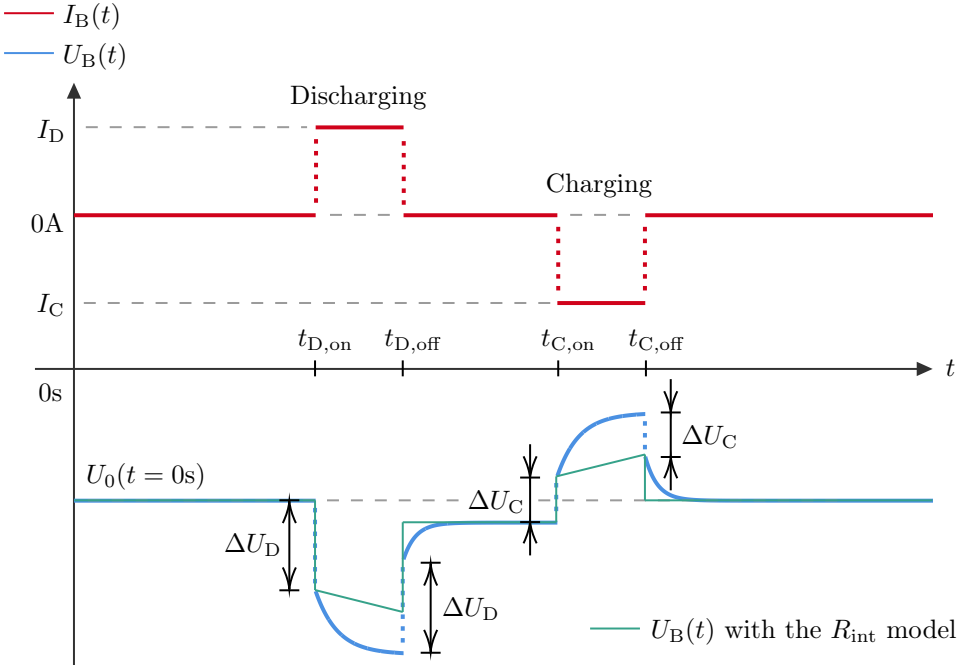


Figure 2.19: Behavior of the battery voltage $U_B(t)$ when it is first discharged with I_D and then charged with I_C . From the resulting voltage drop $\Delta U_D(t_{D,\text{on}})$ and voltage rise $\Delta U_C(t_{C,\text{on}})$, the R_{int} model's electrolyte resistances $R_{e,D}$ and $R_{e,C}$ can be calculated. The turquoise curve represents the behavior of the modeled battery voltage. (Recreated from: [15], [60], [62], [65]–[67], [69])

Discharging experiment:

The experiment is carried out at the ambient temperature $\vartheta_A = 25^\circ\text{C}$ with an initially fully charged LiFePO₄ battery ($\text{SOC}_{N_{\text{MP}}} = 1$) and repeated for the desired number of measuring points N_{MP} in (1), as illustrated in the figure 2.18, until the battery is fully discharged ($\text{SOC}_1 = 0$) [65], [66], [69].

A simple measurement setup for this experiment can be seen in the figure 2.20. U_{shunt} in (V) is the voltage drop across the shunt resistor R_{shunt} , measured with channel 2 (Ch2) of the oscilloscope. On the basis of this voltage drop, I_L is set so that the battery is discharged with the current:

$$I_D = \frac{U_{\text{shunt}}}{R_{\text{shunt}}} + I_{\text{Ch1}} + I_{\text{Ch2}}. \quad (2.72)$$

The measuring currents I_{Ch1} and I_{Ch2} in (A) caused by the internal resistances of the channels of the oscilloscope are small compared to the load current I_L . Depending on the desired accuracy, I_{Ch1} and I_{Ch2} can either be neglected or determined by measuring the internal resistances of said channels [41].

For a certain measuring point $n \in \mathbb{N}$, the battery's open-circuit voltage $U_{0,D}(\text{SOC}_n)$ in (V) is measured with channel 1 (Ch1) of the oscilloscope. The battery is then discharged using an electronic load in constant current (CC) mode²⁵ with I_D for Δt_D until the desired new measuring point SOC_{n-1} is reached. At the point in time when the electronic load is switched on, the voltage drop $\Delta U_D(\text{SOC}_n)$ is measured

²⁵Even if the battery voltage slowly drops during the course of the experiment, the electronic load will keep the current constant.

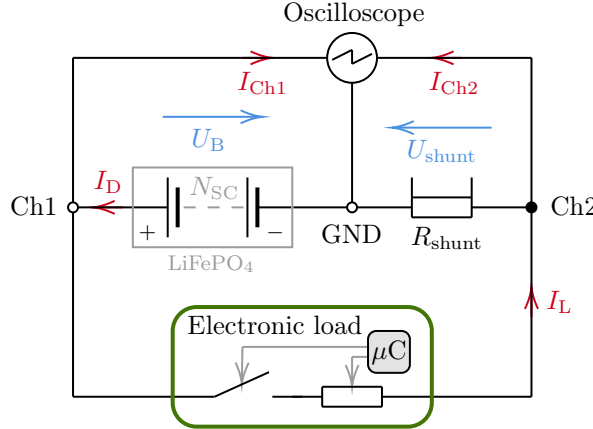


Figure 2.20: Measurement setup for the discharge experiment.

with Ch1 and the voltage drop $U_{\text{shunt}}(\text{SOC}_n)$ with Ch2. After the discharge process for Δt_D has been completed, the battery must remain idle for the *resting period* t_{rest} in (h) until the open-circuit voltage has reached an end value (compare to figure 2.19). When it is reached, the measurements can be repeated for SOC_{n-1} . For the measuring point SOC_1 , the load current I_L can be switched off immediately after the voltage drop ΔU_D , so that the BMS does not have to switch off the secondary cells [65], [66], [69].

From the Coulomb counting method, the time interval Δt_D , which in the course of the experiment can be measured with a timer, and the measuring points can be calculated as follows [15], [56], [58], [60], [64]:

$$\Delta t_D = \frac{Q_{\text{tot}}}{\eta_C I_D (N_{\text{MP}} - 1)}. \quad (2.73)$$

$$\text{SOC}_{n-1} = \text{SOC}_n - \frac{\eta_C I_D}{Q_{\text{tot}}} \Delta t_D. \quad (2.74)$$

Finally, if ΔU_D and U_{shunt} are known for the measuring points SOC_1 to $\text{SOC}_{N_{\text{MP}}}$, the resistance $R_{e,D}$ can be calculated by using the equation (2.75) – which is derived from the equations (2.70) and (2.72) [15], [65], [66], [69].

$$R_{e,D}(\text{SOC}_n) = \left| \frac{\Delta U_D(\text{SOC}_n)}{\frac{U_{\text{shunt}}(\text{SOC}_n)}{R_{\text{shunt}}} + I_{\text{Ch1}} + I_{\text{Ch2}}} \right| \quad (2.75)$$

Charging experiment:

Before the course of the experiment is explained, it must first be clarified how a LiFePO₄ battery behaves when charging. Lithium-ion batteries are usually charged with the *constant current/constant voltage* (CC/CV) method. As presented in the figure 2.21, the battery is first charged with a constant current I_C for t_C in (h), for which the battery voltage is described with the equation (2.69), and then with a constant voltage $U_B(t) = U_{\text{full}}$ for t_V in (h). When the charging process is completed, the battery voltage drops to the so called *floating voltage* U_{float} in (V). This happens when the decreasing charging current I_B falls below a *minimum current* I_{\min} in (A) [11], [14], [15], [70], [71].

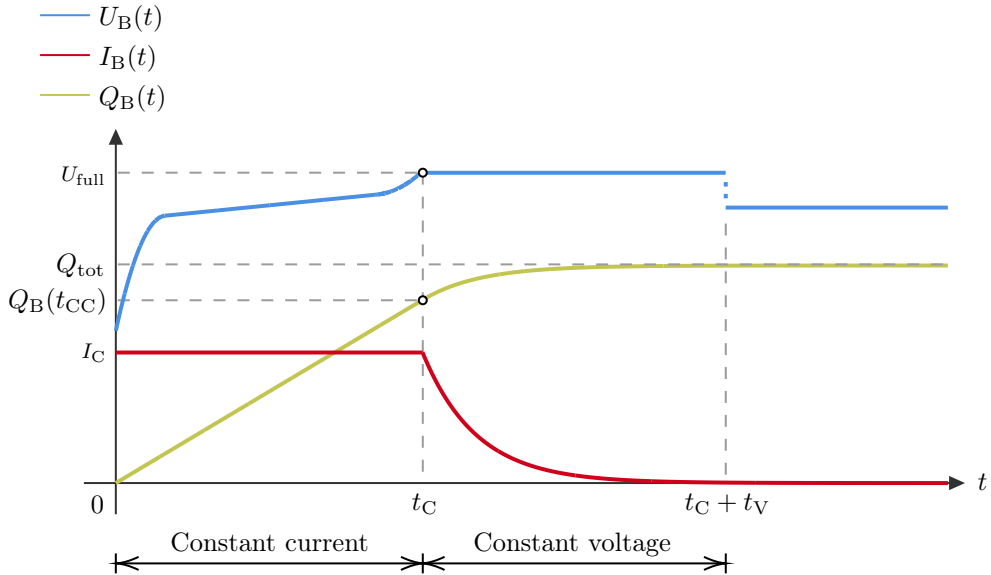


Figure 2.21: An example of the behavior the battery voltage $U_B(t)$, battery current $I_B(t)$ and battery charge $Q_B(t)$ of a LiFePO₄ battery when it is charged with a constant current I_C and then with a constant voltage U_{full} over a longer period of time. At $t_C + t_V$ the battery charger switches from U_{full} to U_{float} to keep the battery in a fully charged state. (Recreated from: [14], [70], [71])

With the *charge difference* $\Delta Q = Q_{\text{tot}} - Q_B(t_C)$ and the model proposed in [71], the battery charge can be written as a function of the charging time as follows:

$$Q_B(t) = \begin{cases} I_C t, & \text{for } 0h \leq t < t_C \\ \Delta Q \left(1 - \exp \left(-\frac{t - t_C}{\tau_B} \right) \right) + I_C t_C, & \text{for } t_C \leq t < t_C + t_V. \end{cases} \quad (2.76)$$

It is assumed that $Q_B(t)$ is continuously differentiable for all points in time. Based on this assumption, the model for the charging current results from the time derivative:

$$\frac{dQ_B(t)}{dt} = \begin{cases} I_C, & \text{for } 0h \leq t < t_C \\ \frac{\Delta Q}{\tau_B} \exp \left(-\frac{t - t_C}{\tau_B} \right), & \text{for } t_C \leq t < t_C + t_V \end{cases} = I_B(t). \quad (2.77)$$

If it is further assumed that $I_B(t)$ is continuous for all points in time – therefore does not drop at the point in time t_C – the *time constant* τ_B in (h) of a battery can be obtained from:

$$\tau_B = \frac{\Delta Q}{I_C}. \quad (2.78)$$

If – in the course of the charge experiment – it can be shown that the second assumption is correct, then the first assumption follows according to [52].

Like the discharge experiment, this experiment is also carried out at $\vartheta_A = 25^\circ\text{C}$. The LiFePO₄ battery, however, is initially fully discharged ($\text{SOC}_1 = 0$) and the charging experiment is repeated for the desired number of measuring points N_{MP} until it is fully charged ($\text{SOC}_{N_{\text{MP}}} = 1$) [65], [66], [69].

The corresponding measurement setup can be seen in the figure 2.22. For the currents $I_{\text{Ch}1}$ and $I_{\text{Ch}2}$ the same applies as in the discharge experiment since they are small compared to the *battery charger current* I_{BC} in (A) [41]. Based on the figure

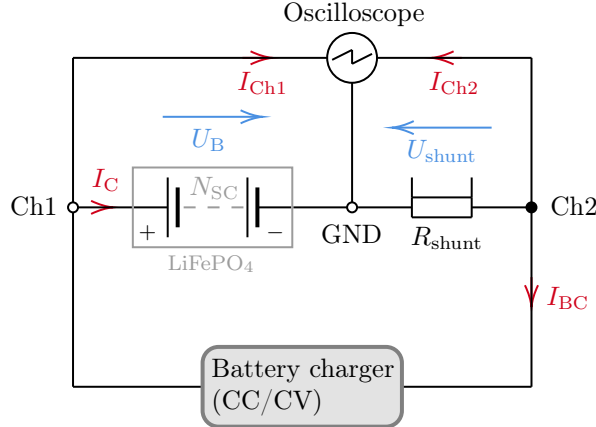


Figure 2.22: Measurement setup for the charge experiment.

2.22, the actual charging current I_C can be calculated with the equation (2.79).

$$I_C = -\frac{U_{\text{shunt}}}{R_{\text{shunt}}} - I_{\text{Ch1}} - I_{\text{Ch2}} \quad (2.79)$$

Identical to the discharge experiment, the battery's open-circuit voltage $U_{0,C}(\text{SOC}_n)$ in (V) is measured with Ch1. The battery is then charged using a suitable battery charger in (CC/CV) mode with a set I_C , I_{\min} , U_{full} and U_{float} . This is done for the time interval Δt_C until the new measuring point SOC_{n+1} is reached. At the point in time when the battery charger is switched on, the voltage rise $\Delta U_C(\text{SOC}_n)$ is measured with Ch1 and the voltage drop $U_{\text{shunt}}(\text{SOC}_n)$ with Ch2. After the charge process for Δt_C has been completed, the battery must remain idle for t_{rest} until the open-circuit voltage has reached an end value (compare to figure 2.19). When this value is reached, the measurements can be repeated for SOC_{n+1} [65], [66], [69]. Based on the previously introduced model $\Delta U_C(\text{SOC}_{N_{\text{MP}}})$ cannot be obtained. However, by performing the experiment on a commercially available LiFePO₄ battery, it was found that for longer resting periods t_{rest} , of up to a few hours, it accepts small charging currents I_C for a short interval Δt_C even for $\text{SOC}_{N_{\text{MP}}}$. It is assumed that this is the consequence of the slow – almost exponential – decrease of $U_{0,C}(\text{SOC}_{N_{\text{MP}}})$ (compare to figure 2.19) [15]. In this case, the equation (2.69) is not equal to U_{full} anymore.

To confirm the previously made assumption that $I_C(t)$ is continuous for all points in time, it is measured with Ch2 and calculated by using the equation (2.79) [11], [14], [15], [70], [71].

The time interval Δt_C and the measuring points are calculated – base on the Coulomb counting method – as shown below [15], [56], [58], [60], [64]:

$$\Delta t_C = \frac{Q_{\text{tot}}}{\eta_C I_C (N_{\text{MP}} - 1)}. \quad (2.80)$$

$$\text{SOC}_{n+1} = \text{SOC}_n + \frac{\eta_C I_C}{Q_{\text{tot}}} \Delta t_C. \quad (2.81)$$

Similar to $R_{e,D}$, $R_{e,C}$ can be obtained – by using the equations (2.71) and (2.79)

– from [15], [65], [66], [69]:

$$R_{e,C}(\text{SOC}_n) = \left| -\frac{\Delta U_C(\text{SOC}_n)}{\frac{U_{\text{shunt}}(\text{SOC}_n)}{R_{\text{shunt}}} + I_{\text{Ch1}} + I_{\text{Ch2}}} \right|. \quad (2.82)$$

Due to the hysteresis effects of the open-circuit voltage $U_0(\text{SOC}_n)$ mentioned in [56], [65]–[67], the battery voltage in the equation (2.69) must be adapted to the so-called zero-state hysteresis model:

$$U_B(\text{SOC}_n) = \begin{cases} U_0(\text{SOC}_n) + \frac{c_B}{2} - R_{e,D}(\text{SOC}_n) I_D, & \text{when discharging the battery} \\ U_0(\text{SOC}_n) + \frac{c_B}{2} + R_{e,C}(\text{SOC}_n) I_C, & \text{when charging the battery,} \end{cases} \quad (2.83)$$

with:

$$U_0(\text{SOC}_n) = \frac{U_{0,D}(\text{SOC}_n) + U_{0,C}(\text{SOC}_n)}{2}, \quad (2.84)$$

and c_B depending on the sign of I_B :

$$c_B = \begin{cases} |U_{0,C}(\text{SOC}_n) - U_{0,D}(\text{SOC}_n)| \cdot (-1), & \text{for } I_B > 0\text{A} \\ 0, & \text{for } I_B = 0\text{A} \\ |U_{0,C}(\text{SOC}_n) - U_{0,D}(\text{SOC}_n)|, & \text{for } I_B < 0\text{A}. \end{cases} \quad (2.85)$$

2.3.9 Cable losses

Cables are used to distribute the generated electrical energy in the self-sufficient voice communication system. The transport of the electrical charge Q in (As) in a cable, however, causes electrical losses which have to be considered with:

$$P_{\text{loss}}(\vartheta_A) = \left(\frac{dQ(A)}{dt} \right)^2 R_{\text{cable}}(\vartheta_A). \quad (2.86)$$

$I(A) = dQ(A)/dt$ represents the time throughput rate of the electrical charge shifted in a directed manner through the *cross-sectional area* A in (mm^2) of a cable. This corresponds to the electrical current I in (A) at the area A . The second factor $R_{\text{cable}}(\vartheta_A)$ in (Ω) is the *cable resistance* depending on the ambient temperature ϑ_A . It can be calculated with the equation (2.87), where l in (m) is the *length* of the cable, ϱ in ($\Omega \text{mm}^2 \text{m}^{-1}$) is the *specific resistance* and α in ($^\circ\text{C}^{-1}$) is the *temperature coefficient* of the material the cable is made of. ϑ_{ref} in ($^\circ\text{C}$) is the temperature for which ϱ applies.

$$R_{\text{cable}}(\vartheta_A) = \frac{\varrho l}{A} [1 + \alpha (\vartheta_A - \vartheta_{\text{ref}})] \quad (2.87)$$

For example, for $\vartheta_{\text{ref}} = 20^\circ\text{C}$ copper has a specific resistance of $\varrho_{\text{Cu},20} = 0,01673 \Omega \text{mm}^2 \text{m}^{-1}$ with a temperature coefficient of $\alpha = 4,3 \cdot 10^{-3} \text{ }^\circ\text{C}^{-1}$ [39], [72]. Cable heating by solar radiation is neglected due to the complexity of the subject.

2.3.10 Martian application

With regard to the usability of the modeled energy distribution for a self-sufficient voice communication system on the surface of Mars, roughly speaking, two main components have to be examined more closely. Namely the PV generator and the LiFePO₄ battery.

Since Mars, with an average distance of 1,524AU, is further away from the Sun than the Earth, the solar irradiance $E_{S,M}$ in (Wm^{-2}) at the top of its atmosphere is 56,9% less than that on Earth [25]:

$$E_{S,M} = \frac{\Phi_S}{4\pi \cdot (1,524 \cdot r_{SE})^2} = \frac{3,845 \cdot 10^{26} \text{W}}{4\pi \cdot (2,279871539 \cdot 10^{11} \text{m})^2} = 588,66 \frac{\text{W}}{\text{m}^2}. \quad (2.88)$$

Similar to the solar resource maps introduced in the subsection 2.3.2, the Solar irradiance data collected by NASA's Viking Lander VL1, shown in the figures 2.23 to 2.24, can be used to calculate the total generator irradiance on the Martian surface, based on the equations (2.13) and (2.19):

$$E_G(t_S) = E_{DHI} \frac{\cos \theta}{\sin \gamma_S} + E_{DIFH} \frac{1 + \cos \beta}{2} + E_{GHI} \frac{1 - \cos \beta}{2} \cdot ALB. \quad (2.89)$$

The quantities E_{DHI} , E_{DIFH} , E_{GHI} , θ and γ_S depend on the solar time t_S . As a first

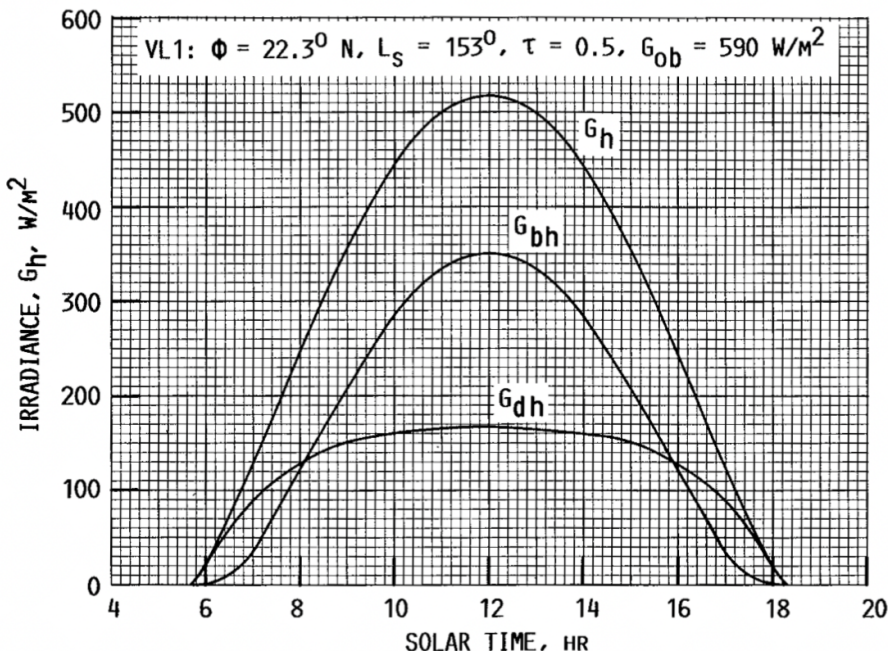


Figure 2.23: “Diurnal variation of global G_h , beam G_{bh} and diffuse G_{dh} irradiance on a horizontal Mars surface at Viking Lander VL1.” (Image and caption credit: [16])

approximation, the albedo value $ALB = 0,25$ can be used. This value represents the mean albedo of Mars [23]. In the article [16] the authors further state that the albedo of the Martian surface varies in the range of 0,1 to 0,4.

The data presented in the figures 2.23 to 2.24, however, only applies for the Martian latitude $\phi \cong \varphi = 22,3^\circ \text{N}$. Figure 2.23 shows the diurnal variation of

$E_{\text{DHI}} \hat{=} G_{\text{bh}}$, $E_{\text{DIFH}} \hat{=} G_{\text{dh}}$ and $E_{\text{GHI}} \hat{=} G_{\text{h}}$ on the Martian surface. The quantities L_s , τ and G_{ob} are the areocentric longitude, the optical depth and the beam irradiance at the top of the Martian atmosphere. Similar data is shown in the figures 2.24 and 2.25, but here an additional reference is made to the orbit of Mars around the Sun and the opacity of its atmosphere. For example, the latter can be caused by dust storms [16].

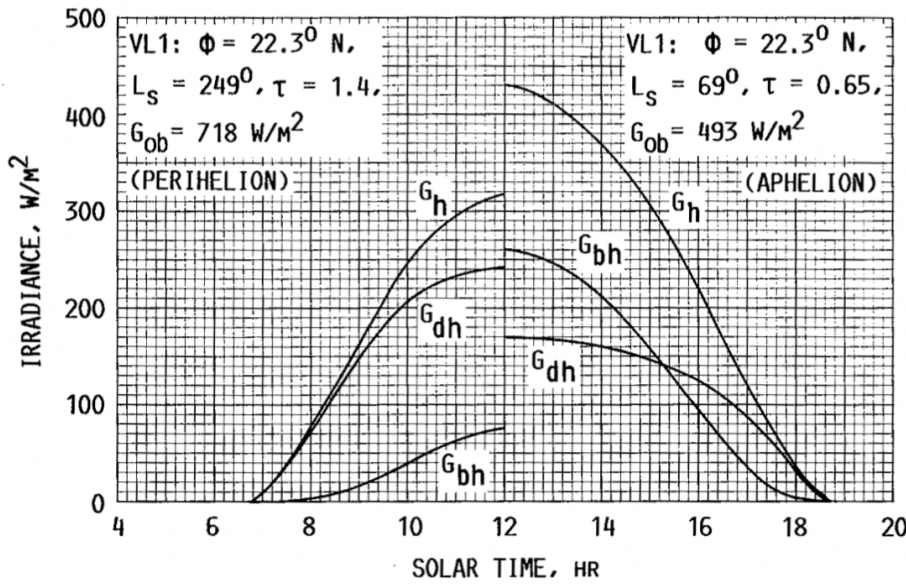


Figure 2.24: “Diurnal variation of global G_h , beam G_{bh} and diffuse G_{dh} irradiance on a horizontal Mars surface at Viking Lander VL1.” (Image and caption credit: [16])

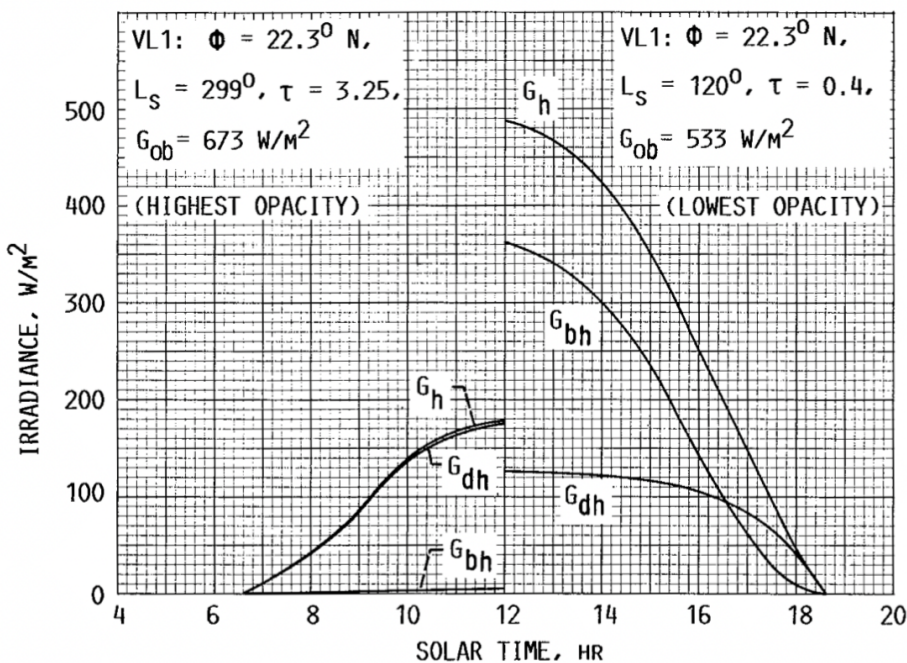


Figure 2.25: “Diurnal variation of global G_h , beam G_{bh} and diffuse G_{dh} irradiance on a horizontal Mars surface at Viking Lander VL1.” (Image and caption credit: [16])

The angles θ and γ_S can be calculated with the equations introduced in the subsections 2.3.1 and 2.3.3. For these, however, the local latitude φ , the Sun's declination δ and the solar time t_S on Mars must be known. On Mars, the maximum values of δ are $-25, 19^\circ$ and $25, 19^\circ$ and the duration of one day is 24,6597h [23]. It is noted, that the equations (2.4) and (2.10) cannot be used to calculate δ and t_S .

In order to get the same energy yield with a PV generator on Mars as on Earth, this can be achieved in two ways. Based on the equation (2.20), and if it is assumed that the PV cell temperatures of the PV generator on Earth and Mars are equal ($\vartheta_{C,E} = \vartheta_{C,M}$), the radiation flux onto the energy-converting area $A_{PV,E}$ of the PV generator on Earth is equal to the radiation flux onto the energy-converting area $A_{PV,M}$ of the PV generator on Mars, when the following equation applies:

$$A_{PV,M} = A_{PV,E} \frac{E_{G,E}}{E_{G,M}}, \quad \text{for } \vartheta_{C,E} = \vartheta_{C,M}. \quad (2.90)$$

Therefore, a self-sufficient voice communication system with a PV generator area $A_{PV,E}$ and, for example, the requirement of an annual average irradiance $E_{G,E}$ to operate on Earth, would require an area $A_{PV,M}$ if there is an annual average irradiance $E_{G,M}$ at the place of use on Mars. The main disadvantage of this method is, that as the area of the PV generator increases, its mass and thus the payload of a rocket increases.

Diurnal temperatures between -89°C to -31°C on Mars theoretically lead to a higher output power of the PV generator. This can reduce the required area $A_{PV,E}$ [11], [23]. However, the influence of temperature must be examined more closely. Although the ambient temperature is lower, the heat dissipation of the PV generator to the surrounding atmosphere is worse than on Earth [73]. This shows that the equation (2.90) can only be used as a rough estimate.

The second approach is based on increasing the sensitivity S of the PV cells (see equation (2.41)) so that equation (2.40) can still deliver the same photocurrent current to charge the LiFePO₄ battery at a lower radiation flux Φ_G . In order to achieve this, the structure of the semiconductor the PV cells are made of needs to be adapted and improved. Research is still ongoing in this area [11].

With regard to longer lasting dust storms, energy can still be converted to supply the self-sufficient voice communication system due to the diffuse component of the total generator irradiance (compare to figure 2.25). This must be planned accordingly [11], [16]–[18]. It becomes more complicated when dust collects on the energy-converting area of the PV generator. Crew members would have to dust it off from time to time. This, however, shortens the effective mission time and increases the risk of an accident. Regarding the LiFePO₄ battery, this can further become a problem in between crewed missions. Even though these types of batteries have a low self-discharge, they can get damaged if they are not sufficiently charged for a longer period of time [63].

Finally, the second component that is heavily influenced by the Martian environment is the LiFePO₄ battery. This is mainly due to the aforementioned extreme diurnal ambient temperatures [23], [55]–[59]. Depending on how well the battery is insulated from the Martian environment in terms of temperature, additional energy from the battery must be used to continuously heat or cool it. Due to this, the nominal battery charge and – if necessary – the energy-converting area of the PV generator must be adjusted.

2.4 Voice communication system

In order to establish voice communication – and at a later stage data communication²⁶ – it was decided to use the VHF band.²⁷ It is preferred for mobile and handheld radio applications, as the range is relatively short and only extends over a few tens of kilometers. With regard to this, the possible interference with neighboring communication systems can be kept to a minimum [5]. Since the OeWF already uses handheld radios that operate in the VHF band, it was decided to incorporate them into the voice communication system due to their good condition.

In the past, VHF radios mainly used analog modulation methods for signal transmission. Nowadays, however, it is an increasing trend in this industry to use digital modulation methods. These have the decisive advantage that the signal quality – for example the audio quality – remains relatively constant up to a certain distance and then deteriorates drastically. In the case of radios that transmit an analog modulated signal, the quality of the signal constantly deteriorates with increasing distance [74]. So that good audio quality over longer distances can be guaranteed the decision was made to use a radio infrastructure based on digital modulation.

In combination with the aforementioned infrastructure, vertically polarized omnidirectional antennas were preferred because the field strength near the ground is stronger than that of horizontally polarized antennas. Moreover, these antennas are often more convenient to use and their directivity is the same for all cardinal directions – in relation to the installation site of a radio system or the current location of a handheld radio [5].

Communication with frequencies in the VHF range has the consequence that the radio waves only propagate – from the transmitter to the receiver – via a direct *line of sight* (LOS) and above the ground as ground waves. As will be shown later, the latter contribute more to the link budget. Ionospheric propagation does not occur in this band because the frequencies are too high [5].

The following subsections deal with the important equations and relationships required to model a voice communication system based on the facts just mentioned.

2.4.1 Load for the electrical energy distribution

In the section 2.1 the self-sufficient energy distribution system for the voice communication system was presented. The electrical load of the energy distribution system is a radio device – for example a repeater or a mobile radio – that operates independently of other energy sources with a certain duty cycle $a_T/a_R/a_{\text{Stby}}$ in (%). The duty cycle gives an indication of what percentage of the operating time the device is in transmission, receiving or standby mode. Since its current consumption is usually specified in the data sheet together with the associated operating mode, the load current I_L can be generalized as follows [75], [76]:

$$I_L(t) = \begin{cases} I_T(t), & \text{when the load transmits} \\ I_R(t), & \text{when the load receives} \\ I_{\text{Stby}}(t), & \text{when the load is in standby} \end{cases} \quad (2.91)$$

²⁶Data communication is not covered in this thesis.

²⁷The VHF band has a frequency range from 30MHz to 300MHz.

For a desired duty cycle, the current consumption of the device can then be modeled with a simple step function. It is assumed that the device installed on site – which is supplied by the self-sufficient energy distribution system – is not shut down outside of operating hours. During these hours it consumes I_{Stby} .

2.4.2 Free space signal budget

This subsection repeats the basics of the free space signal budget. It is assumed that there are no obstacles in the beam path between a transmitter and a receiver radio, and that their antennas are separated by the *distance* d in (m). The *available power* P_R in (W) at the receiving antenna with the *gain* G_R in (1) and the *receiving losses* L_R in (1) – which are caused by, for example, coaxial cables, connectors, adapters or lightning arresters in the antenna feed line – can then be calculated based on the *transmission power* P_T in (W), the gain of the transmission antenna G_T in (1), the *transmission losses* L_T in (1) – which are of the same nature as the receiving losses – and the *free space basic transmission loss* between isotropic antennas L_{ISO} in (1), while considering the *wavelength* λ_\sim in (m) of the transmitted electromagnetic wave, as shown in the equation (2.92).

$$P_R = P_T \underbrace{\left(\frac{\lambda_\sim}{4\pi d} \right)^2}_{L_{\text{ISO}}^{-1}} L_R L_T G_R G_T \quad (2.92)$$

When the equation (2.92) is expressed in decibels, it can be converted into a simple summation:

$$P_{R,\text{dBW}} = P_{T,\text{dBW}} + \underbrace{20\text{dB} \cdot \log_{10} \left(\frac{\lambda_\sim}{4\pi d} \right)}_{-L_{\text{ISO},\text{dB}}} - L_{R,\text{dB}} - L_{T,\text{dB}} + G_{R,\text{dBi}} + G_{T,\text{dBi}}. \quad (2.93)$$

The transmission and available power P_T and P_R use $P_0 = 1\text{W}$ as the reference power. A given power P in (W) can therefore be converted into decibels with:

$$P_{\text{dBW}} = 10\text{dBW} \cdot \log_{10} \left(\frac{P}{P_0} \right). \quad (2.94)$$

$G_{T,\text{dBi}}$ and $G_{R,\text{dBi}}$ in (dBi) are the antenna gains with respect to the isotropic radiator. The losses in the antenna feed lines are divided into two groups. First, the insertion losses caused by the signal attenuation due to the individual components in the antenna feed lines, and second, the losses caused by a slight mismatch of the impedances of these components. The latter causes reflections which result in a relative loss of P_T or P_R . Based on the *voltage standing wave ratio* (VSWR) in (1) of a component in the antenna feed line, the component's mismatch loss can be calculated as follows:

$$L_{M,\text{dB}} = -10\text{dB} \cdot \log_{10} \left(1 - \left(\frac{\text{VSWR} - 1}{\text{VSWR} + 1} \right)^2 \right). \quad (2.95)$$

With the number of occurring insertion and mismatch losses in the feed lines of the transmission and receiving antenna N_I and N_M in (1), $L_{R,\text{dB}}$ and $L_{T,\text{dB}}$ can now be

calculated with the equations (2.96) and (2.97):²⁸

$$L_{T,dB} = \sum_{i=1}^{N_I} L_{TIi,dB} + \sum_{j=1}^{N_M} L_{TMj,dB}, \quad (2.96)$$

$$L_{R,dB} = \sum_{i=1}^{N_I} L_{RIi,dB} + \sum_{j=1}^{N_M} L_{RMj,dB}. \quad (2.97)$$

Because digital modulation will be used, it is worth mentioning that the data sheet of a radio receiver contains information about the minimum required reception power $P_{min,dBW}$ in (dBW) in order not to exceed a certain *bit error rate* (BER). Whereby $P_{min,dBW}$ is usually not specified directly, but rather the sensitivity of the receiver in the form of a voltage U_{min} in (V). With the *system impedance* Z_{Sys} in (Ω), $P_{min,dBW}$ can subsequently be calculated from:

$$P_{min,dBW} = 10dBW \cdot \log_{10} \left(\frac{U_{min}^2}{Z_{Sys}} \right). \quad (2.98)$$

By subtracting $P_{min,dBW}$ from $P_{R,dBW}$, the fade margin can be obtained. If this margin is negative, the system performance insufficient because the received signal is too weak to be processed. This leads to a higher BER or complete loss of signal. When designing a mission critical voice communication system, this margin must therefore be positive and sufficiently large. Its minimum value should be around 20dB to 30dB [2], [5]–[8], [47], [48].

It is moreover noted, that:

$$L_{dB} = 10dB \cdot \log_{10} \left(\frac{P_R}{P_T} \right) \quad (2.99)$$

is the *total path attenuation* in (dB) and:

$$EIRP_{dBW} = P_{T,dBW} + G_{T,dBi} \quad (2.100)$$

is the *effective isotropic radiated power* in (dBW). The quantities P_T , U_{min} , $G_{R,dBi}$ and $G_{T,dBi}$, as well as the insertion losses and the VSWRs can usually be taken from the data sheets of the components and radio devices used in the voice communication system.²⁹ The wavelength follows from the expression:

$$\lambda_{\sim} = \frac{c_0}{f_{\sim}}, \quad (2.101)$$

where $c_0 = 299792458\text{ms}^{-1}$ is the *speed of light* and f_{\sim} in (Hz) is the *frequency* of the transmitted electromagnetic wave [2], [5]–[7], [47], [48].

²⁸The equations (2.96) and (2.97) are the same. This is due to the reciprocity of radio systems. In practice, it makes sense to first calculate the losses in the antenna feed lines of the individual radio devices and then name them $L_{T,dB}$ or $L_{R,dB}$ in the further calculations.

²⁹The information in the data sheets applies to $\vartheta_{A,K} = 290K$ ($\vartheta_A = 16, 85^\circ\text{C}$) if no other reference temperature is given.

2.4.3 Plane earth signal budget

Building on the free space signal budget, the plane earth signal budget now takes into account the Earth's surface as an infinitely extended smooth plane, with the antennas being mounted at heights h_T and h_R in (m) above this plane. As a result of this arrangement, the transmitted electromagnetic waves are now reflected in such a way that they can increase the available power P_R at the receiver. Figure 2.26 is used for illustration. An electromagnetic wave reflected from the ground covers the path d_2 in (m), whereas a wave that is transmitted directly from the transmission to the receiving antenna covers the path d_1 in (m). ψ in ($^\circ$) is the angle of incidence of the electromagnetic waves at the point of reflection and $\underline{\rho}$ is the complex reflection coefficient for vertical polarization in (1). The latter can be obtained from the

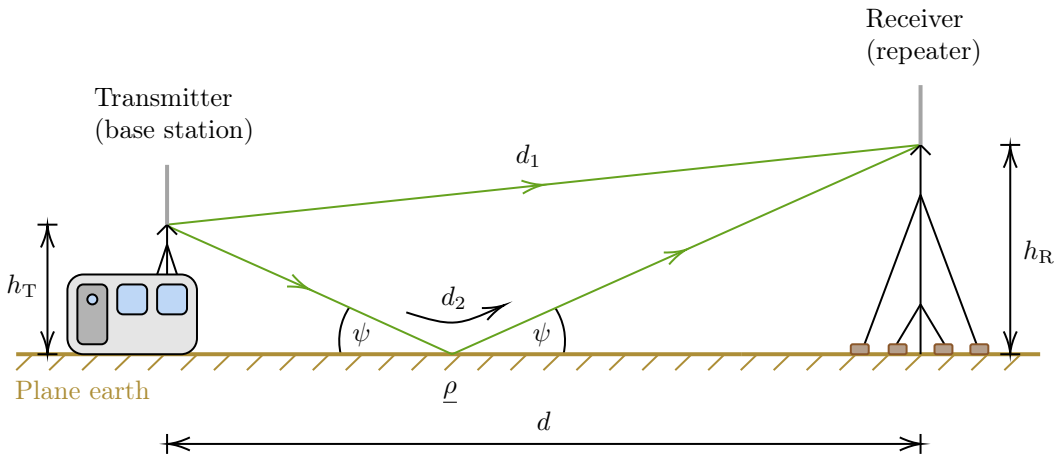


Figure 2.26: Illustration of the plane earth signal budget. (Recreated from: [2], [5], [6])

equation (2.102), where ε_r in (1) is the relative dielectric constant of the Earth, ε_0 in ($\text{AsV}^{-1}\text{m}^{-1}$) is the dielectric constant of free space, σ in (Ω^{-1}) is the conductivity of the Earth and $\omega = 2\pi f_\sim$ is the angular frequency in (s^{-1}).

$$\underline{\rho} = \frac{(\varepsilon_r - jx) \sin \psi - \sqrt{(\varepsilon_r - jx) - \cos^2 \psi}}{(\varepsilon_r - jx) \sin \psi + \sqrt{(\varepsilon_r - jx) - \cos^2 \psi}}, \quad \text{with } x = \frac{\sigma}{\omega \varepsilon_0} \quad (2.102)$$

Based on $\underline{\rho}$, the field strength at the receiving antenna changes with the complex factor:

$$F = 1 + \underline{\rho} \exp(-j\Theta). \quad (2.103)$$

The phase difference Θ in (rad) – which occurs due to the reflection of the electromagnetic wave – can be derived from the figure 2.26 as shown below:

$$\Theta = \frac{4\pi h_T h_R}{\lambda_\sim d}. \quad (2.104)$$

If the angle of incidence ψ is small, which is the case for $d \gg h_T, h_R$, a perfect reflection of the electromagnetic wave can be assumed, hence $\underline{\rho} = \exp(j\pi) = -1$.³⁰ This is because the E-field for the transversal magnetic (TM) mode is perpendicular to the plane when ψ is small [7]. As a result, the squared absolute value of the

³⁰It can be seen that the phase difference Θ is small for $d \gg h_T, h_R$.

complex factor, which now represents the power increase at the receiving antenna compared to free space propagation, can be simplified to:

$$|\underline{F}|^2 = 4 \left| \sin^2 \left(\frac{\Theta}{2} \right) \right| = 4 \sin^2 \left(\frac{2\pi h_T h_T}{\lambda_\sim d} \right), \quad \text{for } \underline{\rho} = -1. \quad (2.105)$$

By multiplying the result from the equation (2.105) with the right side of the equation (2.92), the available power at the receiving antenna for plane earth propagation results in:

$$\begin{aligned} P_R &= P_T \left(\frac{\lambda_\sim}{4\pi d} \right)^2 L_R L_T G_R G_T |\underline{F}|^2 \\ &= 4P_T \left(\frac{\lambda_\sim}{4\pi d} \right)^2 L_R L_T G_R G_T \sin^2 \left(\frac{2\pi h_T h_T}{\lambda_\sim d} \right). \end{aligned} \quad (2.106)$$

Finally, since $d \gg h_T, h_R$ applies, the sine in the equation (2.106) can be approximated with $\sin x \approx x$, from which the *plane earth propagation equation* is derived:

$$P_R = P_T \left(\frac{h_T h_R}{d^2} \right)^2 L_R L_T G_R G_T, \quad \text{for } d \gg h_T, h_R. \quad (2.107)$$

Expressed in decibels this equation can be written as:

$$P_{R,\text{dBW}} = P_{T,\text{dBW}} + \underbrace{20\text{dB} \cdot \log_{10} \left(\frac{h_T h_R}{d^2} \right)}_{-\text{PEPL}_{\text{dB}}} - L_{R,\text{dB}} - L_{T,\text{dB}} + G_{R,\text{dB}} + G_{T,\text{dB}},$$

for $d \gg h_T, h_R.$

(2.108)

PEPL_{dB} is the *plane earth path loss* in (dB) [2], [5], [6].

2.4.4 Martian application

In the previous subsections, some important factors were neglected in order to provide a rough performance estimation of the voice communication system on Earth. For an application on Mars these factors should be considered when designing such a system.

First, the influence of the internal noise of the components – which is due to their thermal noise – as well as the influence of the electromagnetic noise collected by the receiving antenna, must be considered. Antennas in the 30MHz to 1GHz range primarily pick up galactic noise which is caused by the radiation produced by electrons moving through the galactic magnetic field of the Milky Way. Due to the shape of the Milky Way and the location of the Earth within it, this type of noise is anisotropic in nature. It increases when the antenna is pointed directly at the center of the Milky Way. For a more detailed examination of the link budget of a voice communication system on Mars, the galactic noise affecting the system would have to be examined more closely. Because of the low temperatures on Mars, the thermal noise of the components and radio devices will probably be lower. However, due to the thinner atmosphere, the heat generated by these cannot be dissipated, which in turn increases the temperature of the system and thus its thermal noise. This problem must be solved with suitable cooling. For completeness it must be

mentioned that interference caused by other missions or electrical devices on the surface of Mars or in its orbit should not be neglected when planning a voice communication system. Such interferences can be identified as man-made-noise [2], [6], [73].

Second, a topological map of the mission location can be created, on the basis of which a multipath propagation simulation is carried out so that the radio infrastructure can be optimally placed. In contrast to the voice communication system of the OeWF, which is constantly being set up at new mission locations, it is assumed that the radio infrastructure on Mars will only be set up once and then expanded with further missions. Thus, such an elaborate simulation of the multipath propagation can be useful. It is desirable to set up a functioning voice communication network with as little infrastructure as possible in order to save weight and minimize assembly time [19].

Third, the propagation of VHF waves in relation to the Martian atmosphere must be investigated. The authors of [19] have found out that Mars has almost no intrinsic magnetic field, which means that the use of the ionosphere for wave propagation is very dependent on the time of day and the season. During the day, the ionosphere can be used as a reflector for global communication, whereas this may not be possible at night. The authors also assumed that the attenuation of a VHF signal due to the ionosphere is approximately 0,5dB. The effects of storms in the ionosphere have not yet been researched enough to make any statements about them.

Since the troposphere of Mars is very thin, it is believed that it has little effect on the propagation of electromagnetic waves [19].

With regard to dust storms, the authors of [19] further state that due to the large wavelength of VHF signals, compared to the size of Martian dust particles – with adiameter of 0,1mm – the signal attenuation is rather small. However, this still needs to be researched, as dust density also plays a major role.

Fourth, the system must have sufficient redundancy so that a total failure is very unlikely. Loss of communication can potentially be dangerous for a crew during an ongoing mission.

3 Results

With the help of the relationships mentioned in the previous chapter, the designed voice communication system is now briefly explained. A performance estimation was made based on this design and the results are presented in the following sections. For a more fluid readability, the system design is discussed first, followed by the link budget estimation and finally the results of the energy distribution system are presented.

3.1 System design

In order to meet the requirements mentioned in the introduction, a topology of the voice communication system as shown in the figure 3.1 was chosen. Voice communication takes place via the frequency $f_{\sim} = 158,950\text{MHz}$ and the system consists of a *base station* (BSt) – which the OeWF refers to as *operations* (OPS) – an *on-site support* (OSS) crew with handheld radios, a self-sufficient voice communication repeater – which from now on will simply be referred to as *repeater* (REP) – *analog astronauts* (AAs) using the *Serenity* (SER) spacesuit simulator and the safety officers for the AAs. The latter also carry handheld radios. The green arrows indicate

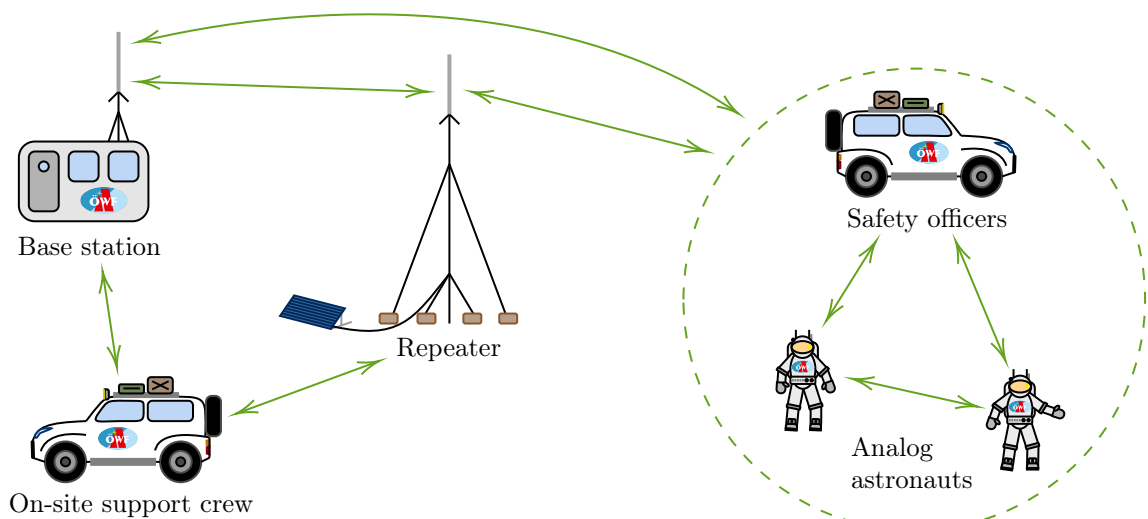


Figure 3.1: Proposed topology for the designed voice communication system.

that voice communication can take place in both directions. Furthermore, all participants within the dashed green circle can either communicate directly with the base station, or via the repeater. If the communication takes place via the repeater,

the distance between the base station and the dashed circle can be increased. The same applies for the on-site support crew. During an ongoing mission the on-site support crew does not communicate with the participants within the dashed circle, but only with the base station.

In essence, the proposed topology is a mesh topology with digital voting. The latter means that a receiver in the system only accepts the strongest source of a particular transmitted signal and ignores the others. This has the major advantage that both the participants within the dashed circle and the on-site support crew can move freely within the range of the base station and the repeater without having to change the channels on their radios [5], [74].

In practice several channels for communication are used so that the traffic over the repeater is kept to a minimum. Radio traffic must therefore be kept low, as the repeater is operated in the so-called *extended range direct mode* which is its simplex mode. In this mode only one participant of the voice communication system can communicate via the repeater at a time. This approach was chosen because the extended range direct mode requires only one frequency and therefore only one antenna [74]. However, this is not dealt with in more detail in this thesis, as it does not affect the link budget.¹

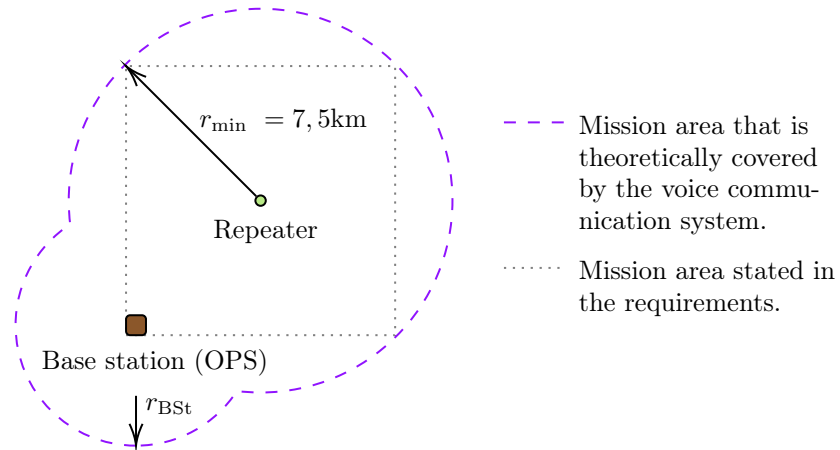


Figure 3.2: Top view of the mission area covered by the voice communication system.

Figure 3.2 shows the top view of the mission area that is theoretically covered by the voice communication system [4]. The border of the mission area covered is illustrated with the dashed purple line. In it, the brown rounded square represents the base station, the green dot represents the repeater and the gray dotted square represents the mission area specified by the system requirements. According to these requirements the minimum radius is $r_{\min} = 7,5\text{km}$, as a total mission area of approximately 10km by 10km has to be covered. Furthermore, the system was designed in such a way that the requirements are met for the least powerful radio device.

Since the base station, like the repeater, uses an omnidirectional antenna, the participants of the voice communication system also have reception in an area with a radius r_{BSt} in (m) around it. By transforming the equation (2.108) and assuming that the fade margin of the least powerful radio device stays the same for the entire

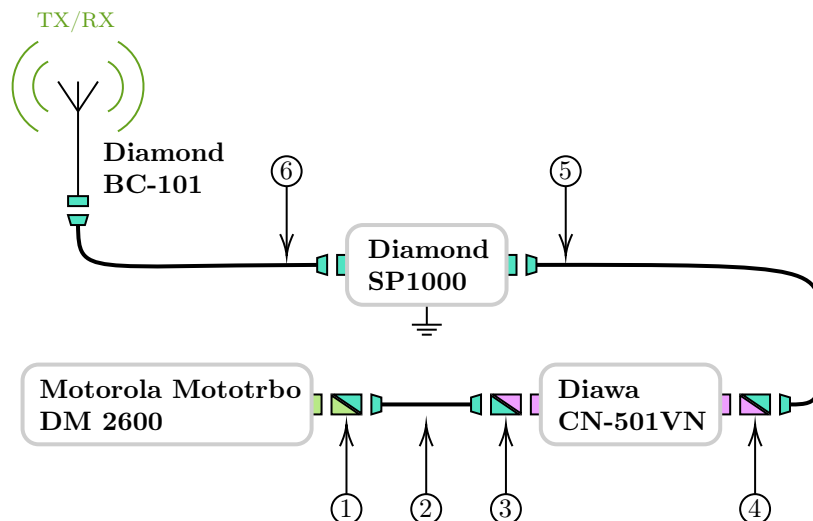
¹Further information can be found in the user manual once it has been completed.

coverage area, r_{BSI} can be calculated.² Although this extends the mission area, it must be taken into account that it may interfere with a neighboring radio system.

In the following subsections each part of the voice communication system will be introduced.

3.1.1 Base station radio infrastructure

The task of the base station crew is to monitor and coordinate both an ongoing mission and the on-site support crew. It is thus the central link of the voice communication system. The base station radio infrastructure is supplied by electrical energy from the local power grid and it consists of a Motorola Mototrbo DM 2600 mobile radio, a Diawa CN-501VN cross needle VSWR & power meter to monitor the VSWR of the antenna feed line and detect possible errors, a Diamond SP1000 lightning arrester to protect the base station crew, the DM 2600 and the CN-501VN from the consequences of a lightning strike³ and a Diamond BC-101 VHF fixed station antenna. Besides that, several adapters and coaxial cables with different lengths l in (m) are used to connect these devices and components with each other. Figure



- ① **Adapter:** BNC plug to PL socket
- ② **Coaxial cable:** M&P Ultraflex 7 with two PL plugs, $l = 0,3\text{m}$
- ③ **Adapter:** PL socket to N plug
- ④ **Adapter:** N plug to PL socket
- ⑤ **Coaxial cable:** M&P Ultraflex 7 with two PL plugs, $l = 2\text{m}$
- ⑥ **Coaxial cable:** M&P Ultraflex 7 with two PL plugs, $l = 7\text{m}$

Figure 3.3: Schematic structure of the base station radio infrastructure.

3.3 provides an illustration. There are gaps between the devices and components to make the schematic structure easier to read.⁴ Green connectors represent a BNC

²In the equation (2.108), r_{BSI} corresponds to the distance d .

³It is not recommended to use the voice communication system in situations where lightning strikes may occur.

⁴In practice these are connected.

plug or socket, turquoise connectors represent a PL plug or socket and pink connectors represent a N plug or socket. For more information on whether it is a socket or a plug, see figure 3.3 and tables 3.1 through 3.5. Adapters – such as ① and ③ – are characterized by a rectangle with a diagonal drawn in. The colors in the resulting right-angled triangles indicate which connectors an adapter has. Coaxial cables are drawn with a thicker line and trapezoids as connectors – for example ②, ⑤ and ⑥. Because the coaxial cables were delivered without connectors, they were installed afterwards. The connectors of the DM 2600, Diawa CN-501VN, Diamond SP1000 and Diamond BC-101 are marked by a small rectangle which is in direct contact with the associated device or component. These have factory-installed connectors which their data sheets already take into account.

From the data sheet of the DM 2600, from which an excerpt is provided in table 3.1, it can be seen that its maximum transmission power is 25W and its sensitivity – in the worst case – is $0,25\mu\text{V}$. Its maximum transmission and minimum required

Motorola Mototrbo DM 2600 (VHF digital) specifications	
Frequency	136MHz to 174MHz
System impedance	50Ω
Dimensions (H × W × D)	$44 \times 169 \times 134\text{mm}$
Mass	1,3kg
Power supply	13,2VDC (nominal) (10,8 to 15,6VDC)
Current standby	0,81A (max.)
Current RX	2A (max.)
Current TX	11A (max.)
Operating temperature	-30°C to 60°C
Storage temperature	-40°C to 85°C
RX sensitivity 5% BER:	$0,25\mu\text{V}$ ($0,19\mu\text{V}$ typical)
TX power output	1W to 25W
Connector	BNC socket

Table 3.1: Excerpt from the data sheet of the Motorola Mototrbo DM 2600 mobile radio. [75]

reception power therefore follow to:

$$P_{\text{T,dBW}} = 10\text{dBW} \cdot \log_{10} \left(\frac{25\text{W}}{1\text{W}} \right) = 13,979\text{dBW}, \quad (3.1)$$

$$P_{\text{min,dBW}} = 10\text{dBW} \cdot \log_{10} \left(\frac{(0,25 \cdot 10^{-6}\text{V})^2}{50\Omega} \right) = -149,031\text{dBW}. \quad (3.2)$$

It is assumed that the CN-501VN will not cause any loss or gain in the antenna feed line as its data sheet does not contain any specifications on this matter. An excerpt of said data sheet can be seen in the table 3.2.

The SP1000 has an insertion loss of less than 0,2dB and a VSWR of less than 1,2 as shown in the table 3.3. If now the worst case is assumed – which means that the insertion loss is exactly 0,2dB and the VSWR is exactly 1,2 – then the total loss caused by this component is the sum of the insertion and the mismatch loss:

$$L_{\text{arr,dB}} = 0,2\text{dB} - 10\text{dB} \cdot \log_{10} \left(1 - \left(\frac{1,2 - 1}{1,2 + 1} \right)^2 \right) = 0,236\text{dB}. \quad (3.3)$$

As can be seen in the table 3.4, the BC-101 has a gain of $G_{\text{ant,dBi}} = 3,5\text{dBi}$ and a VSWR of less than 1,5. With $\text{VSWR} = 1,5$, the mismatch loss in the worst case

Daiwa CN-501VN specifications	
Frequency	140MHz to 525MHz
Input/Output impedance	50Ω
Dimensions (H × W × D)	80 × 155 × 100mm
Weight	0, 67kg
Power range	20W/200W (forward)
Power rating	200W (140MHz to 525MHz)
Tolerance	±10% at full scale
VSWR measurement range	1 to ∞
VSWR detection sensitivity	200W (min.)
Connector	2 × N socket

Table 3.2: Excerpt from the data sheet of the Daiwa CN-501VN cross needle VSWR & power meter.[77]

Diamond SP1000 specification	
Frequency range	0 to 1000MHz
Impedance	50Ω
VSWR	< 1, 2
Insertion loss	< 0, 2dB
Max. power rating	400W
Impulse wave discharge voltage	1000V
Impulse wave discharge current	6000A
Impulse wave retention voltage	350VDC ± 20%
Insulating resistance (100VDC)	> 10000MΩ
Connector	2 × PL socket

Table 3.3: Excerpt from the data sheet of the Diamond SP1000 lightning arrester. [78]

Diamond BC-101 specifications	
Type	5/8 wave ground plane
Frequency	144MHz to 174MHz
Impedance	50Ω
Gain	3, 5dBi
Power rating	200W (max.)
VSWR	< 1, 5
Weight	0, 86kg
Connector	PL plug

Table 3.4: Excerpt from the data sheet of the Diamond BC-101 VHF fixed station antenna.[79]

can be calculated as shown in the equation (3.4).

$$L_{\text{ant,dB}} = -10 \text{dB} \cdot \log_{10} \left(1 - \left(\frac{1,5 - 1}{1,5 + 1} \right)^2 \right) = 0, 177 \text{dB} \quad (3.4)$$

Regarding this antenna, it should also be mentioned that a mast will be made available at the mission site. Therefore, the height of the mast can vary from mission to mission. An antenna, which is set up on a 1m high tripod on a freight container in accordance with ISO 668, has approximately a height of $h_{\text{BSt}} = 3, 6 \text{m}$ above the ground. This height is used for the link budget estimation.

All coaxial cables used for the voice communication system are Messi & Paoloni Ultraflex 7 coaxial cables. An excerpt of the data sheet of this coaxial cable can be found in the table 3.5 and the attenuation as a function of the frequency – interpolated with a **MATLAB** program – according to its data sheet, in the figure

Messi & Paoloni Ultraflex 7 specifications	
Frequency	1, 8MHz to 8000MHz
Impedance	$50 \pm 3\Omega$ (at 200MHz)
Operating temperature	-40°C to 60°C
Inner conductor resistance	$7, 3\Omega\text{km}^{-1}$
Outer conductor resistance	$9, 8\Omega\text{km}^{-1}$
Capacitance	$75 \pm 3\text{pFm}^{-1}$
Power rating	8000W (peak)
Net. weight	6, 9kg/100m
Connector	none

Table 3.5: Excerpt from the data sheet of the Messi & Poloni Ultraflex 7 coaxial cable. [80]

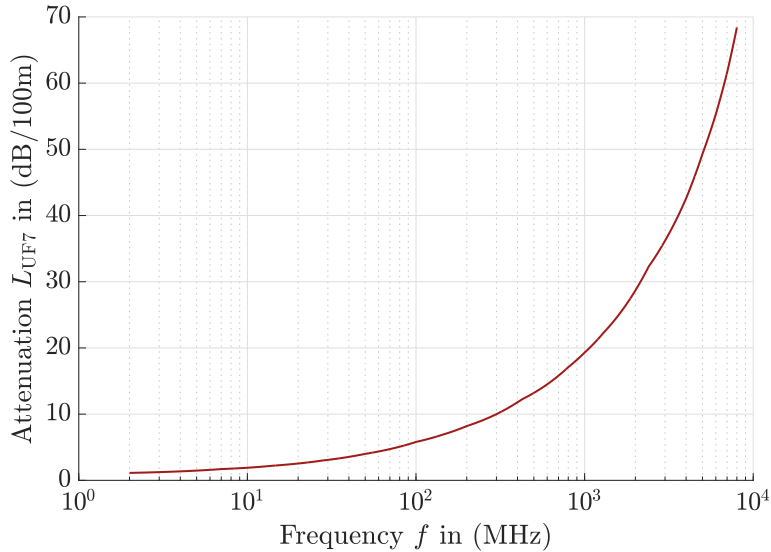


Figure 3.4: Attenuation of the Messi & Paoloni Ultraflex 7 coaxial cable for 20°C. For the frequency $f_{\sim} = 158,950\text{MHz}$, the attenuation is around 7,2471dB/100m. (Recreated from: [80])

3.4. Based on this, an attenuation of 7,2471dB/100m was determined for the frequency $f_{\sim} = 158,950\text{MHz}$. The cable lengths of the individual coaxial cables in the systems can be taken from the figure 3.3. This results in an insertion loss – without connectors – of:

$$L_{\text{coax,dB}} = \frac{7,2471 \cdot 9,3}{100} \text{dB} = 0,674 \text{dB}. \quad (3.5)$$

It is noted, that $L_{\text{coax,dB}}$ increases as the cable length increases. It can become significantly greater if the antenna is mounted at a location further away from the base station.

Regarding the attenuation of the numbered adapters and connectors, which also includes the connectors of the coaxial cables in the figure 3.3, it is assumed that each of these has an attenuation of 0,1dB [8]. With $N_I = 9$, the total insertion loss caused by the connectors and adapters follows to:

$$L_{\text{conn/adapt,dB}} = 0,9 \text{dB}. \quad (3.6)$$

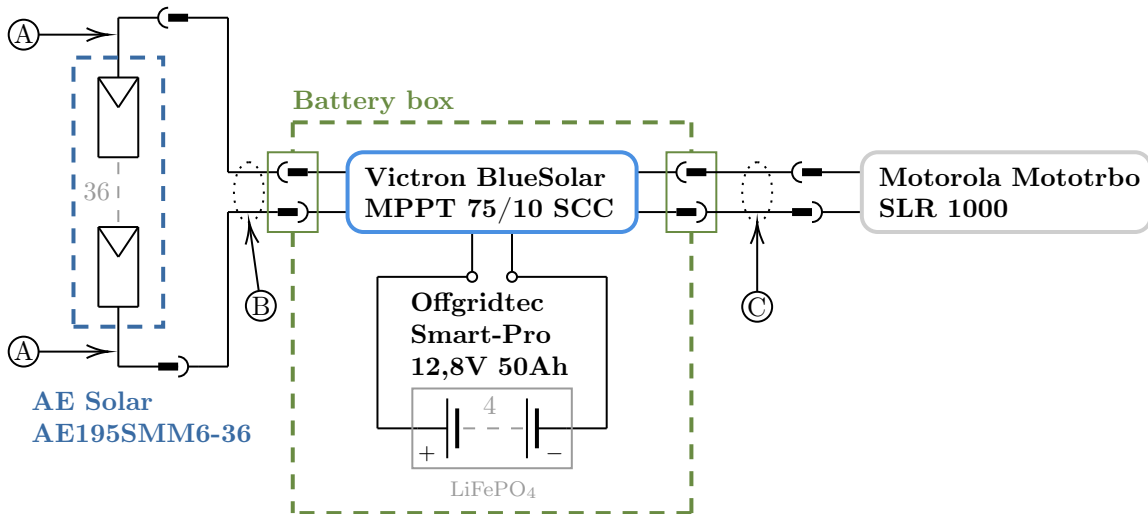
An assumption was made because no data sheets for the adapters and connectors were found.

From the above, the total loss of the antenna feed line now results in:

$$L_{\text{BSt,dB}} = L_{\text{arr,dB}} + L_{\text{ant,dB}} + L_{\text{coax,dB}} + L_{\text{conn/adapt,dB}} = 1,987 \text{dB}. \quad (3.7)$$

3.1.2 Repeater radio infrastructure

The main task of the repeater is to receive weak signals and to re-transmit them with increased transmission power. Its radio infrastructure is supplied by electrical energy from the self-sufficient energy distribution system, for which the schematic structure is shown in the figure 3.5. As it can be seen, an AE Solar AE195SMM6-36 PV generator with pre-mounted cables (A), a Victron BlueSolar MPPT 75/10 SCC and an Offgridtec Smart-Pro 12,8V 50Ah LiFePO₄ battery are used. In addition, the cables (B) and (C), which are designed for harsh environments, are used to connect these devices. The SCC and the LiFePO₄ battery are contained in an IP67 certified



- (A) PV generator cable: 1 × (Cu, $A = 4\text{mm}^2$, $l = 0,9\text{m}$)
- (B) H07RN-F cable: 2 × (Cu, $A = 4\text{mm}^2$, $l = 0,5\text{m}$)
- (C) H07RN-F cable: 2 × (Cu, $A = 2,5\text{mm}^2$, $l = 11\text{m}$)

Figure 3.5: Schematic structure of the self-sufficient energy distribution system of the repeater radio infrastructure.

battery box to protect them from the environment. This IP rating also applies to the connectors in the small green rectangles.

In the figure 3.5, only the part necessary for the simulation of the self-sufficient energy distribution system can be seen. In practice, fuses, switches, lightning protection and other important components are also installed. Due to the short length of the cable that connects the LiFePO₄ battery with the SCC, it was neglected. The simulation results of the self-sufficient energy distribution system of the repeater radio infrastructure can be found in the section 3.3.

Continuing from the SLR 1000, the repeater radio infrastructure further consists of a Diamond SP1000 lightning arrester to protect the SLR 1000 and the self-sufficient energy distribution system from the consequences of a lightning strike and a Diamond BC-101 VHF fixed station antenna. As shown in the figure 3.6, additional adapters, connectors and a coaxial cable are required. The adapter (1) represents a 90° angle.

Using the specifications of the SLR 1000 listed in the table 3.6, the maximum transmission power is calculated in the equation (3.8). The minimum required reception power for the worst case can be taken from the equation (3.2).

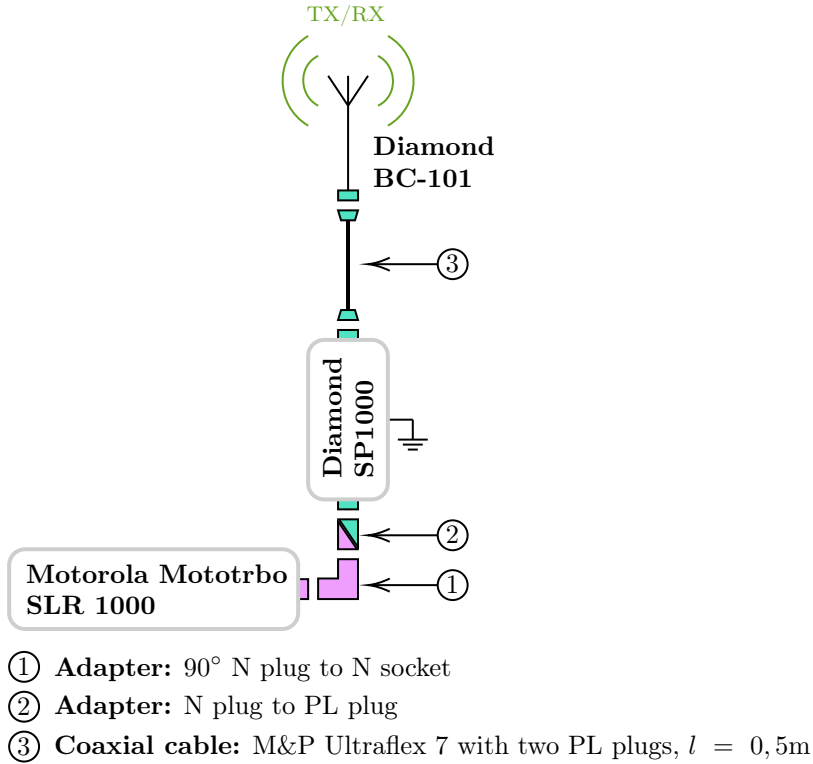


Figure 3.6: Schematic structure of repeater radio infrastructure.

Motorola Mototrbo SLR 1000 (VHF digital) specifications	
Frequency	136MHz to 174MHz
System impedance	50Ω
Dimensions (H × W × D)	279 × 229 × 102mm
Mass	4, 54kg
Power supply	12VDC (11, 0 to 15, 5VDC)
Current RX and standby	0, 7A (0, 63A typical)
Current TX	3A (max.)
Operating temperature	-30°C to 60°C
RX sensitivity 5% BER:	0, 25μV (0, 18μV typical)
TX power output	1W to 10W
Connector	N socket
IP rating	65

Table 3.6: Excerpt from the data sheet of the Motorola Mototrbo SLR 1000 repeater. [76]

$$P_{T,\text{dBW}} = 10\text{dBW} \cdot \log_{10} \left(\frac{10\text{W}}{1\text{W}} \right) = 10\text{dBW}, \quad (3.8)$$

Since the repeater uses the same lightning arrester and the same antenna as the base station, the resulting losses can be taken directly from the equations (3.3) and (3.4). The antenna of the repeater is always mounted at a height of $h_{\text{REP}} = 8\text{m}$ above the ground, as a mast is included in the system design.

As can be seen in the figure 3.6, the length of the coaxial cable is 0, 5m, resulting in an insertion loss of:

$$L_{\text{coax,dB}} = \frac{7, 2471 \cdot 0, 5}{100} \text{dB} = 0, 036\text{dB}. \quad (3.9)$$

With the number of adapters and connectors $N_I = 4$, their insertion loss follows

to:

$$L_{\text{conn/adapt,dB}} = 0,4 \text{dB}. \quad (3.10)$$

Finally, the total loss of the antenna feed line can be calculated with:

$$L_{\text{REP,dB}} = L_{\text{arr,dB}} + L_{\text{ant,dB}} + L_{\text{coax,dB}} + L_{\text{conn/adapt,dB}} = 0,849 \text{dB}. \quad (3.11)$$

3.1.3 Serenity radio system

As mentioned earlier, Serenity is the spacesuit simulator that the AAs use to conduct analog Mars missions. Its radio system consists of a Motorola Mototrbo SL 2600 handheld radio with a Motorola PMAD4156A antenna, a *push-to-talk* (PTT) button and a Jabra Storm Bluetooth headset. The antenna is attached directly to the handheld radio and the entire system is built into the spacesuit simulator with the upper part of the antenna sticking out. Since the SL 2600 radio supports Bluetooth 4.0, it was decided that communication with the headset should take place via Bluetooth. This has two advantages. Firstly, the AA can put on the headset before donning and thus simply step into the spacesuit simulator, and secondly, the amount of cabling is reduced. The PTT button is wired to the outside of the spacesuit so that the AA can press it to communicate. A schematic structure of this system is illustrated in the figure 3.7.

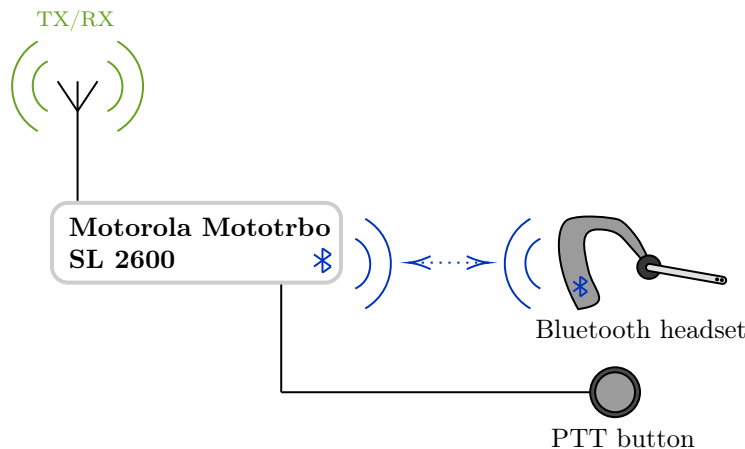


Figure 3.7: Schematic structure of the Serenity radio system.

Electrical energy is provided to the SL 2600 via its 2,3Ah lithium-ion battery (Motorola PMNN4468B) which is charged with the electrical energy from the local power grid between missions. At a later point in time, the radio system can be upgraded in such a way, that the SL 2600 can be directly charged from the spacesuit simulator. Similar to the SL 2600, the Bluetooth headset is also supplied with electrical energy from its battery, but can only be charged via the local power grid.

The maximum transmission power of the SL 2600, as shown in the equation (3.12), is calculated based on its specifications in the table 3.7.

$$P_{\text{T,dBW}} = 10 \text{dBW} \cdot \log_{10} \left(\frac{3 \text{W}}{1 \text{W}} \right) = 4,771 \text{dBW}, \quad (3.12)$$

As with the SLR 1000, the minimum required reception power for the worst case can be taken from the equation (3.2). At this point, the assumption is made that

Motorola Mototrbo SL 2600 (VHF digital) specifications	
Frequency	136MHz to 174MHz
Dimensions (H × W × D)	125, 7 × 55, 0 × 22, 7mm
Mass (incl. std. battery)	190g
Power supply	3, 7VDC (nominal)
Average battery life at 5/5/90 duty cycle	13, 5h
Operating temperature	-30°C to 60°C
Storage temperature	-40°C to 85°C
RX sensitivity 5% BER:	0, 25µV (0, 19µV typical)
TX power output	0, 5W to 3W
Bluetooth version	4, 0
IP rating	54

Table 3.7: Excerpt from the data sheet of the Motorola Mototrbo SL 2600 handheld radio. [81]

the antenna impedance is 50Ω , as no further specifications could be found. It was furthermore assumed that there are no losses in the antenna feed line and that the antenna has a gain of 0dBi.

In cooperation with the Serenity *structures* (STRUC) team, a position for the SL 2600 in the HUT of the spacesuit simulator was found, so that its antenna is upright at a height of 1,65m above the ground for a standard male AA, or at a height of 1,55m above the ground for a standard female AA [82]. Regarding the link budget estimation $h_{SER} = 1,55\text{m}$ is used. In its installed position the device can be recharged and, if necessary, removed for maintenance purposes. This fulfills the requirement that the Serenity radio system must fit into the HUT.

Taking into account the requirements for the operating temperature of the radio system, the data sheets of the SL 2600 (see table 3.7) and the PTT button, including the wires and connectors involved, show that these are met. Due to the large push area of the PTT button, it was adopted from the Aouda spacesuit simulator, which is the predecessor of Serenity. No specifications were found for the Bluetooth headset and the audio jack that connects the PTT button to the SL 2600. The prototype still needs to be tested in this regard. However, if these do not meet the requirements, a suitable audio jack can be requested directly from Motorola Solutions Inc. and the Motorola EP900w Bluetooth headset can be procured [83], [84].

The most important factor that needed to be considered when developing the radio system was its mass. As stated in the requirements, the combined mass of the W-LAN and VHF based communication systems must not exceed 1000g. At the time the Serenity (VHF) radio system was developed, the W-LAN based communication system had a mass of 605, 33g. The total mass of the (VHF) radio system is 248g. This results in a combined mass of 853, 33g. 9g of this is the mass of the Jabra Storm Bluetooth headset. Should it be replaced by the Motorola EP900w Bluetooth headset, the (VHF) radio system would then have a mass of 261g, which results in a combined mass of 866, 33g. The measurements were conducted with a digital kitchen scale from WMF (Model No.: 06.0873.6040). In the case that the audio jack needs to be changed, its mass is likely to remain the same. Since the W-LAN based communication system is not finished, it cannot be said at this point whether the mass requirement has been met.

3.1.4 Safety officer radio

The safety officers do not interact directly with the AAs during an ongoing mission, but intervene in certain events. During these events it is crucial that voice communication is established between these two groups. For this purpose, the safety officers use a Motorola Mototrbo SL 2600 handheld radio with the same antenna and lithium-ion battery as that of the AAs. The battery of the SL 2600 is charged by the local power grid between missions.

The maximum transmission power is the same as in the equation (3.12) and the minimum required reception power for the worst case is the same as in the equation (3.2).

Regarding the antenna, the same assumptions are made as for the Serenity radio system. However, its height above the ground was determined based on the anthropometric dimensional data for an american female and male, shown in the figures 3.8a and 3.8b. When it is assumed that the SL 2600 is operated at shoul-

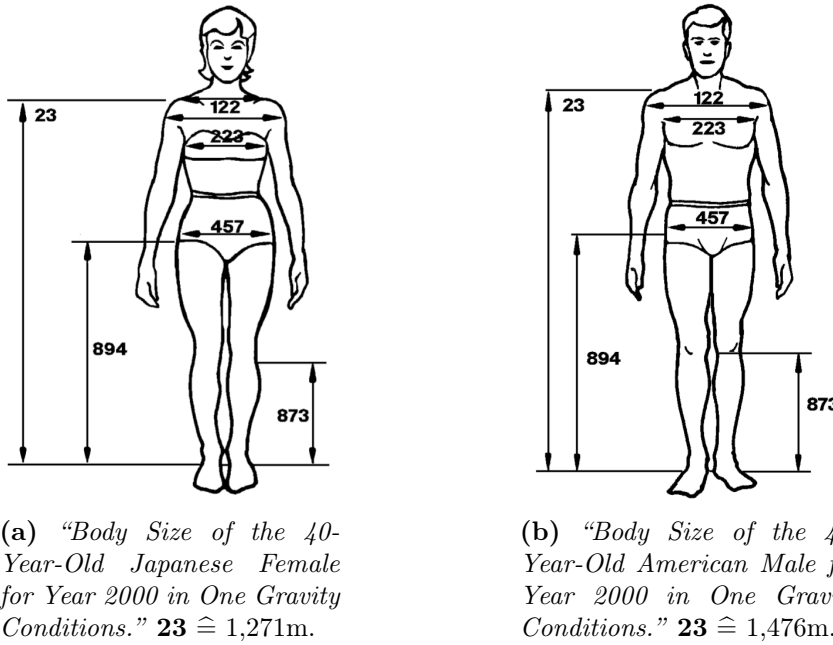


Figure 3.8: Anthropometric dimensional data for the american female and male. (Image and caption credit: [82], [85])

der height, then its antenna is 1,271m above the ground for a female and 1,476m above the ground for a male safety officer [82], [85]. For the link budget estimation $h_{SFTY} = 1,271\text{m}$ is used.

3.1.5 On-site support crew radio

The on-site support crew, which carries out general tasks in the mission area, uses the DP 3601 handheld radios. These are supplied with electrical energy from their 2,15Ah lithium-ion batteries (Motorola PMNN4103A) which are charged via the local power grid when required.

According to the same principle as in the previous subsections, the maximum transmission power of the DP 3601 can be calculated using the equation (3.13), with its specifications being listed in the table 3.8.

Motorola Mototrbo DP 3601 (VHF digital) specifications	
Frequency	136MHz to 174MHz
Dimensions (H × W × D)	131, 5 × 63, 5 × 35, 2mm
Mass (incl. 2200mAh li-ion battery)	361g
Power supply	7, 5VDC (nominal)
Average battery life at 5/5/90 duty cycle	19, 0h
Operating temperature	-30°C to 60°C
Storage temperature	-40°C to 85°C
RX sensitivity 5% BER:	0, 30µV
TX power output	1W to 5W
IP rating	57

Table 3.8: Excerpt from the data sheet of the Motorola Mototrbo DP 3601 handheld radio. [86]

$$P_{T,\text{dBW}} = 10\text{dBW} \cdot \log_{10} \left(\frac{5\text{W}}{1\text{W}} \right) = 6, 99\text{dBW}, \quad (3.13)$$

Since the DP 3601 is an older handheld radio, its sensitivity differs from that of the other Motorola Mototrbo radio devices mentioned earlier. By assuming that the antenna impedance is 50Ω – due to the same reasons as for the SL 2600 – the minimum required reception power follows to:

$$P_{\min,\text{dBW}} = 10\text{dBW} \cdot \log_{10} \left(\frac{(0, 30 \cdot 10^{-6}\text{V})^2}{50\Omega} \right) = -147, 447\text{dBW}. \quad (3.14)$$

The antenna of the DP 3601 is directly attached to the radio and it is assumed, that no losses in the antenna feed line occur. Furthermore, its gain is assumed to be 0dBi and, as in the previous subsection, its hight above the ground is assumed to be $h_{\text{OSS}} = 1, 271\text{m}$.

3.2 Link budget estimation

In this section it is examined whether the range of the theoretically covered mission area is fulfilled according to the requirements. For this purpose, the link margins of the participants that can freely move and the base station, at a distance of $r_{\min} = 7, 5\text{km}$ from the repeater, are determined. If their margins are around 20dB to 30dB, the range requirement for the case described in the subsection 2.4.3 is met. Regarding the Motorola Mototrbo radio devices, it can then be said that the BER within the theoretically covered mission area is less than 5%. After evaluating the results, the radio device – from the group of participants that can freely move – with the smallest fade margin is determined and the radius r_{BSt} is calculated.

Table 3.9 provides a summary of the designed voice communication system discussed in the previous section in relation to the link budget. For completeness it is mentioned that $G_{\text{ant,dB}}$ in (dBi) is the antenna gain, $L_{\text{tot,dB}}$ in (dB) is the total loss of the antenna feed line and h_{ant} in (dB) is the antenna height above the ground, of a certain radio system.

Since the Austrian authorities have only permitted a maximum transmission power of $P_T = 5\text{W}$, the case in which this is the maximum transmission power of the base station and the repeater is also taken into account. Table 3.10 summarizes this with the new EIRP_{dBW} for these radio systems marked in orange.

Radio system	$EIRP_{dBW}$	$P_{min,dBW}$	$G_{ant,dBi}$	$L_{tot,dB}$	h_{ant}
BSt	17, 479dBW	-149, 031dBW	3, 5dBi	1, 987dB	3, 6m
REP	13, 5dBW	-149, 031dBW	3, 5dBi	0, 849dB	8m
SER	4, 771dBW	-149, 031dBW	0dBi	0dB	1, 55m
SFTY	4, 771dBW	-149, 031dBW	0dBi	0dB	1, 271m
OSS	6, 99dBW	-147, 447dBW	0dBi	0dB	1, 271m

Table 3.9: Specifications of the designed voice communication system when all participants transmit at maximum power.

Radio system	$EIRP_{dBW}$	$P_{min,dBW}$	$G_{ant,dBi}$	$L_{tot,dB}$	h_{ant}
BSt	10, 49dBW	-149, 031dBW	3, 5dBi	1, 987dB	3, 6m
REP	10, 49dBW	-149, 031dBW	3, 5dBi	0, 849dB	8m
SER	4, 771dBW	-149, 031dBW	0dBi	0dB	1, 55m
SFTY	4, 771dBW	-149, 031dBW	0dBi	0dB	1, 271m
OSS	6, 99dBW	-147, 447dBW	0dBi	0dB	1, 271m

Table 3.10: Specifications of the designed voice communication system when all participants are limited to a maximum transmission power of $P_T = 5\text{W}$.

3.2.1 Communication links and fade margin

If the radio system parameters in the table 3.9 – for maximum transmission power – and the distance $d \hat{=} r_{min} = 7,5\text{km}$ are now used in the equation (2.108), the results in the table 3.11 are obtained. The arrows in the column called **Link** represent the

Link	$PEPL_{dB}$	$P_{R,dBW}$	Fade margin
SER → REP	133, 134dB	-125, 712dBW	23, 319dB
SER ← REP	133, 134dB	-120, 483dBW	28, 548dB
OSS → REP	134, 858dB	-125, 217dBW	23, 841dB
OSS ← REP	134, 858dB	-122, 207dBW	25, 24dB
BSt → REP	125, 815dB	-107, 672dBW	41, 359dB
BSt ← REP	125, 815dB	-111, 651dBW	37, 38dB
SFTY → REP	134, 858dB	-127, 436dBW	21, 595dB
SFTY ← REP	134, 858dB	-122, 207dBW	26, 824dB

Table 3.11: Results of the plane earth signal budget calculation for the designed voice communication system when all participants transmit at maximum power.

communication direction.

In the same way the results in the table 3.12 are obtained. However, these apply when the voice communication system is limited to a maximum transmission power of $P_T = 5\text{W}$. Those radio links on which this has an effect are marked in orange.

Link	$PEPL_{dB}$	$P_{R,dBW}$	Fade margin
SER → REP	133, 134dB	-125, 712dBW	23, 319dB
SER ← REP	133, 134dB	-123, 493dBW	25, 538dB
OSS → REP	134, 858dB	-125, 217dBW	23, 841dB
OSS ← REP	134, 858dB	-125, 217dBW	22, 23dB
BSt → REP	125, 815dB	-114, 661dBW	34, 37dB
BSt ← REP	125, 815dB	-114, 661dBW	34, 37dB
SFTY → REP	134, 858dB	-127, 436dBW	21, 595dB
SFTY ← REP	134, 858dB	-125, 217dBW	23, 841dB

Table 3.12: Results of the plane earth signal budget calculation for the designed voice communication system when all participants are limited to a maximum transmission power of $P_T = 5\text{W}$.

From both tables it can be seen that the link margins marked in green are above 20dB. The lowest link margin is 21,595dB and it occurs when a safety officer is 7,5km away from the repeater and communicates through it.

Due to the fact that the plane earth model is used, these calculations are only estimations. In order to study the performance of the designed voice communication system in more detail, experiments must be carried out on it in order to obtain empirical data.

In theory, the safety officers and AAs, with each group being located somewhere within a distance of $r_{\min} = 7,5\text{km}$ around the repeater, can communicate – via said repeater – with each other. In practice, however, it is important that both groups maintain LOS either to the repeater or to each other and that the OeWF uses the topology of the mission area to the advantage of the designed voice communication system. If there are elevations in the mission area, then these should preferably be used as installation sites of the base station and the repeater. This increases their antenna heights and thus their fade margins. Depending on the topology of the mission area, the LOS can be maintained more easily with antennas being mounted at higher locations. If LOS cannot be maintained due to the topology of the mission area, this compromise must be made, and if necessary, the mission planning must be adapted to it.

3.2.2 Additional coverage area around the base station

As shown in the figure 3.2, the participants of the designed voice communication system that can freely move also receive a transmitted signal from the base station at a distance r_{BSt} around it. So that the link margin of 21,595dB for the least powerfull radio device is constant in the entire system, the distance r_{BSt} follows from transforming the equation (2.108) to:

$$r_{\text{BSt}} = \sqrt{\frac{1,271 \cdot 3,6\text{m}^2}{10 \left(\frac{-127,436\text{dBW} - 4,771\text{dBW} - 3,5\text{dBi} + 1,987\text{dB}}{20\text{dB}} \right)}} \quad (3.15)$$

$$= 4712,20\text{m}.$$

In this case there is no need to differentiate between the maximum transmission power and the transmission power limited to 5W of the base station, since the 3W transmission power of the safety officer's radio is the decisive factor.

Since the repeater may not receive the signal from the safety officers and the AAs in this area, it is necessary to calculate the maximum distance that the safety officers can take to the AAs. It is calculated in the same manner as the equation (3.15) and results in:

$$r_{\text{SER,SFTY}} = \sqrt{\frac{1,271 \cdot 1,55\text{m}^2}{10 \left(\frac{-127,436\text{dBW} - 4,771\text{dBW}}{20\text{dB}} \right)}} = 2834,09\text{m}. \quad (3.16)$$

The distances calculated in the equations (3.15) and (3.16) may appear large, but what has already been mentioned in the section 3.2.1 must be taken into account.

3.3 Self-sufficient energy distribution system

Now the self-sufficient energy distribution system of the repeater radio infrastructure is being examined. For this purpose, the PV generators used are first introduced and their behavior for different values of the PV cell temperature ϑ_C and the solar irradiance E_G is examined based on the model mentioned in the subsection 2.3.6. The LiFePO₄ battery used is then introduced and the results from the experiments discussed in the subsection 2.3.8 are presented. Finally, the remaining components required for the self-sufficient energy distribution system are introduced and a performance estimation based on a **MATLAB** simulation (see appendix C.1) is carried out in order to assess whether it can supply the repeater radio infrastructure with electrical energy.

3.3.1 Photovoltaic generator model

In general, two different PV generators are examined. Namely the AE Solar AE195SMM6-36 and the DAS Energy DAS145PF. Only one (primary) PV generator is used to supply the repeater radio infrastructure with electrical energy, with the second one serving as a backup. The backup PV generator is installed when the primary one fails to convert the required amount of electrical energy. This is the case, for example, if it gets damaged during an ongoing mission. Since both PV generators have a similar power output P_{PV} , it is up to the OeWF to decide which one is used as the primary and which one as the backup. Excerpts from their data sheets can be found in the tables 3.13 and 3.14.

AE Solar AE195SMM6-36 specifications	
PV cell type	5BB Monocrystalline
PV cell area	156, 75 · 156, 75 mm ²
Number of PV cells	36 (4 · 9)
Wind load	244 kg m ⁻²
Mechanical load	550 kg/m ²
Operating temperature	-40°C to 85°C
Maximum system voltage	1000 V
Maximum series fuse rating	10 A
Short-circuit current	9, 79 A
Open-circuit voltage	25, 87 V
MPP current	9, 11 A
MPP voltage	21, 41 V
Nominal MPP power	195, 0 W (peak)
NOCT	45 ± 2°C
Efficiency	19, 25%
Temperature coeff. for P_{MPP}	-0, 380% °C ⁻¹
Temperature coeff. for U_{OC}	-0, 290% °C ⁻¹
Temperature coeff. for I_{SC}	0, 050% °C ⁻¹

Table 3.13: Excerpt from the data sheet of the AE Solar AE195SMM6-36 PV generator at STC [87].

As can be seen from the results of the **MAPLE** source code in the appendix C.2, it makes little difference for the first few decimal places if the model is approximated with the Jacobian matrix. In the **MAPLE** source code, the caluclations are performed for the AE Solar AE195SMM6-36 PV generator, with its PV cell temperature being $\vartheta_C = 25^\circ\text{C}$ and the total irradiance onto its inclined surface being

DAS Energy DAS145PF specifications	
PV cell type	3BB Polycrystalline
PV cell area	156, 75 · 156, 75mm ²
Number of PV cells	36 (4 · 9)
Operating temperature	-40°C to 85°C
Maximum system voltage	1000V
Maximum series fuse rating	20A
Short-circuit current	8, 69A
Open-circuit voltage	22, 85V
MPP current	8, 19A
MPP voltage	18, 69V
Nominal MPP power	153, 1W (peak)
Temperature coeff. for P_{MPP}	-0, 393%°C ⁻¹
Temperature coeff. for U_{OC}	-0, 310%°C ⁻¹
Temperature coeff. for I_{SC}	0, 051%°C ⁻¹

Table 3.14: Excerpt from the data sheet of the DAS Energy DAS145PF PV generator at STC [88].

$E_G = 200\text{Wm}^{-2}$. These results can be replicated for the DAS Energy DAS145PF PV generator and for other values of ϑ_C and E_G as well. Therefore, it can be said that the starting values shown in the equation (2.52) suffice as a good approximation for the PV generator's open-circuit voltage U_{OC} and reverse saturation current I_S . This is because I_S is usually very small [11], [13].

The results for the modeled current-voltage and power-voltage characteristics of the AE Solar AE195SMM6-36 PV generator, depending on either the total irradiance onto its inclined surface E_G or on its PV cell temperature ϑ_C , can be seen in the figures 3.9, 3.11, 3.13 and 3.15. If it depends on E_G it is assumed that $\vartheta_C = 25^\circ\text{C}$ is constant, and if it depends on ϑ_C it is assumed that $E_G = 1000\text{Wm}^{-2}$ is constant. These constant values for ϑ_C and E_G were chosen because they represent the STCs. Identically, the results for the DAS Energy DAS145PF PV generator can be taken from the figures 3.10, 3.12, 3.14 and 3.16. All results were obtained by programming the discussed model of a PV generator in MATLAB.

From the current-voltage characteristics for different irradiance levels E_G of both PV generators shown in the figures 3.9 and 3.10, it can be seen that the short-circuit current I_{SC} decreases faster than the open-circuit voltage U_{OC} . This is due to the fact that $I_{Ph} = I_{SC}$ is proportional to E_G (compare to equation (2.42)), while U_{OC} changes with the natural logarithm to it (compare to equations (2.44) and 2.52)) [11].

Now the associated power-voltage characteristics for different irradiance levels E_G of both PV generators can be calculated by using the equation (2.55), as shown in the figures 3.11 and 3.12. As can be observed from a real PV generator, the power output P_{PV} decreases with lower irradiance levels E_G .

Another interesting behavior of the PV generators can be observed for different temperatures ϑ_C of their PV cells. Due to the temperature increase of the semiconductors, the current $I_{Ph} = I_{SC}$ increases, however not as much as the voltage U_{OC} decreases. This finding results in an overall decrease in the power output P_{PV} of the PV generators for rising temperatures ϑ_C . Similarly, such behavior can be observed for decreasing temperatures ϑ_C . Here the overall power output P_{PV} increases. This is shown in the figures 3.13 and 3.14. When modeling a self-sufficient energy system, this factor must therefore not be neglected [11].

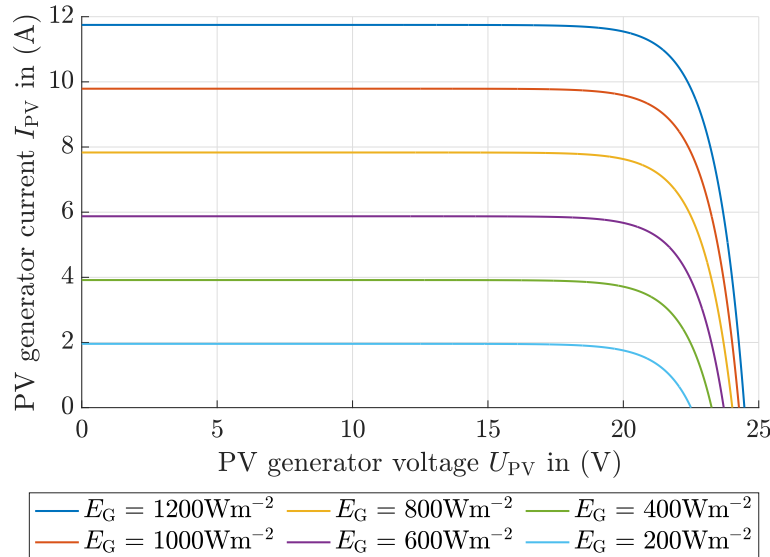


Figure 3.9: Modeled current-voltage characteristic of the AE Solar AE195SMM6-36 PV generator, depending on the total irradiance onto its inclined surface E_G . The PV cell temperature $\vartheta_C = 25^\circ\text{C}$ is assumed to be constant.

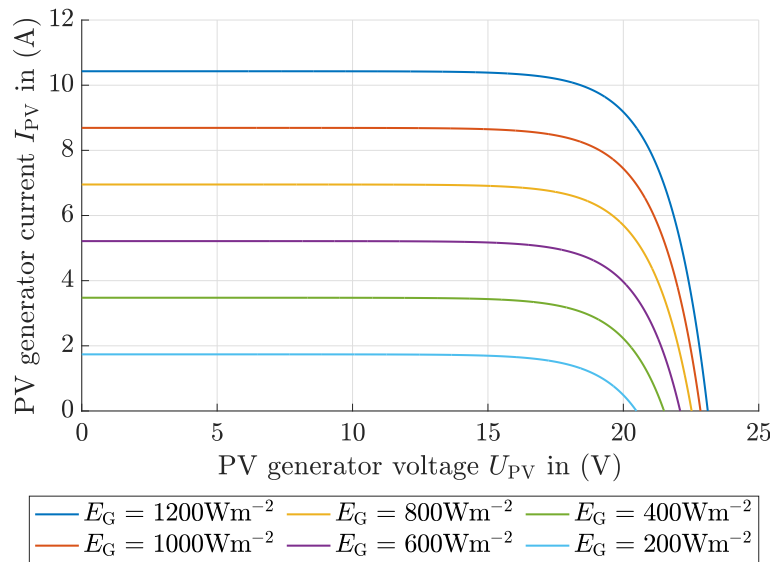


Figure 3.10: Modeled current-voltage characteristic of the DAS Energy DAS145PF PV generator, depending on the total irradiance onto its inclined surface E_G . The PV cell temperature $\vartheta_C = 25^\circ\text{C}$ is assumed to be constant.

With the help of the aforementioned **MATLAB** program, the ideality factors of the two PV generators were empirically determined in such a way that their power output at MPP for STCs corresponds to that in their data sheets. This resulted in an ideality factor of $m = 1,19045$ for the AE Solar AE195SMM6-36 PV generator and $m = 1,58972$ for the DAS Energy DAS145PF PV generator – for an accuracy of two decimal places.

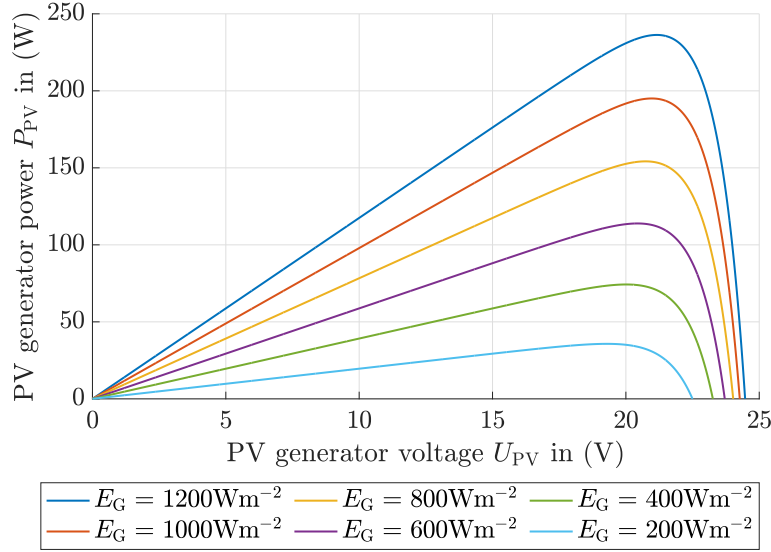


Figure 3.11: Modeled power-voltage characteristic of the AE Solar AE195SMM6-36 PV generator, depending on the total irradiance onto its inclined surface E_G . The PV cell temperature $\vartheta_C = 25^\circ\text{C}$ is assumed to be constant.

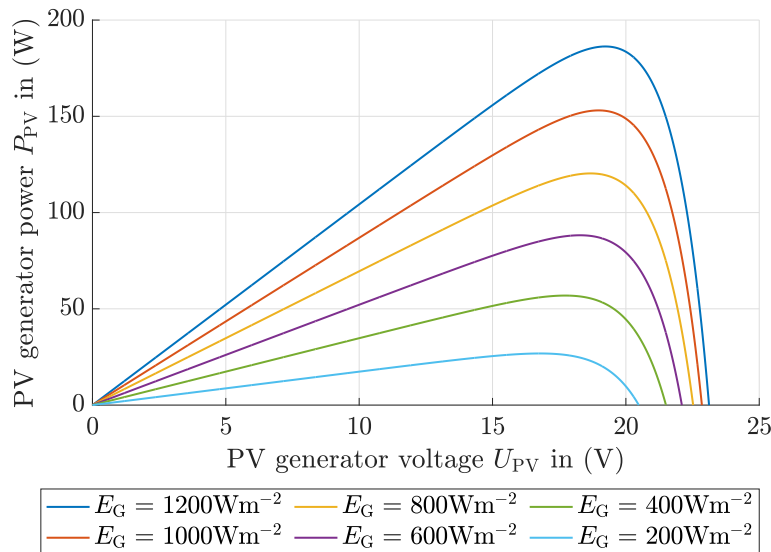


Figure 3.12: Modeled power-voltage characteristic of the DAS Energy DAS145PF PV generator, depending on the total irradiance onto its inclined surface E_G . The PV cell temperature $\vartheta_C = 25^\circ\text{C}$ is assumed to be constant.

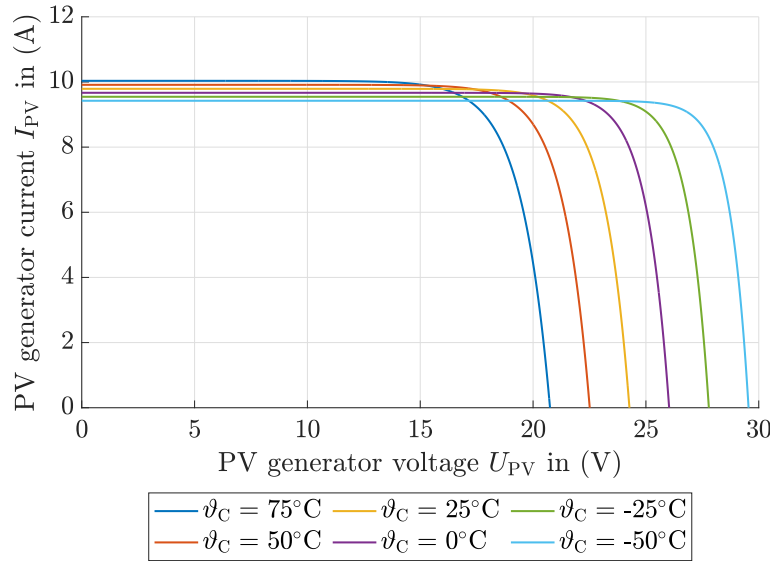


Figure 3.13: Modeled current-voltage characteristic of the AE Solar AE195SMM6-36 PV generator, depending on its PV cell temperature ϑ_C . The total irradiance onto its inclined surface $E_G = 1000\text{Wm}^{-2}$ is assumed to be constant.

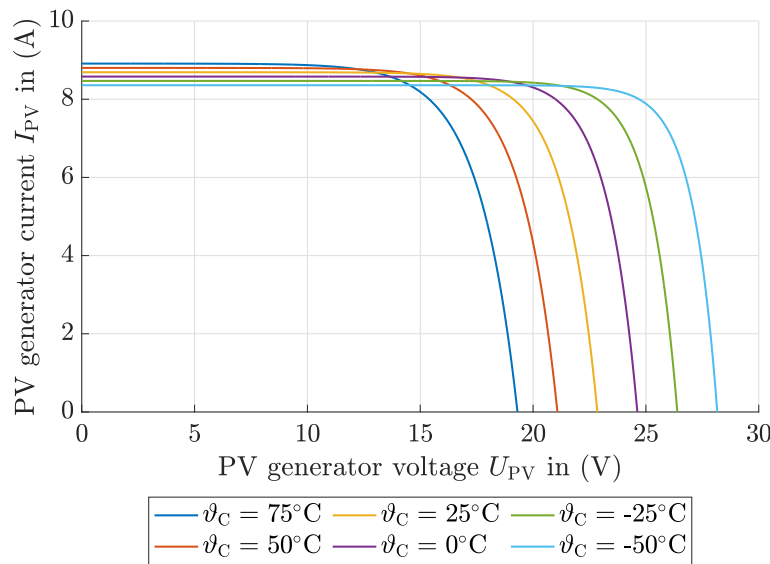


Figure 3.14: Modeled current-voltage characteristic of the DAS Energy DAS145PF PV generator, depending on its PV cell temperature ϑ_C . The total irradiance onto its inclined surface $E_G = 1000\text{Wm}^{-2}$ is assumed to be constant.

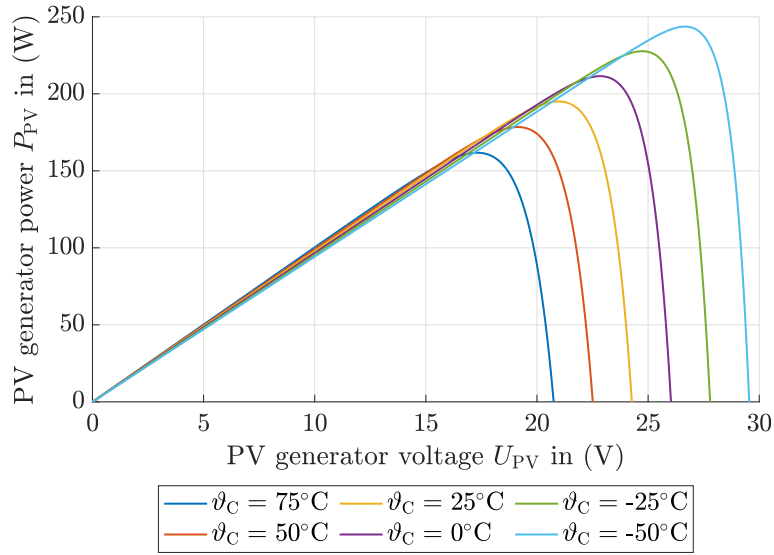


Figure 3.15: Modeled power-voltage characteristic of the AE Solar AE195SMM6-36 PV generator, depending on its PV cell temperature ϑ_C . The total irradiance onto its inclined surface $E_G = 1000 \text{ W m}^{-2}$ is assumed to be constant.

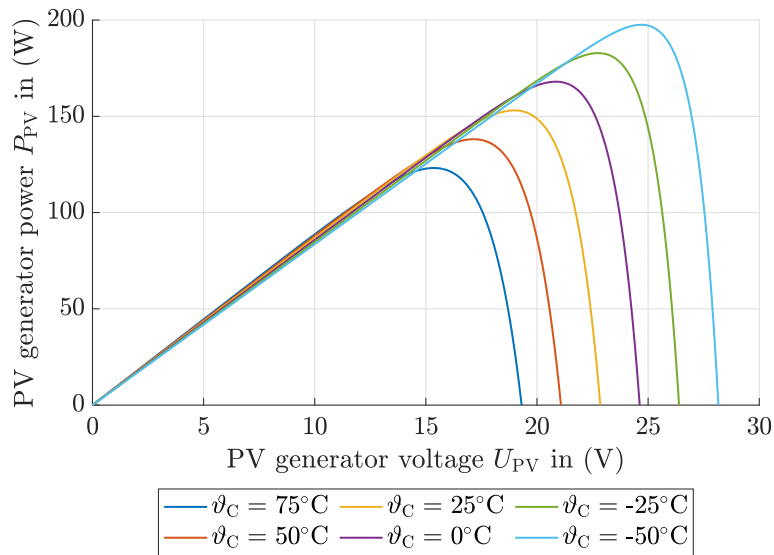


Figure 3.16: Modeled power-voltage characteristic of the DAS Energy DAS145PF PV generator, depending on its PV cell temperature ϑ_C . The total irradiance onto its inclined surface $E_G = 1000 \text{ W m}^{-2}$ is assumed to be constant.

3.3.2 LiFePO₄ battery model

As already mentioned, the Offgridtec Smart-Pro 12,8V 50Ah LiFePO₄ battery – which from now on will simply be referred to as battery – is used to store the electrical energy converted by the PV generator and to supply the repeater radio infrastructure with it. Table 3.15 contains an excerpt from the data sheet for this battery, with which the nominal current of the battery can be calculated using the equation (2.67) to $I_{\text{nom}} = 16,67\text{A}$.

Offgridtec Smart-Pro 12,8V 50Ah specifications	
Nominal charge for $C_D = 1/3\text{h}^{-1}$	50Ah
Nominal discharging current	16,7A
Nominal voltage	12,8V
Working voltage	11,0V to 14,6V
Maximum continuous discharging current	50A
Recommended continuous discharging current	20A
Maximum charging current	50A
Recommended charging current	25A
Maximum charging voltage	$14,4 \pm 0,2\text{V}$
Float charge voltage	$13,8 \pm 0,2\text{V}$
Minimum number of cycles	> 2500
Charging temperature	-20°C to 60°C
Discharging temperature	-5°C to 45°C
Storage temperature (20% to 75% humidity)	0°C to 20°C
BMS	Integrated
Bluetooth	Integrated

Table 3.15: Excerpt from the data sheet of the Offgridtec Smart-Pro 12,8V 50Ah LiFePO₄ battery [63].

So that this battery can be used with the **MATLAB** simulation in the appendix C.1, the discharging and charging experiments discussed in the subsection 2.3.8 had to be carried out. The laboratory equipment required for these experiments is listed in the table 3.16. A total of four electronic loads connected in parallel were used.

Laboratory equipment	
Oscilloscope	Keysight DSOX 1102G
Shunt resistor	Lumel 60mV 50A (1,2mΩ)
Electronic load	FTVOGUE17cm0w5uh2
Battery charger	Mean Well ENC-180-12

Table 3.16: Laboratory equipment required to carry out the discharging and charging experiment with the Offgridtec Smart-Pro 12,8V 50Ah LiFePO₄ battery.

This was done because each electronic load could only convert a maximum power of 60W into heat. To assure that these were switched on and off at the same time, a central button for all electronic loads was used.

Before the experiments were carried out, the internal resistances of the input channels 1 and 2 of the oscilloscope were measured. These measurements resulted in $R_{\text{Ch1}} = 1011,68\text{k}\Omega$ for Ch1 and $R_{\text{Ch2}} = 1004,99\text{k}\Omega$ for Ch2. Taking into account the battery voltage U_B for the upper left and the current divider rule for the upper right loop in the figures 2.20 and 2.22, it was determined that the resulting currents I_{Ch1} and I_{Ch2} are negligibly small. This applies because during the discharging experiment I_L was set so that I_D is equal to I_{nom} and during the charging experiment

the battery charger provides a current of $I_{BC} = 12A$ [89]. It is noted that neglecting I_{Ch1} and I_{Ch2} has the consequence that $I_D = I_L$ and $I_C = I_{BC}$.

Both experiments were carried out in such a way that measuring points were recorded in 0,05 steps of the SOC. Thus, $N_{MP} = 21$ measuring points had to be recorded per experiment. Based on this – while taking into account the equation (2.66) and that $\eta_C = 1$ – the equations (2.73) and (2.80) result in $\Delta t_D = 8,98\text{min}$ and $\Delta t_C = 12,5\text{min}$. Since the battery has integrated Bluetooth, its SOC was additionally observed – in parallel to a set timer – using the Offgridtec Battery Viewer Smart Android app provided by Offgridtec GmbH.

In order to get to the next measuring point, the battery had to be discharged with I_D over the time interval Δt_D or charged with I_C over the time interval Δt_C . When this measuring point was reached, the currents were switched off. After 20min it could be clearly observed with Ch1 of the oscilloscope that the battery voltage hardly changed. Therefore t_{rest} was set to this time. At each measuring point the ambient temperature ϑ_A was measured with a Newentor weather station (ASIN: B08M6C4MCM). This resulted in a *mean ambient temperature* during the discharging experiment of $\bar{\vartheta}_{A,D} = 23,99^\circ\text{C}$ and during the charging experiment of $\bar{\vartheta}_{A,C} = 25,23^\circ\text{C}$.

Two recorded measurements for the discharging and charging experiment for $SOC_n = 0,5$ can be seen in the figures 3.17 and 3.18. The blue y-axes represent Ch1 and the green y-axes represent Ch2 of the oscilloscope. The green continuous lines are the currents $I_D(t)$ and $I_C(t)$ and the blue continuous lines are the battery voltages $U_B(t)$ for the respective experiments. Furthermore, several cursors can be seen. In the case of the currents $I_D(t)$ and $I_C(t)$, the green dash-dotted cursor indicates their top value, and the green dashed cursor indicates their bottom value. In the case of the battery voltages $U_B(t)$, the blue cursors mark the voltage drop for both experiments. The voltage drop instead of the voltage rise was used for the charging experiment because the observed rising slope was not steep enough – after switching on $I_C(t)$. This could falsify the result for calculating the electrolyte resistance $R_{e,C}(SOC_n)$. Similar to the currents, the blue dash-dotted cursor represents the top value of the voltage drop and the blue dashed cursor the bottom value of the voltage drop.

The time courses of the channels 1 and 2 shown in the figures 3.17 and 3.18 were recorded with the oscilloscope for all measuring points, with each being saved in a separate .cvs file. Subsequently, the data in the .cvs files were processed with a MATLAB program, in which the function `ischange()` was used to determine the positions of the cursors. The currents $I_D(SOC_n)$ and $I_C(SOC_n)$ as well as the voltage drops $\Delta U_D(SOC_n)$ and $\Delta U_C(SOC_n)$ were then calculated by subtracting their respective dashed cursor from their dash-dotted cursor. Now that all the required parameters were known, the electrolyte resistances $R_{e,D}(SOC_n)$ and $R_{e,C}(SOC_n)$ were determined using the equations (2.75) and (2.82).

For completeness it must be mentioned that the scales of the green y-axes from the figures 3.17 and 3.18 were calculated with this MATLAB program by extracting the Ch2 data – which represents the measured voltage drop across the shunt resistor – from the .cvs files and applying it to the equations (2.72) and (2.79).

It should further be noted that Δt_D and Δt_C cannot be seen in the figures 3.17 and 3.18, since these are the time intervals between two successive measuring points. The time interval between switching the discharging or charging current

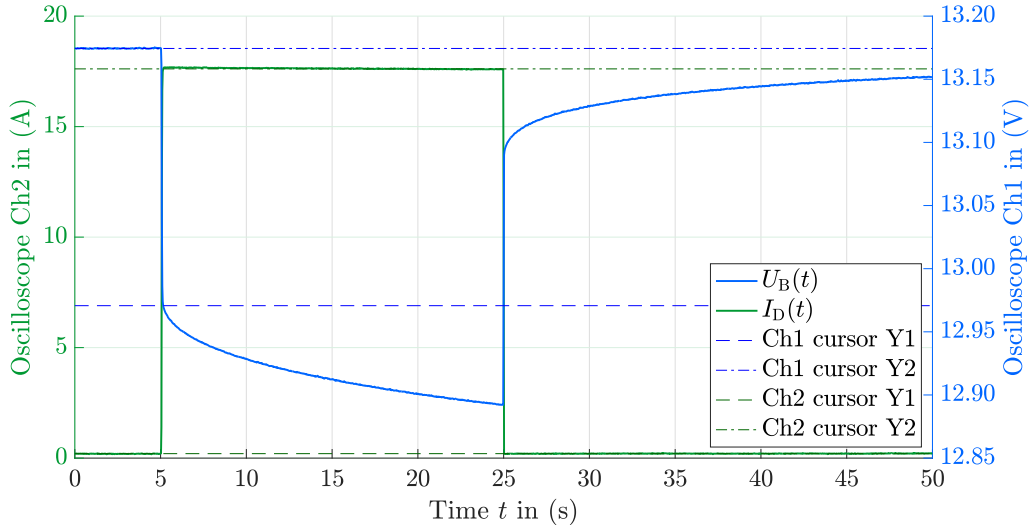


Figure 3.17: Recorded time courses of $U_B(t)$ and $I_D(t)$ during the discharging experiment for $SOC_n = 0, 50$. The device under test was the Offgridtec Smart-Pro 12,8V 50Ah LiFePO₄ battery.

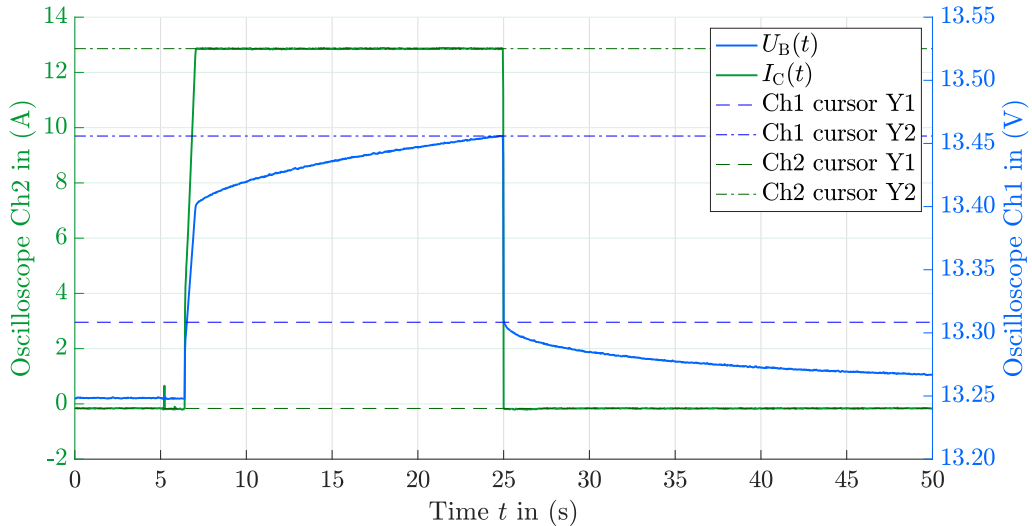


Figure 3.18: Recorded time courses of $U_B(t)$ and $I_C(t)$ during the charging experiment for $SOC_n = 0, 50$. The device under test was the Offgridtec Smart-Pro 12,8V 50Ah LiFePO₄ battery.

on and off – for a certain measuring point – was determined during the course of the experiments. When t_{rest} was over, the open-circuit voltages $U_{0,D}(\text{SOC}_n)$ and $U_{0,C}(\text{SOC}_n)$ were measured, the time scale of the oscilloscope was set to 50s and Ch1 was triggered manually. After approximately 5s, either the electronic load or the charger was switched on manually. After another 20s these were switched off again. This approach gave the best results. From the measured open-circuit voltages, $U_0(\text{SOC}_n)$ was calculated with the equation (2.84).

The results of the experiments are summarized in the table 3.17 and visualized in the figures 3.19 and 3.20. To obtain the battery model, these now only have to be interpolated and inserted into the equation (2.83).

Now it only remains to be shown that the assumptions for the equations (2.76) and (2.77) are correct. For this purpose, the course of the charging current $I_C(t)$ during the CV charging phase was measured for $\text{SOC} \approx 0, 99$ – which was monitored via the Offgridtec Battery Viewer Smart app – with Ch2 of the oscilloscope. The

SOC_n	$R_{e,D}(SOC_n)$	$R_{e,C}(SOC_n)$	$U_{0,D}(SOC_n)$	$U_{0,C}(SOC_n)$	$U_0(SOC_n)$
1,00	0,0121Ω	0,0121Ω	13,877V	14,107V	13,9920V
0,95	0,0117Ω	0,0113Ω	13,315V	13,387V	13,3510V
0,90	0,0118Ω	0,0115Ω	13,319V	13,393V	13,3560V
0,85	0,0117Ω	0,0114Ω	13,322V	13,401V	13,3615V
0,80	0,0116Ω	0,0115Ω	13,320V	13,415V	13,3675V
0,75	0,0116Ω	0,0116Ω	13,306V	13,388V	13,3470V
0,70	0,0117Ω	0,0112Ω	13,248V	13,387V	13,3175V
0,65	0,0116Ω	0,0112Ω	13,196V	13,275V	13,2355V
0,60	0,0116Ω	0,0111Ω	13,181V	13,272V	13,2265V
0,55	0,0117Ω	0,0112Ω	13,117V	13,253V	13,1850V
0,50	0,0117Ω	0,0113Ω	13,174V	13,250V	13,2120V
0,45	0,0117Ω	0,0113Ω	13,172V	13,248V	13,2100V
0,40	0,0118Ω	0,0114Ω	13,169V	13,250V	13,2095V
0,35	0,0118Ω	0,0115Ω	13,111V	13,244V	13,1775V
0,30	0,0118Ω	0,0114Ω	13,087V	13,225V	13,1560V
0,25	0,0118Ω	0,0115Ω	13,012V	13,179V	13,0955V
0,20	0,0118Ω	0,0116Ω	12,931V	13,089V	13,0100V
0,15	0,0118Ω	0,0115Ω	12,837V	12,958V	12,8975V
0,10	0,0117Ω	0,0117Ω	12,814V	12,923V	12,8685V
0,05	0,0118Ω	0,0118Ω	12,350V	12,502V	12,4260V
0,00	0,0121Ω	0,0121Ω	11,371V	11,420V	11,3955V

Table 3.17: Calculated results from the discharging and charging experiment carried out on the Offgridtec Smart-Pro 12,8V 50Ah LiFePO₄ battery.

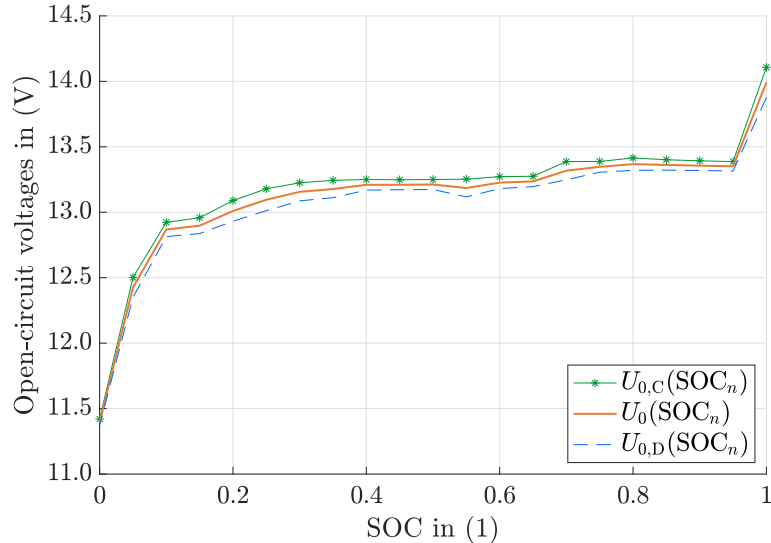


Figure 3.19: Open-circuit voltages $U_{0,C}(SOC_n)$, $U_0(SOC_n)$ and $U_{0,D}(SOC_n)$ obtained from the discharging and charging experiment carried out on the Offgridtec Smart-Pro 12,8V 50Ah LiFePO₄ battery.

result can be seen in the figure 3.21, with the red continuous line representing the measured charging current. To prepare this measurement, the charging process of the almost fully charged battery ($SOC \approx 0,99$) was switched off as soon as a decrease in the charging current was observed with Ch2 of the oscilloscope. This indicated that the battery charger was transitioning from the CC to the CV charging phase. Thereafter the battery was left to rest for 20min. The measurement was then recorded by setting the time scale of the oszilloscope to 8min, triggering Ch2 manually and continuing the charging process. First, the battery charger went into

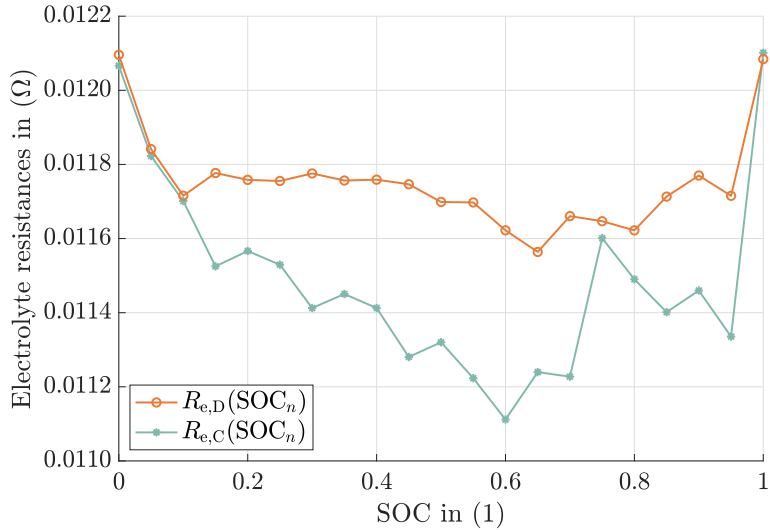


Figure 3.20: Electrolyte resistances $R_{e,D}(SOC_n)$ and $R_{e,C}(SOC_n)$ obtained from the discharging and charging experiment carried out on the Offgridtec Smart-Pro 12,8V 50Ah LiFePO₄ battery.

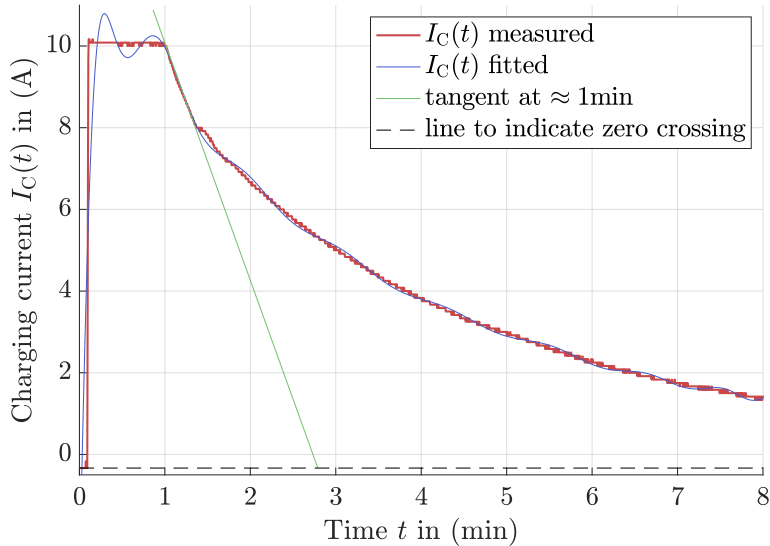


Figure 3.21: Time course of $I_C(t)$ over time during the CV charging phase of the Mean Well ENC-180-12 battery charger. The charged device was the Offgridtec Smart-Pro 12,8V 50Ah LiFePO₄ battery.

the CC charging phase and then, $t_1 = 1\text{min}$ after the start of the measurement, into the CV charging phase. No steep drop in the charging current can be seen from the recorded measurement (compare to figure 3.21). Thus, the described model for charging and discharging the battery from the equations (2.76) and (2.77) is used for the **MATLAB** simulation in the appendix C.1.

As can be seen, the measured data was fitted with a polynomial function illustrated with the blue continuous line. The tangent of the polynomial fitting function, illustrated with the green continuous line, was chosen so that it runs through the point in time $t_1 = 1\text{min}$ – at which the battery charger changes from the CC to the CV charging phase. The top and bottom values of the charging current are 10,167A and -0,333A, with the difference between these values being the charging current in the CC charging phase $I_C = 10,5\text{A}$. Based on the bottom value, the black dashed line indicates the zero crossing of the measured $I_C(t)$. The intersection with this

line and the tangent is at $t_2 = 2,7904\text{min}$. Hence, the measured time constant of the battery follows to:

$$\tau_B = t_2 - t_1 = 1,7904\text{min}. \quad (3.17)$$

It can be seen from the figures 3.17, 3.18 and 3.21 that the top and bottom values for the currents I_D and I_C do not quite match the values I_{nom} and I_{BC} . This is likely due to the electronic loads and the battery charger. Since the behavior of these devices is only known from their data sheets, further investigations must be carried out in order to obtain more precise results. Alternatively, more professional devices that are certified for laboratory use can be used. Finally, a resistance measurement of the shunt resistor can be carried out in order to determine its exact resistance value.

3.3.3 Performance estimation

Now the results of the performance estimation of the self-sufficient energy distribution system for two different mission locations on Earth are presented. First for the Negev Desert in Israel, as the OeWF's next analog Mars field mission AMADEE-20 will take place there from October 4th to October 31st, 2021, and then for Vienna, Austria, from April 1st to April 30th, as this is the location where the assembled voice communication system will probably be tested.

Before the simulated results are presented, the SCC must first be briefly introduced. For the self-sufficient energy distribution system, the Victron Energy BlueSolar MPPT 75/10 solar charging controller is used. Its specifications are listed in the table 3.18. According to the user manual of this SCC, it only connects the PV

Victron BlueSolar MPPT 75/10 specifications	
Battery voltage	12V
Maximum battery current	10A
Maximum PV generator power	145W
Maximum PV generator short-circuit current	13A
Maximum load current	15A
CV charging voltage	14,4V
Float charge voltage	13,8V

Table 3.18: Excerpt from the user manual of the Victron Energy BlueSolar MPPT 75/10 solar charging controller [90].

generator when a voltage of $U_{\text{in},\text{PV}} > U_B + 5\text{V}$ is reached at its PV generator input terminal. It is noted that $U_{\text{in},\text{PV}}$ already takes the cable losses into account. After this condition is met, the PV generator remains connected to the battery and the load as long as the new condition $U_{\text{in},\text{PV}} > U_B + 1\text{V}$ is fulfilled. In its user manual it is also mentioned that the maximum power of the PV generator must not exceed 145W. If the power is exceeded, the SCC limits the current from said generator [90].

The **MATLAB** simulation in the appendix C.1 is based on the user manual of the Victron BlueSolar MPPT 75/10 SCC, the results presented in the subsections 3.3.1 and 3.3.2 and the basics explained in the section 2.3.

Although it was mentioned in the subsection 2.4.1 that a step function can be implemented for the load current, this was not successful in **MATLAB**. It should also be noted that the battery charging process explained in the subsection 2.3.8 was

not implemented due to the effort involved. Instead, the equation 2.64 was used, which models a linear increase or decrease in the SOC of the battery.

The aim of the **MATLAB** simulation is to calculate how the PV generator must be installed at the mission location so that it can maximize its daily electrical energy yield throughout the mission. Based on the daily electrical energy yield, the **MATLAB** simulation calculates the SOC of the battery for each mission day. It then gives a feedback if the the battery can be fully charged during the course of the mission. If this is the case, it is likely that the repeater radio system can be supplied with enough electrical energy. However, if the battery cannot be fully charged during the course of the mission, one or more PV generators must be connected in parallel to the existing one to increase the current I_{MPP} , and thus P_{MPP} , of the PV generator array [11]. For completeness it is noted that the **MATLAB** simulation assumes that the PV generators connected in parallel are the same type. In addition to that, the simulation can throw several error messages if either the conditions in the equations 2.8 and 2.9 are not met, the voltage at the repeater is too low or to high, or if the battery gets fully discharged during the course of the mission.

Based on the simulation inputs for the Negev Desert in Israel and for Vienna, Austria, in the tables 3.19 and 3.20, the command window outputs of the **MATLAB** simulation result in the listings 3.1 and 3.2 for the Negev Desert and in the listings 3.3 and 3.4 for Vienna. The global horizontal irradiation, direct normal irradiation and average ambient temperature for the Negev Desert can be obtained from the figures 3.22 to 3.24 and for Vienna from the figures 2.5, 2.6 and 2.14.

Simulation input for the Negev Desert in Israel	
Latitude	30, 500° N
Longitude	34, 917° E
Date of mission start	October 4 th 2021
Date of mission end	October 31 st 2021
Daily mission start (UTC)	4:00h
Daily mission end (UTC)	14:00h
Average ambient temperature	22, 3°C
Global horizontal irradiation	6, 05kWhm ⁻²
Direct normal irradiation	6, 85kWhm ⁻²
Albedo of the ground (Sand)	0, 30
Repeater radio system duty cycle ($a_T/a_R/a_{Stby}$)	20%/20%/60%
PV generator	AE Solar AE195SMM6-36
Number of PV generators	1
Initial state of charge of the battery	0, 6

Table 3.19: Input for the **MATLAB** simulation of the self-sufficient energy distribution system for the Negev Desert in Israel.

Listing 3.1 shows the optimal angle of inclination – or tilting angle – β and the orientation of the normal to the PV generator's energy converting surface A_{PV} , with respect to the cardinal directions, for each mission day. As explained in the subsection 2.3.4, the optimal angle of inclination applies for solar noon $t_S = 12\text{h}$. This might not be true for cloudy days when the direct normal irradiation is weaker. During these days, β must be reduced in order to maximize E_{DIFG} and E_{RGI} (compare to equations 2.17 and 2.18), which causes E_G to increase (compare to equation 2.19). Furthermore, the simulation determines the mean angle of inclination and orientation so that the PV generator only needs to be set up once at the beginning of the mission.

Simulation input for Vienna, Austria	
Latitude	48, 210° N
Longitude	16, 363° E
Date of mission start	April 1 st 2021
Date of mission end	April 30 th 2021
Daily mission start (UTC)	5:00h
Daily mission end (UTC)	15:00h
Average ambient temperature	11, 4°C
Global horizontal irradiation	3, 25kWhm ⁻²
Direct normal irradiation	2, 90kWhm ⁻²
Albedo of the ground (Grass)	0, 25
Repeater radio system duty cycle ($a_T/a_R/a_{Stby}$)	20%/20%/60%
PV generator	AE Solar AE195SMM6-36
Number of PV generators	2 (parallel)
Initial state of charge of the battery	0, 6

Table 3.20: Input for the MATLAB simulation of the self-sufficient energy distribution system for Vienna, Austria.

Mitzpe Ramon, Southern District, Israel
30.5N, 34.917E | Elevation: 539 m | Climate Class: BWh | Years: 1990-2019

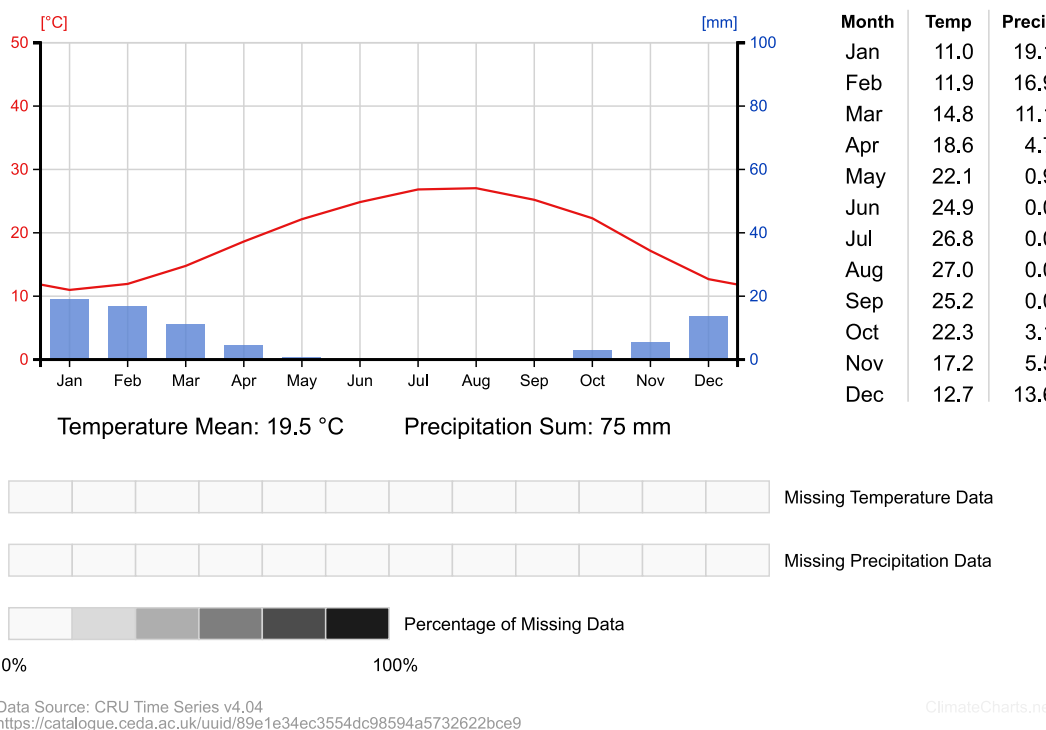


Figure 3.22: Monthly averages of temperature and precipitation data for Mitzpe Ramon, Southern District, Israel (Negev Desert). (Image credit: [54])

To display the command window output shown in the listing 3.2, the simulation uses the mean inclination angle from the listing 3.1 and calculates the daily electrical energy yield of the PV generator. On the basis of this, the SOC of the battery is calculated for each mission day. An algorithm then evaluates whether the battery has been fully charged during each mission day and outputs either YES or NO. As it can be seen, the battery cannot be fully charged for the first few mission days. This is due to the assumption that the battery is 60% charged at the beginning of

***** [OUTPUT] PV GENERATOR INSTALLATION:		
Mission day	Opt. tilt angle	Orientation
04-Oct-2021	35.78 deg	SOUTH
05-Oct-2021	36.18 deg	SOUTH
06-Oct-2021	36.57 deg	SOUTH
07-Oct-2021	36.96 deg	SOUTH
08-Oct-2021	37.34 deg	SOUTH
09-Oct-2021	37.73 deg	SOUTH
10-Oct-2021	38.11 deg	SOUTH
11-Oct-2021	38.49 deg	SOUTH
12-Oct-2021	38.87 deg	SOUTH
13-Oct-2021	39.25 deg	SOUTH
14-Oct-2021	39.62 deg	SOUTH
15-Oct-2021	39.99 deg	SOUTH
16-Oct-2021	40.36 deg	SOUTH
17-Oct-2021	40.72 deg	SOUTH
18-Oct-2021	41.08 deg	SOUTH
19-Oct-2021	41.44 deg	SOUTH
20-Oct-2021	41.80 deg	SOUTH
21-Oct-2021	42.15 deg	SOUTH
22-Oct-2021	42.50 deg	SOUTH
23-Oct-2021	42.84 deg	SOUTH
24-Oct-2021	43.18 deg	SOUTH
25-Oct-2021	43.52 deg	SOUTH
26-Oct-2021	43.86 deg	SOUTH
27-Oct-2021	44.19 deg	SOUTH
28-Oct-2021	44.51 deg	SOUTH
29-Oct-2021	44.83 deg	SOUTH
30-Oct-2021	45.15 deg	SOUTH
31-Oct-2021	45.46 deg	SOUTH

Mean | 40.80 deg | SOUTH

Listing 3.1: Output of the **MATLAB** simulation in appendix C.1 regarding the installation of the PV generator for the mission inputs in the table 3.19.

the mission – hence $\text{SOC}_{\text{init}} = 0, 6$. With this SOC, the Offgridtec Smart-Pro 12,8V 50Ah LiFePO₄ battery is stored for longer periods of time [63]. Therefore it can be said that the self-sufficient energy distribution system can supply the repeater radio system during the course of the analog Mars field mission AMADEE-20.

An interesting case occurs when the battery cannot be fully charged towards the end of the mission. This can happen, for instance, when the available solar energy is decreasing every day. Such results can be explained by changing seasons. In this case PV generators must be connected in parallel to guarantee sufficient electrical energy supply of the repeater radio system throughout the mission.

A similar command window output can be obtained from the listings 3.3 and 3.4 for Vienna. Here, however, two PV generators connected in parallel are required. Besides that, simulations have shown, that the daily electrical energy yield is increased

```
*****
[OUTPUT] PV GENERATOR ENERGY YIELD:
```

Applies for mean tilting angle and orientation. The energy yield is the electrical energy yield. SOC full shows if the battery could be fully charged during the day.

Mission day	Energy yield	SOC full
04-Oct-2021	427.74 Wh	NO
05-Oct-2021	428.65 Wh	NO
06-Oct-2021	430.23 Wh	NO
07-Oct-2021	431.09 Wh	NO
08-Oct-2021	431.92 Wh	NO
09-Oct-2021	433.41 Wh	NO
10-Oct-2021	434.17 Wh	YES
11-Oct-2021	435.61 Wh	YES
12-Oct-2021	436.31 Wh	YES
13-Oct-2021	437.69 Wh	YES
14-Oct-2021	438.32 Wh	YES
15-Oct-2021	439.64 Wh	YES
16-Oct-2021	440.21 Wh	YES
17-Oct-2021	441.46 Wh	YES
18-Oct-2021	441.96 Wh	YES
19-Oct-2021	443.15 Wh	YES
20-Oct-2021	443.58 Wh	YES
21-Oct-2021	444.71 Wh	YES
22-Oct-2021	445.80 Wh	YES
23-Oct-2021	446.12 Wh	YES
24-Oct-2021	447.15 Wh	YES
25-Oct-2021	447.40 Wh	YES
26-Oct-2021	448.37 Wh	YES
27-Oct-2021	449.30 Wh	YES
28-Oct-2021	449.44 Wh	YES
29-Oct-2021	450.30 Wh	YES
30-Oct-2021	450.37 Wh	YES
31-Oct-2021	451.16 Wh	YES

```
*****
```

Listing 3.2: Output of the **MATLAB** simulation in appendix C.1 regarding the daily energy yield of the PV generator for the mission inputs in the table 3.19.

when the angle of inclination $\beta = 0^\circ$. This can also be recognized by analyzing the solar resources maps in the figures 2.5 and 2.6, because the global horizontal irradiation is greater than the direct normal irradiation. The author of the book [11] mentions this as well. Such a simulation result can further be explained by the fact that these solar resource maps provide average values that have been recorded over several years and are therefore mainly used for the long-term planning of a PV generator array.

In order to obtain more intuitive simulation results, the SOC of the battery can be plotted over the entire duration of the mission or for individual mission days.

```
*****
[OUTPUT] PV GENERATOR INSTALLATION:

Mission day | Opt. tilt angle | Orientation
-----
01-Apr-2021 | 43.84 deg | SOUTH
02-Apr-2021 | 43.44 deg | SOUTH
03-Apr-2021 | 43.05 deg | SOUTH
04-Apr-2021 | 42.65 deg | SOUTH
05-Apr-2021 | 42.26 deg | SOUTH
06-Apr-2021 | 41.87 deg | SOUTH
07-Apr-2021 | 41.48 deg | SOUTH
08-Apr-2021 | 41.10 deg | SOUTH
09-Apr-2021 | 40.71 deg | SOUTH
10-Apr-2021 | 40.33 deg | SOUTH
11-Apr-2021 | 39.95 deg | SOUTH
12-Apr-2021 | 39.58 deg | SOUTH
13-Apr-2021 | 39.20 deg | SOUTH
14-Apr-2021 | 38.83 deg | SOUTH
15-Apr-2021 | 38.46 deg | SOUTH
16-Apr-2021 | 38.10 deg | SOUTH
17-Apr-2021 | 37.74 deg | SOUTH
18-Apr-2021 | 37.38 deg | SOUTH
19-Apr-2021 | 37.02 deg | SOUTH
20-Apr-2021 | 36.67 deg | SOUTH
21-Apr-2021 | 36.32 deg | SOUTH
22-Apr-2021 | 35.97 deg | SOUTH
23-Apr-2021 | 35.63 deg | SOUTH
24-Apr-2021 | 35.29 deg | SOUTH
25-Apr-2021 | 34.95 deg | SOUTH
26-Apr-2021 | 34.62 deg | SOUTH
27-Apr-2021 | 34.30 deg | SOUTH
28-Apr-2021 | 33.97 deg | SOUTH
29-Apr-2021 | 33.65 deg | SOUTH
30-Apr-2021 | 33.34 deg | SOUTH
-----
Mean | 38.39 deg | SOUTH
```

```
*****
```

Listing 3.3: Output of the **MATLAB** simulation in appendix C.1 regarding the installation of the PV generator for the mission inputs in the table 3.20.

Since the **MATLAB** simulation only serves as a reference point, the on-site support crew still has to make regular checks of the battery's SOC during the mission in order to collect empirical data. Finally, it should be noted that the simulation could not provide any results for the DAS Energy DAS145PF PV generator, as it could not meet the condition $U_{\text{in},\text{PV}} > U_B + 5\text{V}$ with the solar resource maps mentioned. However, this could be different with the solar resource maps from [29].

```
*****  
[OUTPUT] PV GENERATOR ENERGY YIELD:
```

Applies for mean tilting angle and orientation. The energy yield is the electrical energy yield. SOC full shows if the battery could be fully charged during the day.

Mission day	Energy yield	SOC full
01-Apr-2021	490.62 Wh	NO
02-Apr-2021	490.80 Wh	NO
03-Apr-2021	490.98 Wh	YES
04-Apr-2021	491.15 Wh	YES
05-Apr-2021	491.31 Wh	YES
06-Apr-2021	491.47 Wh	YES
07-Apr-2021	491.62 Wh	YES
08-Apr-2021	491.78 Wh	YES
09-Apr-2021	491.93 Wh	YES
10-Apr-2021	492.08 Wh	YES
11-Apr-2021	492.23 Wh	YES
12-Apr-2021	492.38 Wh	YES
13-Apr-2021	492.53 Wh	YES
14-Apr-2021	491.98 Wh	YES
15-Apr-2021	492.16 Wh	YES
16-Apr-2021	492.32 Wh	YES
17-Apr-2021	492.48 Wh	YES
18-Apr-2021	492.65 Wh	YES
19-Apr-2021	492.83 Wh	YES
20-Apr-2021	493.01 Wh	YES
21-Apr-2021	492.51 Wh	YES
22-Apr-2021	492.73 Wh	YES
23-Apr-2021	492.94 Wh	YES
24-Apr-2021	493.16 Wh	YES
25-Apr-2021	492.70 Wh	YES
26-Apr-2021	492.94 Wh	YES
27-Apr-2021	493.23 Wh	YES
28-Apr-2021	492.80 Wh	YES
29-Apr-2021	493.09 Wh	YES
30-Apr-2021	493.40 Wh	YES

```
*****
```

Listing 3.4: Output of the MATLAB simulation in appendix C.1 regarding the daily energy yield of the PV generator for the mission inputs in the table 3.20.

Results

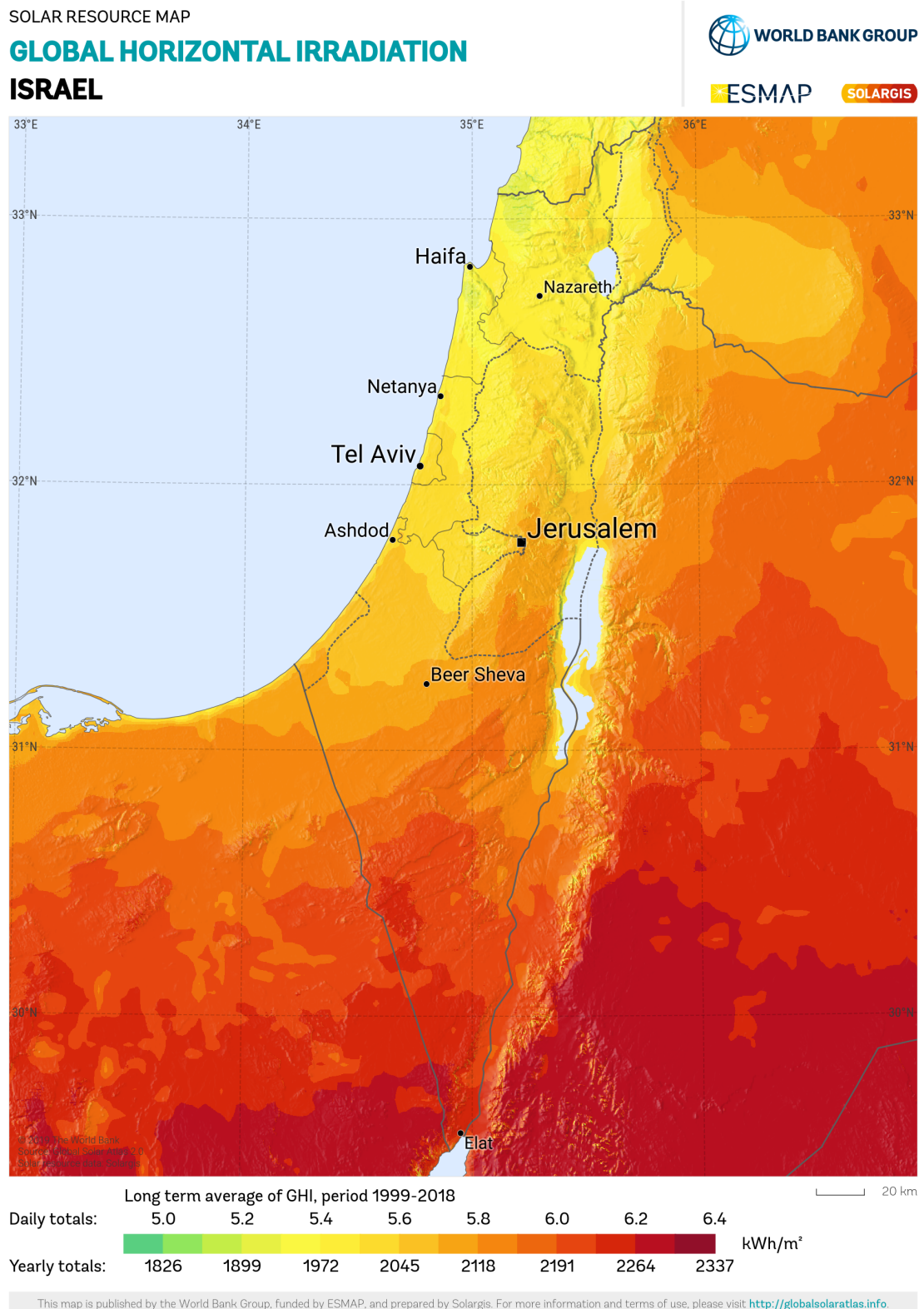


Figure 3.23: Solar resource map of the long term average global horizontal irradiation of Israel. (Image credit: [28], [34])

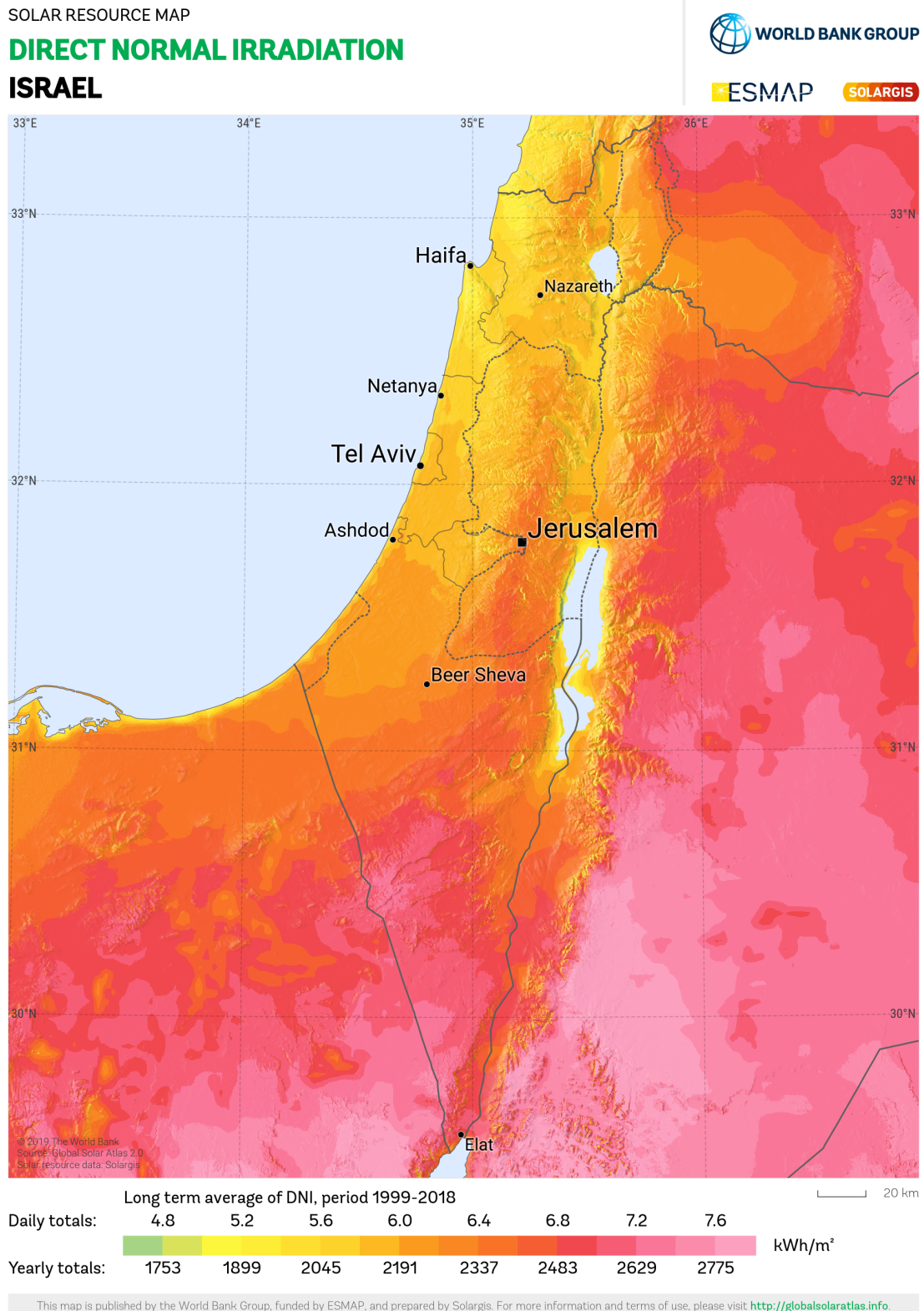


Figure 3.24: Solar resource map of the long term average direct normal irradiation of Israel. (Image credit: [28], [34])

4 Conclusion and critical reflection

In addition to the summary and conclusion of the results, a critical examination of this thesis is presented in the following sections.

4.1 Conclusion

In this section the findings and results of this thesis are summarized and concluded. First the results of the designed voice communication system are presented, followed by the self-sufficient energy distribution system and finally the usability of the system on Mars is discussed.

4.1.1 Voice communication system

It was shown that a voice communication system can be designed according to requirements of the OeWF and that a performance estimation can be carried out on it. The designed voice communication system consists of a base station radio infrastructure, a radio system for the Serenity spacesuit simulator and a repeater radio infrastructure which is used to increase the covered mission area. It furthermore consists of handheld radios used by the the on-site support crew and the safety officers.

Both the Motorola Mototrbo DP 3601 handheld VHF radios and the existing frequency license for 158,950MHz, owned by the OeWF, were reused. In addition to the existing infrastructure, further Motorola Mototrbo radios were procured, with which an infrastructure was designed so that a theoretical mission area with a diameter of 15km can be covered.

The model for plane earth signal budget was calculated for two cases to show that the fade margins of the voice communication system do not fall below a minimum value of 20dB. In the first case it was assumed that all designed radio systems in the voice communication system were transmitting with maximum transmission power and the second case took into account the limitation of the transmission power to a maximum of 5W. In both cases the minimum fade margin resulted in 21,595dB.

With regard to the Serenity spacesuit simulator, a place for the Serenity radio system in the HUT of the spacesuit simulator was found in such a way that its antenna is installed vertically at a height of 1,65m above the ground for a standard male AA, or at a height of 1,55m above the ground for a standard female AA. The radio system is installed in such a way that it can be recharged in this position and removed if necessary. An approach with a wired PTT button and a wireless Bluetooth headset was chosen to reduce the cabling effort. This also has the advantage that an AA can put on the headset before donning and simply step into the

spacesuit simulator. The same applies to doffing.

The requirement for the operating temperature of the Serenity radio system could not be fully demonstrated. The data sheet of the radio device, the PTT button, the cables and the connections involved show that they meet this requirement. However, no specifications could be found for the Bluetooth headset and the audio jack that connects the PTT button to the radio device. No experiments were carried out either. In order to show that these components meet the temperature requirement, further experiments must be carried out. Alternatively, a Bluetooth headset was presented which fulfills this requirement and is compatible with the radio system. Furthermore, an audio jack that meets this requirement can be requested directly from Motorola Solutions inc.

Since the W-LAN based voice communication system has not yet been fully developed, no qualitative statement can be made regarding the requirement for the combined mass of the two radio systems. Their combined mass is currently 853,33g with the proposed Bluetooth headset and 866,33g with an alternative Bluetooth headset.

4.1.2 Self-sufficient energy distribution system

Because the repeater radio system cannot be recharged as easy due to its remote location in the field, an environmentally friendly self-sufficient energy distribution system was designed to supply it with electrical energy. In general it consists of one or more PV generators connected in parallel, a solar charging controller and a LiFePO₄ battery. A **MATLAB** simulation was developed which provides an estimation of whether the self-sufficient energy distribution system can supply the repeater radio infrastructure with enough electrical energy at a given mission location or not. This simulation is based on models of the angular relationships between the Sun and Earth, photovoltaic generators and LiFePO₄ batteries. To obtain a model from the latter, discharging and charging experiments were carried out.

MATLAB simulations of the self-sufficient energy distribution system for the upcoming analog Mars field mission AMADEE-20 in October 2021 in the Negev Desert in Israel showed that the repeater radio system can be sufficiently supplied with electrical energy from one PV generator. Similar results could be obtained for Vienna, Austria, in April 2021. It was shown, however, that at least two PV generators in parallel are required.

4.1.3 Martian application

When examining the self-sufficient energy distribution system, two components of the system emerged which required special attention. First, the PV generator, as it requires a larger energy converting area due to the lower solar radiation on Mars, and second, the LiFePO₄ battery due to its temperature dependence. An equation was derived which compares the area ratio between a PV generator on Earth and one on Mars. However, this should only be used as a rough estimation, since the temperature dependence of said generator on the surface of Mars has to be investigated more closely. Taking into account dust storms, it was found that during such storms, due to the diffuse component of sunlight, still enough electrical energy can be converted. However, dust that accumulates on the PV generator's

energy converting area can become a problem in the long term. Regarding LiFePO₄ batteries, it was found that these have a high temperature dependence and therefore have to be heated or cooled accordingly. For this, a higher energy consumption must be planned.

After examining the voice communication system, it was found that the temperature of the radio devices and components has an influence on their thermal noise. Similar to the self-sufficient energy system, the temperature dependence also needs to be examined in more detail here. So that a reliable voice communication system can be set up on the surface of Mars, it is advisable to carry out a more detailed investigation of the multipath propagation of the electromagnetic waves, so that the infrastructure can be optimally placed. During the day, the Martian ionosphere can be used as a reflector for global communication for frequencies in the VHF range. At night, however, this effect is limited because Mars has almost no intrinsic magnetic field. This effect therefore depends heavily on the time of the day. It is assumed that the Martian troposphere has no influence on the propagation of electromagnetic waves, as it is very thin. The impact of dust storms needs further investigation. However, it is assumed that the signal attenuation for the VHF band is rather low. Finally, sufficient redundancy must be ensured so that a failure of the voice communication system is very unlikely, as this can become dangerous for astronauts.

4.2 Critical refelction

A critical reflection of this thesis is now presented to point out the areas in which further studies need to be carried out. First the voice communication system will be examined and then the self-sufficient energy distribution system.

4.2.1 Voice communication system

As already mentioned, a number of factors that influence the performance of the designed voice communication system were neglected. In the literature [2] it is explained that special consideration should be given to the temperature of the individual radio devices and components in order to investigate their thermal noise. Independent of this noise source, this literature also deals with other noise sources that could have an influence on the system. Furthermore, a more detailed examination of the signal budget should be carried out in order to take into account possible obstacles in the path of the electromagnetic waves. This includes, for instance, ground roughness. The basis for this can be found in books [5], [7]. For a Martian application this topic is covered in the NASA publication [19]. Subsequently, a simulation with topological maps for different mission locations can be carried out. Finally, the influence of the Earth's atmosphere on the propagation of electromagnetic waves should be taken into account [2], [5]. In order to obtain empirical data to get a better model of the voice communication system for simulations, experiments need to be carried out with the assembled voice communication system in different locations [8].

4.2.2 Self-sufficient energy distribution system

Instead of the approximated equations for the angular relationships between the Sun and Earth, databases can be used which contain measured values of these angles throughout the year. Thus, the accuracy of the **MATLAB** simulation can be improved. In addition, instead of the Gaussian fitting function – which was used to simulate the radiation flux Φ_G – a more precise curve shape as shown in [30] can be used.

Regarding the PV generator, the *two diodes model* can be used to improve the accuracy of the **MATLAB** simulation as well. This model is much more accurate because it takes into account the parallel resistance, the series resistance and the leakage currents of a PV cell. However, in order to obtain the necessary parameters for this model, various experiments must be carried out on a PV generator [11], [13]. Furthermore, the effect of shade on the PV generator's energy converting area must be investigated, as well as its power output for different weather conditions [11].

To further increase the accuracy of the **MATLAB** simulation, a temperature model [55], [57], [59], a capacity fading model [60] and the transient (dynamic) behavior, which is described by the Thevenin model [60]–[62], [64], [65], [67], [69], of the LiFePO₄ battery should be considered.

Finally, the **MATLAB** simulation can be sped up by reducing the amount of `for` loops and by removing possible bugs. Improvements of its accuracy can also be achieved by implementing the described step function of the load current and the charging behavior of the LiFePO₄ battery.

A Austrian Space Forum

Since 1999, the Austrian Space Forum continuously motivates dedicated space pioneers to participate in humanity's mission to explore the vast universe and fuels their passion for adventure and exploration. A quotation which is written on a wall in the OeWF Suit-laboratory in Innsbruck, Austria, wonderfully depicts what this means and what the OeWF stands for:

"I am the power that proudly looks beyond the horizon, surpassing limits and expectations.

Honoring Europe's tradition of exploration with a new glow, I am the extraordinary union of engineering excellence, scientific curiosity and the people's passion for seeking new worlds, with every step carefully drafted with diligence, emotion and elegant design.

I am the magnet that attracts talent and hearts; the maker that symbolizes Europe's ambition to set sail for the unknown.

More than just a mission in time, I define missions for generations to come.

I am the Austrian Space Forum."

A.1 History

As part of the PolAres program, which originated in 2007 after an international collaboration, the first spacesuit simulator called Aouda was developed. Its goal is to help humanity gain more knowledge and experience for future Mars missions by conducting simulations on Earth [91]. Such simulations are possible because certain regions on Earth, like the Atacama Desert in South America, the Mojave Desert in North America, the Qaidam Basin in the Tibetan Plateau or the Turpan Desert in China, have at least one feature that resembles a Martian environment [92]–[94]. Due to this analogy, these regions are often referred to as analog Martian environments. Astronauts that conduct missions in these areas are referred to as analog astronauts. As an example, figure A.1 shows the geological Mars analogy between the elongated crater "Spirit of St. Louis" on Mars (figure A.1a) and the Dhofar Desert in Oman (figure A.1b) [95]. Areas like these provide a great opportunity for scientist, engineers and analog astronauts to study possible Martian environments.



(a) Elongated crater “Spirit of St. Louis” on Mars taken from the panoramic camera on NASA’s Mars Exploration Rover Opportunity. (Image credit: [95])



(b) Two analog astronauts from the OeWF performing a simulation with Aouda spacesuit simulators in the Dhofar Desert in Oman. (Image credit: OeWF/Florian Voggeneder)

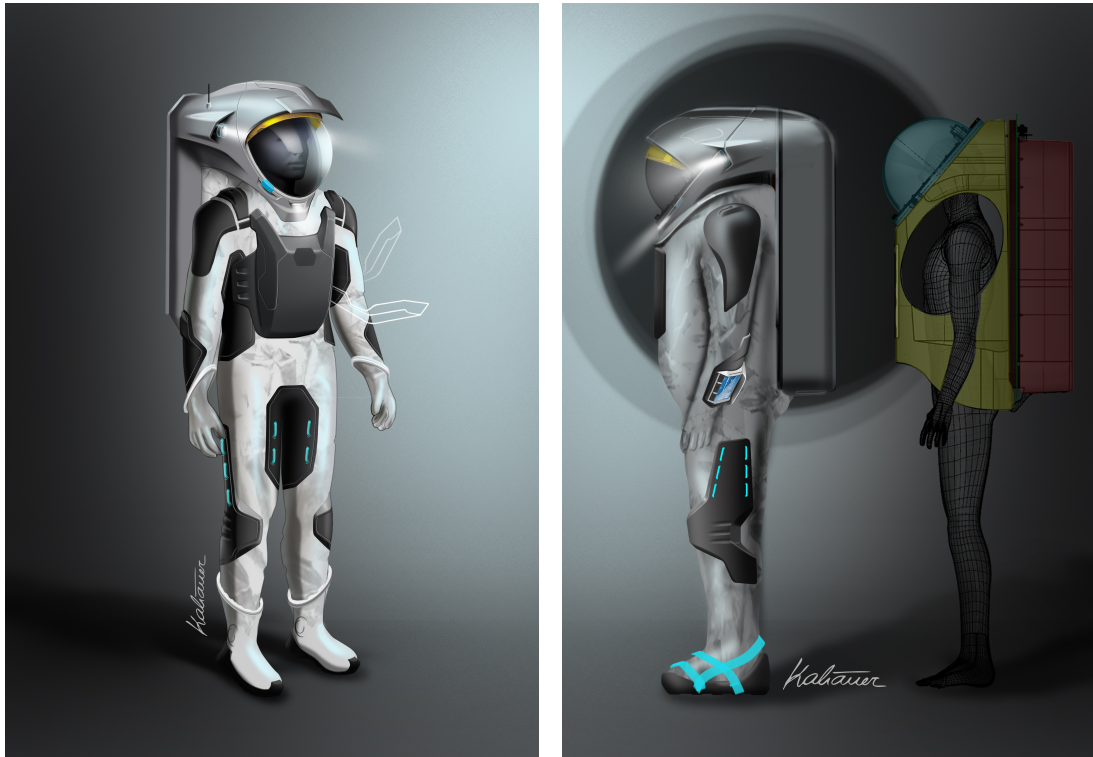
Figure A.1: Visible geological similarities between the Martian surface and an analog Martian environment on Earth.

With the help of Aouda, analog astronauts can conduct basic training, experiments and other important tasks while experiencing similar restrictions and technical aids a Mars spacesuit in two to three decades will have. This makes it possible to collect vital data from different scientific areas, which can help future astronauts to safely prepare for Mars missions [91].

In 2010, the Aouda spacesuit simulator was tested for the first time in a field simulation on a glacier in the Kaunertal in Austria. The mission lasted for two days and aimed to perform astrobiological experiments. Further missions took place in 2011 in Rio Tinto in Spain, in 2012 on the Dachstein mountains in Austria, in 2013 in the northern Sahara near Erfoud in Morocco (MARS2013), in 2015 again in the Kaunertal in Austria (AMADEE-15) and in 2018 in the Dhofar Desert in Oman (AMADEE-18). The next mission, called AMADEE-20, was planned to take place in late 2020 in the Negev Desert in Israel but it was postponed until October 2021 due to the ongoing SARS-CoV-2 pandemic. Missions carried out by the OeWF generally last from a couple of days to a few months [96], [97].

A.2 Serenity spacesuit simulator

After ten years and more than 750 hours of *extravehicular activities* (EVAs), Aouda's successor is the Serenity spacesuit simulator. In participation with national and international high-end universities and companies, Serenity has been under development since 2018. Bernhard Kaliauer Design Studio's first concept of Serenity is shown in figure the A.2.



(a) Front view

(b) Side view

Figure A.2: Serenity spacesuit simulator design study. (Image credit: OeWF/Bernhard Kaliauer Design Studio)

It is important to the OeWF to make the transition from Aouda to Serenity as fluid and environmentally friendly as possible. That is why, on the one hand, tried and tested materials are being upgraded and re-used, which shortens the retraining time of the analog astronauts, and on the other hand, a number of innovations are introduced based on the knowledge gathered over the past few years.

Apart from the complete revision to carry out even more realistic simulations, a new advanced rear-entry system will be implemented. This system represents the latest NASA standard for Mars missions due to its ability to easily dock at a habitat, thus reducing contamination and donning time [98].

B Mathematical basics

This appendix covers the most important mathematical basics that were used. More information can be found in the books [50]–[53], [99].

B.1 Integral of the Gaussian bell curve

The shifted Gaussian bell function, shown in the figure B.1, is used to model the solar energy curve (see subsection 2.3.5). Therefore, the mathematical approach of calculating the area of the Gaussian bell function – enclosed by the curve and the x-axis – will be explained.

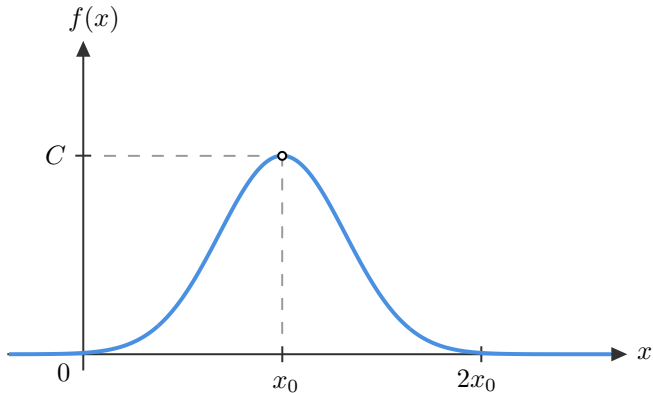


Figure B.1: Shifted Gauss bell.

In general, the Gaussian bell function can be written as shown in the equation (B.1), with its corresponding indefinite Integral shown in the equation (B.2).

$$f(x) = C \exp\left(-\frac{(x - x_0)^2}{a}\right) \quad (\text{B.1})$$

$$F(x) = C \int_{-\infty}^{\infty} \exp\left(-\frac{(x - x_0)^2}{a}\right) dx \quad (\text{B.2})$$

Since the integral in the equation (B.2) cannot be solved, an approach is used in which the integral is squared. How this works is presented in the following steps.

$$\begin{aligned}
 F(x)^2 &= C^2 \left(\int_{-\infty}^{\infty} \exp\left(-\frac{(x-x_0)^2}{a}\right) dx \right)^2 \\
 &= C^2 \int_{-\infty}^{\infty} \exp\left(-\frac{(u-u_0)^2}{a}\right) du \int_{-\infty}^{\infty} \exp\left(-\frac{(v-v_0)^2}{a}\right) dv \\
 &= C^2 \int_{-\infty}^{\infty} \int_{-\infty}^{\infty} \exp\left(-\frac{(u-u_0)^2}{a}\right) \exp\left(-\frac{(v-v_0)^2}{a}\right) du \cdot dv \\
 &= C^2 \int_{-\infty}^{\infty} \int_{-\infty}^{\infty} \exp\left(-\frac{(u-u_0)^2 + (v-v_0)^2}{a}\right) du \cdot dv
 \end{aligned} \tag{B.3}$$

If now $x = u - u_0$ and $y = v - v_0$ are substituted in the last step of the equation (B.3), the double integral can be written as presented in the equation (B.8). Due to these substitutions, the equations (B.4) to (B.6) have to be considered.

$$dx = du, dy = dv \tag{B.4}$$

$$\lim_{u \rightarrow \infty} x = \infty, \quad \lim_{u \rightarrow -\infty} x = -\infty \tag{B.5}$$

$$\lim_{v \rightarrow \infty} y = \infty, \quad \lim_{v \rightarrow -\infty} y = -\infty \tag{B.6}$$

By using the expressions from the equation (B.7), the double integral in the equation (B.8) can be transformed into polar coordinates.

$$x^2 + y^2 = r^2, \quad dx dy = r dr d\phi \tag{B.7}$$

$$\begin{aligned}
 F(x)^2 &= C^2 \int_{-\infty}^{\infty} \int_{-\infty}^{\infty} \exp\left(-\frac{x^2 + y^2}{a}\right) dx \cdot dy \\
 &= C^2 \int_0^{2\pi} \int_0^{\infty} \exp\left(-\frac{r^2}{a}\right) r dr \cdot d\phi
 \end{aligned} \tag{B.8}$$

With a final substitution of $w = -\frac{r^2}{a}$, from which the equations (B.9) and (B.10) derive, the double integral can be solved as shown in the equation (B.11).

$$r dr = -\frac{a}{2} du \tag{B.9}$$

$$\lim_{r \rightarrow \infty} w = -\infty, \lim_{r \rightarrow 0} w = 0 \quad (\text{B.10})$$

$$F(x)^2 = -\frac{a C^2}{2} \int_0^{2\pi} \underbrace{\int_0^{-\infty} e^w dw}_{-1} \cdot d\phi = \frac{a C^2}{2} \int_0^{2\pi} 1 d\phi = a C^2 \pi \quad (\text{B.11})$$

The result of the indefinite integral of the Gaussian bell function must therefore be:

$$F(x) = C\sqrt{a\pi}. \quad (\text{B.12})$$

It is positive because the area enclosed by the curve and the x-axis cannot be negative.

B.2 Newton-Raphson method

The zero crossing $x = x_R$ of a function $f(x) : \mathbb{R} \rightarrow \mathbb{R}$, for which $f(x_R) = 0$ applies, can be approximated with the Newton-Raphson method as shown in the equation B.13.

$$\begin{aligned} x_1 &= x_0 - \frac{f(x_0)}{f'(x_0)} \\ x_2 &= x_1 - \frac{f(x_1)}{f'(x_1)} \\ &\vdots \\ x_{n+1} &= x_n - \frac{f(x_n)}{f'(x_n)} \end{aligned} \quad (\text{B.13})$$

This algorithm can be derived by using the figure B.2, whereby the requirement must be met that the function $f(x)$ is continuously differentiable for the required number of iteration steps $n + 1$ with $n \in \mathbb{N}$. The approximation quality of the zero crossing x_R can be determined with the specified precision $|x_{n+1} - x_n| < \varepsilon$. In order for the algorithm to converge towards the zero crossing, the start value x_0 must be found accordingly.

Based on the previous findings, the elements of the vector of zero crossings $\mathbf{x} = \mathbf{x}_R$ of the vector of functions $\mathbf{f}(\mathbf{x}) : \mathbb{R}^m \rightarrow \mathbb{R}^m$ with $m \in \mathbb{N}$, for which $\mathbf{f}(\mathbf{x}_R) = \mathbf{0}$ applies, can be approximated as shown below.

$$\mathbf{x}_{R,n+1} = \mathbf{x}_{R,n} - \mathbf{J}^{-1}(\mathbf{x}_{R,n}) \mathbf{f}(\mathbf{x}_{R,n}) \quad (\text{B.14})$$

The Jacobian matrix \mathbf{J} contains all partial derivatives of the function vector with respect to the vector of the zero crossings.

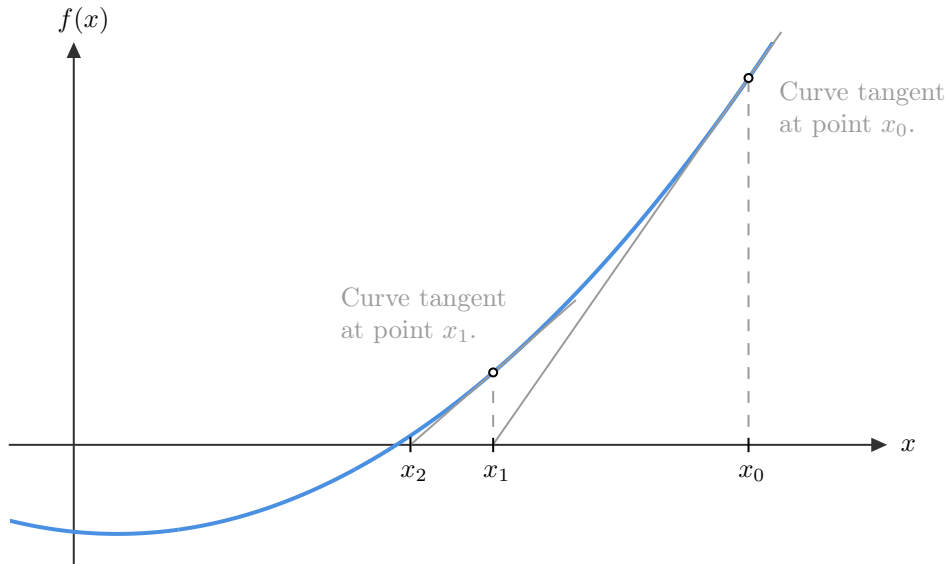


Figure B.2: Newton-Raphson method to approximate the zero crossing of a function.

$$\mathbf{J} = \left. \frac{\partial \mathbf{f}(\mathbf{x})}{\partial \mathbf{x}} \right|_{\mathbf{x}=\mathbf{x}_R} = \begin{pmatrix} \frac{\partial}{\partial x_1} f_1(\mathbf{x}_R) & \frac{\partial}{\partial x_2} f_1(\mathbf{x}_R) & \cdots & \frac{\partial}{\partial x_m} f_1(\mathbf{x}_R) \\ \frac{\partial}{\partial x_1} f_2(\mathbf{x}_R) & \frac{\partial}{\partial x_2} f_2(\mathbf{x}_R) & \cdots & \frac{\partial}{\partial x_m} f_2(\mathbf{x}_R) \\ \vdots & \vdots & \ddots & \vdots \\ \frac{\partial}{\partial x_1} f_m(\mathbf{x}_R) & \frac{\partial}{\partial x_2} f_m(\mathbf{x}_R) & \cdots & \frac{\partial}{\partial x_m} f_m(\mathbf{x}_R) \end{pmatrix} \quad (\text{B.15})$$

For completeness it is noted that $\mathbf{x}_R = (x_1, \dots, x_m)^T$ does not correspond to the figure B.2. The elements x_1 to x_m of the vector \mathbf{x}_R are zero crossings of the functions contained by the vector $\mathbf{f}(\mathbf{x}_R) = (f_1(\mathbf{x}_R), \dots, f_m(\mathbf{x}_R))^T = \mathbf{0}$. Their $(n+1)^{\text{th}}$ approximation is $\mathbf{x}_{R,n+1} = (x_{1,n+1}, \dots, x_{m,n+1})^T$.

C MATLAB and MAPLE source codes

This appendix contains the **MATLAB** simulation which was used to simulate the self-sufficient energy distribution system and the **MAPLE** source code which was used to calculate the Jacobian matrix in the subsection 2.3.6.

C.1 MATLAB simulation of the self-sufficient energy distribution system

```
1 %% MAIN: Self-sufficient energy distribution system performance ...
2 % estimation
3 % This simulation provides a performance estimation of the ...
4 % self-sufficient energy distribution system, which is part of ...
5 % the voice communication system of the OeWF Serenity spacesuit ...
6 % simulator. It can be simulated if the repeater radio ...
7 % infrastructure can operate at a certain mission location on ...
8 % Earth. All sections labeled [INPUT] can be manipulated. For ...
9 % further information please refer to the MATLAB documentation, ...
10 % look into the bachelor thesis about this simulation or contact ...
11 % the author.
12
13
14 % Organization:      OeWF (Austrian Space Forum)
15 % Author:            Omar Filip El Sendiouny
16 % Project:           Serenity BU-COMMs
17 % Date:              15.12.2020
18 % Version:           1
19
20
21 clear all;
22 close all;
23 clc;
24
25
26 show_command_window_output = 1; % allow command window output
27 N_dp = 4; % number of decimal points for solar angle calculations ...
28 % (accuracy)
29
30
31 dfile ='command_window_output.txt'; % command window output can be ...
32 % found in the local folder
33 if(exist(dfile, 'file'))
34     delete(dfile);
35 end
36 diary(dfile)
37 diary on
38
39
40 %% [INPUT] Mission information:
```

```

25 % It is assumed that the missions start at the same time every day ...
   for the entire duration of the mission. The time of the mission ...
   start must be smaller than the time of mission end.
26
27 lat = 30.500; % latitude in (deg)
28 lon = 35.917; % longitude in (deg)
29 irradiation_GH = 6.05; % daily total of the global horizontal ...
   irradiation in (kWh / m^2)
30 irradiation_DN = 6.85; % daily total of the direct normal ...
   irradiation in (kWh / m^2)
31 date(1) = datetime(2021, 10, 4); % mission start date in (Y, M, D)
32 date(2) = datetime(2021, 10, 31); % mission end date in (Y, M, D)
33 t_UTC(1) = {'4:00'}; % time of the daily mission start in (h)
34 t_UTC(2) = {'14:00'}; % time of the daily mission end in (h)
35 ALB = 0.30; % albedo in (1)
36 theta_A = 22.3; % average ambient temperature in (degrees C)
37
38 %% [INPUT] Photovoltaic generator:
39 % MPP ... maximim power point
40 % STC ... standard test conditions
41 % SC ... short-circuit
42 % OC ... open-circuit
43
44 N_C = 36; % number of PV cells in (1)
45 A_PV = 0.88; % PV generator area in (m^2)
46 I_MPP_STC = 9.11; % current at MPP for STC in (A)
47 U_MPP_STC = 21.41; % voltage at MPP for STC in (V)
48 I_SC_STC = 9.79; % SC current for STC in (A)
49 U_OC_STC = 24.27; % OC voltage for STC in (V)
50 TC_I_SC = 0.05; % temperature coefficient for I_SC in (% / degC)
51 TC_U_OC = -0.29; % temperature coefficient for U_OC in (% / degC)
52 NOCT = 45; % nominal operating cell temperature in (degC)
53 m = 1.19045; % ideality factor in (1)
54 N_PV = 1; % number of PV generators (if greater than 1, they are ...
   connected in parallel)
55
56 %% [INPUT] Load (repeater radio system):
57 % After t_UTC(2) and before t_UTC(1) the repeater radio system is ...
   in standby. The sum of the duty cycles must be 100%.
58
59 U_L_min = 11.0; % minimum load voltage in (V)
60 U_L_max = 15.5; % maximum load voltage in (V)
61 I_T = 3; % current consumption when the load transmits in (A)
62 I_R = 0.7; % current consumption when the load receives in (A)
63 I_Stby = 0.7; % current consumption when the load is in standby in (A)
64 a_T = 20; % duty cycle when transmitting in (%)
65 a_R = 20; % duty cycle when receiving in (%)
66 a_Stby = 60; % duty cycle when in standby in (%)
67 I_add = 0; % additional load current in (A)
68
69 %% [INPUT] LiFePo_4 battery
70 % The initial state of charge of the battery is usually the SOC for ...
   storage, which is between 50% and 60%.
71
72 SOC_init = 0.6; % initial state of charge in (1)
73 Q_nom = 50; % nominal charge in (Ah)
74 C_D = 1/3; % discharging rate for Q_nom in (h^(-1))
75

```

```
76 % Obtained from the discharging and charging experiments:
77 SOC = [1.00 0.95 0.90 0.85 0.80 0.75 0.70 0.65 0.60 0.55 0.50 0.45 ...
    0.40 0.35 0.30 0.25 0.20 0.15 0.10 0.05 0.00]; % state of ...
    charge in (1) of the battery
78 U_0_D = [13.877 13.315 13.319 13.322 13.320 13.306 13.248 13.196 ...
    13.181 13.117 13.174 13.172 13.169 13.111 13.087 13.012 12.931 ...
    12.837 12.814 12.350 11.371]; % open-circuit voltages when ...
    discharging the battery in (V)
79 U_0_C = [14.107 13.387 13.393 13.401 13.415 13.388 13.387 13.275 ...
    13.272 13.253 13.250 13.248 13.250 13.244 13.225 13.179 13.089 ...
    12.958 12.923 12.502 11.420]; % open-circuit voltages when ...
    charging the battery in (V)
80 R_e_D = [0.0120840740086789 0.0117154203104446 0.0117700588020157 ...
    0.0117132299485587 0.0116221338950336 0.0116467701188540 ...
    0.0116605558931997 0.0115638462618863 0.0116222251883952 ...
    0.0116974390402753 0.0116987272047564 0.0117465274490441 ...
    0.0117588908671468 0.0117566064015986 0.0117756658545291 ...
    0.0117553658832641 0.0117583775845481 0.0117768748688630 ...
    0.0117155094645921 0.0118414656950463 0.0120957986167104]; % ...
    electrolyte resistances when discharging in (Ohm)
81 R_e_C = [0.0121012406947893 0.0113356302935661 0.0114597641410590 ...
    0.0114014839745851 0.0114900762492556 0.0116012192457450 ...
    0.0112273867826839 0.0112396239841211 0.0111117629249463 ...
    0.0112231518757464 0.0113202903133204 0.0112805170265242 ...
    0.0114125559543423 0.0114503161497776 0.0114125257730806 ...
    0.0115293500897879 0.0115664251765242 0.0115250208156497 ...
    0.0117012683150631 0.0118226401014494 0.0120662511263975]; % ...
    electrolyte resistances when charging in (Ohm)
82
83 %% [INPUT] Solar charging controller
84 % The SCC only connects the PV generator when its voltage at the PV ...
    generator input terminal exceeds U_Bat + 5V. As soon as this ...
    condition is met the PV generator remains connected as long as ...
    the voltage at the PV generator input terminal is greater than ...
    U_Bat + 1V.
85
86 I_SCC = 0.020; % current consumption of the SCC in (A)
87 I_B_max = 10; % maximum battery current in (A)
88 P_MPP_max = 145; % maximum power from PV generator in (W)
89 eta_SCC = 0.98; % efficiency in (1)
90
91 %% [INPUT] Cables:
92 % Only one wire of the cable is to be described. For more ...
    information, please refer to the subsection 3.1.2 (Repeater ...
    radio infrastructure) of the bachelor thesis about this simulation.
93
94 % Input style: cables = [cable_A; cable_B; cable_C]
95 % Input style: cables(n,:) = [length cross_section_area ...
    specific_resistance temperature_coefficient]
96
97 % length in (m)
98 % cross_section_area in (mm^2)
99 % specific_resistance for 20 degC in (Ohm * mm^2 / m)
100 % temperature coefficientc for 20 degC in (degC^(-1))
101
102 cables = [0.9 4.0 0.01673 4.3 * 10^(-3); 0.5 4.0 0.01673 4.3 * ...
    10^(-3); ...
    11.0 2.5 0.01673 4.3 * 10^(-3)];
```

```

104
105 %% [OUTPUT] Radiation flux received by an inclined PV generator:
106 % To ensure better readability, for-loops were used instead of ...
107 % direct assignments for most vectors/matrices. This further ...
108 % helps with the maintenance of the program. However, it ...
109 % decreases the performance of the simulation (fix in version 1.1)
110
111 lat = round(lat, N_dp);
112 lon = round(lon, N_dp);
113
114 date_array = (date(1):date(2))'; % contains all mission dates
115 N_md = split(between(date(1), date(2), 'days'), 'days') + 1; % ...
116 % number of mission days
117
118 delta_t_S = 0.01; % resolution for solar time
119 N_dp_delta_t_S = 0; % number of decimal places of delta_t_S
120
121 while (floor(delta_t_S * 10^N_dp_delta_t_S) ≠ delta_t_S * 10^N_dp_delta_t_S) % find ...
122 % the number of decimal places of delta_t_S
123 N_dp_delta_t_S = N_dp_delta_t_S + 1;
124 end
125
126 t_S = round(0:delta_t_S:24, N_dp_delta_t_S); % solar time
127 h_S = round((t_S - 12) * 15, N_dp); % solar hour angle
128
129 N_d = zeros(N_md, 1); % number of days since Jan. 1st
130 delta = zeros(N_md, 1); % Sun declination
131 beta = zeros(N_md, 1); % optimal inclination angle for the PV generator
132 h_rs = zeros(N_md, 2); % solar sunrise and sunset hour angles
133
134 for n = 1:N_md % calculating N_d, delta, and beta
135     N_d(n) = 30.3 * (month(date_array(n)) - 1) + day(date_array(n));
136     delta(n) = round(23.45 * sind((360 * (284 + N_d(n)) / 365)), N_dp);
137     beta(n) = round(abs(lat - delta(n)), N_dp);
138 end
139
140 beta_mean = mean(beta); % mean value of beta will be used from now on
141
142 for n = 1:N_md % calculating h_rs
143     if(abs(lat) < 90 - abs(delta(n)))
144         h_rs(n,1) = round(-acosd(-tand(delta(n)) * tand(lat)), N_dp); ...
145             % solar sunrise hour angle
146         h_rs(n,2) = round(-h_rs(n,1), N_dp); % solar sunset hour angle
147     else
148         error('Solar sunrise and sunset angles cannot not be ...
149             calculated!');
150     end
151 end
152
153 t_rs = 12 + h_rs / 15; % solar sunrise and sunrise times
154
155 idx = h_S ≤ 0; % get index for solar hour angles from t_S = 0h to ...
156 % t_S = 12h
157 h_S_fhd = h_S(idx); % create associated vector for solar hour ...
158 % angles (first half of the day)
159
160 gamma_S = zeros(N_md, length(h_S_fhd)); % altitude of the Sun
161 alpha_S = zeros(N_md, length(h_S_fhd)); % azimuth of the Sun

```

```
153 theta = zeros(N_md, length(h_S_fhd)); % angle theta (solar ...
    incidence angle)
154
155 for n = 1:N_md % calculating gamma_S_deg from sunrise to t_S = 12h
156     for o = 1:length(h_S_fhd)
157         if(h_S_fhd(o) ≥ h_rs(n,1)) % if the Sun is above the horizon
158             gamma_S(n,o) = round(asind(sind(lat) * sind(Δ(n)) + ...
159             cosd(lat) * cosd(Δ(n)) * cosd(h_S_fhd(o))), N_dp);
160         else
161             gamma_S(n,o) = NaN; % invalid angle (Sun is below the ...
                horizon)
162         end
163     end
164
165 for n = 1:N_md % calculating alpha_S_deg from sunrise to t_S = 12h
166     for o = 1:length(h_S_fhd)
167         if(h_S_fhd(o) ≥ h_rs(n,1) && h_S_fhd(o) ≠ 0) % if the Sun ...
            is above the horizon before t_S = 12h
168             alpha_S(n,o) = round(-acosd((sind(lat) * cosd(Δ(n)) * ...
            cosd(h_S_fhd(o)) - cosd(lat) * sind(Δ(n))) / ...
            cosd(gamma_S(n,o))), N_dp);
169         elseif(h_S_fhd(o) == 0 && gamma_S(n,o) ≠ 90) % if t_S = 12h ...
            and the Sun is not at its zenith
170             if(lat > Δ(n))
171                 alpha_S(n,o) = round(0, N_dp);
172             elseif(lat < Δ(n))
173                 alpha_S(n,o) = round(180, N_dp);
174             end
175         else % the Sun is below the horizon or at its zenith
176             alpha_S(n,o) = NaN; % invalid angle
177         end
178     end
179 end
180
181 for n = 1:N_md % calculating theta
182     for o = 1:length(h_S_fhd)
183         if(h_S_fhd(o) ≥ h_rs(n,1)) % if the Sun is above the horizon
184             if(gamma_S(n,t_S == 12) ≠ 90) % if the Sun is not at ...
                its zenith
185                 tmp = sind(Δ(n)) * sind(lat) * cosd(beta_mean) ...
186                     - sind(Δ(n)) * cosd(lat) * sind(beta_mean) * ...
187                         cosd(alpha_S(n, t_S == 12)) ...
188                         + cosd(Δ(n)) * cosd(lat) * cosd(beta_mean) * ...
189                             cosd(h_S_fhd(o)) ...
190                             + cosd(Δ(n)) * sind(lat) * sind(beta_mean) * ...
191                                 cosd(alpha_S(n,o)) * cosd(h_S_fhd(o)) ...
192                                 + cosd(Δ(n)) * sind(beta_mean) * ...
193                                     sind(alpha_S(n, t_S == 12)) * cosd(h_S_fhd(o));
194             if(tmp>1) % necessary because of rounding errors ...
                caused by matlab
195                 tmp = 1;
196             end
197             theta(n,o) = round((acosd(tmp)), N_dp);
198         elseif(gamma_S(n,t_S == 12) == 90) % if the Sun is at ...
                its zenith
199             tmp = sind(Δ(n)) * sind(lat) ...
200                 + cosd(Δ(n)) * cosd(lat) * cosd(h_S_fhd(o));
```

```

197         theta(n,o) = round(acosd(tmp), N_dp);
198     end
199 else
200     theta(n,o) = NaN; % invalid angle
201 end
202 end
203 end
204
205 for n = 1:N_md % because of the projection of the normal to A_PV ...
206     onto plane earth?
207     [~, idx(n)] = max(theta(n,:));
208     for o = 1:length(theta)
209         if(o < idx(n) || theta(n,o) ≥ 90.0) % if the Sun's rays do ...
210             not hit A_PV
211             theta(n,o) = NaN;
212         end
213     end
214 end
215 tmp_mat = gamma_S;
216 tmp_mat = fliplr(tmp_mat); % flip the temporary matrix from left to ...
217     right
218 tmp_mat(:,1) = []; % delete first entry so it does not appear twice ...
219     in the gamma_S matrix
220 gamma_S = [gamma_S tmp_mat]; % allowed because the Sun is ...
221     symmetrical around t_S = 12h
222
223 tmp_mat = alpha_S;
224 tmp_mat = fliplr(tmp_mat); % flip the temporary matrix from left to ...
225     right
226 tmp_mat(:,1) = []; % delete first entry so it does not appear twice ...
227     in the alpha_S matrix
228 alpha_S = [alpha_S -tmp_mat]; % allowed because the Sun is ...
229     symmetrical around t_S = 12h
230
231 tmp_mat = theta;
232 tmp_mat = fliplr(tmp_mat); % flip the temporary matrix from left to ...
233     right
234 tmp_mat(:,1) = []; % delete first entry so it does not appear twice ...
235     in the theta matrix
236 theta = [theta tmp_mat]; % allowed because the Sun is symmetrical ...
237     around t_S = 12h
238
239 E_GHI = irradiation_GH * 10^(3) / 24; % global horizontal irradiance
240 E_DNI = irradiation_DN * 10^(3) / 24; % direct normal irradiance
241
242 E_G = zeros(N_md, length(t_S)); % total irradiance received by an ...
243     inclined PV generator
244 W_G = zeros(N_md, 1); % solar energy yield
245 tau_S = zeros(N_md, 1); % auxiliary variable
246 Phi_max = zeros(N_md, 1); % maximal daily radiation flux
247 Phi_G = zeros(N_md, length(t_S)); % radiation flux received by an ...
248     inclined PV generator
249
250 for n = 1:N_md % calculating E_G
251     for o = 1:length(t_S)
252         if(isnan(theta(n,o)) && ~isnan(gamma_S(n,o)))

```

```
241         E_G(n,o) = (E_GHI - E_DNI * sind(gamma_S(n,o))) * (1 + ...
242             cosd(beta_mean)) / 2; % PV generator receives DIFG
243     elseif (~isnan(theta(n,o)) && ~isnan(gamma_S(n,o))) % PV ...
244         generator receives DGI, DIFG and RGI
245         E_G(n,o) = E_DNI * cosd(theta(n,o)) ...
246             + (E_GHI - E_DNI * sind(gamma_S(n,o))) * (1 + ...
247                 cosd(beta_mean)) / 2 ...
248             + E_GHI * ALB * (1 - cosd(beta_mean)) / 2;
249     else
250         E_G(n,o) = 0;
251     end
252 end
253
254 for n = 1:N_md % calculating W_G
255     for o = 1:length(t_S)
256         W_G(n) = W_G(n) + A_PV * E_G(n,o) * dt_S;
257     end
258 end
259
260 for n = 1:N_md % calculating Phi_G
261     for o = 1:length(t_S)
262         tau_S(n) = (12 - t_rs(n,1)) / 3;
263         Phi_max(n) = 0.997 / (tau_S(n) * sqrt(2 * pi)) * W_G(n);
264         Phi_G(n,o) = Phi_max(n) * exp(- (t_S(o) - 12)^2/(2 * ...
265             tau_S(n)^2));
266     end
267 end
268 %% [OUTPUT] PV generator power output
269
270 e = 1.602176634 * 10^(-19); % elementary charge in (As)
271 k_B = 1.380649 * 10^(-23); % Boltzmann constant in (Ws/K)
272
273 theta_C = zeros(N_md, length(t_S)); % PV cell temperature
274 U_T = zeros(N_md, length(t_S)); % thermal voltage
275 I_Ph = zeros(N_md, length(t_S)); % photocurrent
276 I_Ph_irr_STC = zeros(N_md, length(t_S)); % photocurrent with E_STC
277 U_OC_0 = zeros(N_md, length(t_S)); % open-circuit voltage
278 I_S_0 = zeros(N_md, length(t_S)); % reverse saturation current
279
280 for n = 1:N_md % calculating the parameters initialized above
281     for o = 1:length(t_S)
282         theta_C(n,o) = theta_A + (NOCT - 20) * Phi_G(n,o) * A_PV / 800;
283         U_T(n,o) = k_B * (theta_C(n,o) + 273.15)/e;
284         I_Ph(n,o) = I_SC_STC * Phi_G(n,o) * A_PV * (1 + TC_I_SC / ...
285             100 * (theta_C(n,o) - 25)) / 1000;
286         I_Ph_irr_STC(n,o) = I_SC_STC * (1 + TC_I_SC / 100 * ...
287             (theta_C(n,o) - 25));
288         U_OC_0(n,o) = U_OC_STC * (1 + TC_U_OC / 100 * (theta_C(n,o) ...
289             - 25)) ...
290             + m * N_C * U_T(n,o) * log(I_Ph(n,o) / I_Ph_irr_STC(n,o));
291
292 if (U_OC_0(n,o) < 0) % so that I_S << I_Ph is fulfilled
293     U_OC_0(n,o) = NaN;
294     I_S_0(n,o) = NaN;
295 else
```

```

291         I_S_0(n,o) = I_Ph(n,o) * exp(- (U_OC_0(n,o)) / (m * N_C ...
292                                         * U_T(n,o)));
293     end
294 end
295
296 [idxn, idxo] = find(U_OC_0 == max(max(U_OC_0))); % finding maximum ...
297 % value in U_OC_0 matrix (improve in version 1.1)
298 Δ_U_PV = 0.01; % resolution for PV generator voltage
299 U_PV = 0:Δ_U_PV:U_OC_0(idxn, idxo) + Δ_U_PV; % PV generator voltage
300 I_PV = zeros(N_md, length(t_S), length(U_PV)); % PV generator current
301 P_PV = zeros(N_md, length(t_S), length(U_PV)); % PV generator power
302 P_MPP = zeros(N_md, length(t_S)); % PV generator power for MPP
303 U_MPP = zeros(N_md, length(t_S)); % PV generator voltage for MPP
304 I_MPP = zeros(N_md, length(t_S)); % PV generator current for MPP
305 W_G_el = zeros(N_md, 1); % electrical energy yield of the PV generator
306
307 for n = 1:N_md % calculating PV generator current and MPP values ...
308 % as well as its daily electrical energy yield (3D matrix ... ...)
309 % noice UWU)
310     for o = 1:length(t_S)
311         for p = 1:length(U_PV)
312             I_PV(n,o,p) = N_PV * (I_Ph(n,o) - I_S_0(n,o) * ...
313                                         (exp(U_PV(p) / (m * N_C * U_T(n,o))) - 1));
314
315             if(I_PV(n,o,p) < 0)
316                 I_PV(n,o,p) = NaN;
317             end
318
319             P_PV(n,o,p) = I_PV(n,o,p) * U_PV(p);
320
321             if(isnan(P_PV(n,o,p)))
322                 P_PV(n,o,p) = 0;
323             end
324         end
325
326         if(isnan(I_PV(n,o, idx)))
327             I_MPP(n,o) = 0;
328         else
329             I_MPP(n,o) = I_PV(n,o, idx);
330         end
331     end
332
333 for n = 1:N_md % calculating W_G_el
334     for o = 1:length(t_S)
335         W_G_el(n) = W_G_el(n) + P_MPP(n,o) * Δ_t_S; % electrical ...
336                                         % energy yield
337     end
338
339 %% [OUTPUT] Load (repeater radio system)
340 % The load current is an average current, because an on-off step ...
341 % function could not be implemented.

```

```
342 dtv = datevec(datetime(t_UTC{1}, 'InputFormat', 'HH:mm')); % ...
    converitng time of daily mission start to floating point number
343 da = duration(dtv(:,4:end));
344 t_UTC_float(1) = hours(da);
345
346 dtv = datevec(datetime(t_UTC{2}, 'InputFormat', 'HH:mm')); % ...
    converitng time of daily mission end to floating point number
347 da = duration(dtv(:,4:end));
348 t_UTC_float(2) = hours(da);
349
350 Z_h = zeros(N_md, 1); % equation of time
351 t_S_mission_se = zeros(N_md, 2); % solar mission start and end times
352 I_L = zeros(N_md, length(t_S)); % load current
353
354 for n = 1:N_md % calculating solar mission time
355     Z_h(n) = 0.123 * cosd(360 * (88 + N_d(n)) / 365) - 0.167 * ...
        sind(720 * (10 + N_d(n)) / 365);
356     t_S_mission_se(n, 1) = round(t_UTC_float(1) + Z_h(n) + lon / ...
        15, N_dp_Δ_t_S);
357     t_S_mission_se(n, 2) = round(t_UTC_float(2) + Z_h(n) + lon / ...
        15, N_dp_Δ_t_S);
358 end
359
360 idx_mission_se = zeros(N_md, 2); % indices for daily mission start ...
    and end in t_S
361
362 for n = 1:N_md % find index of daily mission start and end in t_S
363     [~, idx_mission_se(n,1)] = find(t_S == t_S_mission_se(n,1));
364     [~, idx_mission_se(n,2)] = find(t_S == t_S_mission_se(n,2));
365 end
366
367 for n = 1:N_md % calculating I_L
368     if(n == 1)
369         for o = 1:length(t_S) % first day begins at mission start
370             if(o < idx_mission_se(n,1))
371                 I_L(n,o) = 0;
372             elseif(o ≥ idx_mission_se(n,1) && o ≤ idx_mission_se(n,2))
373                 I_L(n,o) = I_T * a_T / 100 + I_R * a_R / 100 + ...
                    I_Stby * a_Stby / 100 + I_add;
374             else
375                 I_L(n,o) = I_Stby + I_add;
376             end
377         end
378     else
379         for o = 1:length(t_S) % all other days
380             if(o ≥ idx_mission_se(n,1) && o ≤ idx_mission_se(n,2))
381                 I_L(n,o) = I_T * a_T / 100 + I_R * a_R / 100 + ...
                    I_Stby * a_Stby / 100 + I_add;
382             else
383                 I_L(n,o) = I_Stby + I_add;
384             end
385         end
386     end
387 end
388
389 %% [OUTPUT] Cables losses
390
391 sz = size(cables);
```

```

392 R_wires = zeros(sz(1),1); % wire resistances
393
394 for p = 1:sz(1) % calculate all wire resistances
395     R_wires(p) = cables(p,1) * cables(p,3) * (1 + cables(p,4) * ...
396         (theta_A - 20)) ...
397         / cables(p,2);
398 end
399 %% [OUTPUT] Solar charging controller and LiFePO_4 battery
400
401 k_P = 1.05; % Peukert constant in (1)
402 I_nom = C_D * Q_nom; % nominal battery current
403
404 U_in = zeros(N_md, length(t_S)); % voltage at PV generator input ...
405     terminal
406 U_L = zeros(N_md, length(t_S)); % voltage at repeater
407 Q_B = zeros(N_md, length(t_S)); % battery charge
408 I_B = zeros(N_md, length(t_S)); % battery current
409 U_B = zeros(N_md, length(t_S)); % battery voltage
410 SOC_curr = zeros(N_md, length(t_S)); % current state of charge of ...
411     the battery
412 thd = 0; % threshold counter for U_MPP
413
414 Δ_ip = -0.01;
415
416 SOC_ip = 1:Δ_ip:0; % interpolated state of charge of the battery
417 U_0_D_ip = interp1(SOC, U_0_D, SOC_ip); % interpolated open-circuit ...
418     voltage of the battery when discharging
419 U_0_C_ip = interp1(SOC, U_0_C, SOC_ip); % interpolated open-circuit ...
420     voltage of the battery when charging
421 R_e_D_ip = interp1(SOC, R_e_D, SOC_ip); % interpolated electrolyte ...
422     resistance of the battery when discharging
423 R_e_C_ip = interp1(SOC, R_e_C, SOC_ip); % interpolated electrolyte ...
424     resistance of the battery when charging
425
426 U_0 = (U_0_D_ip + U_0_C_ip) / 2; % mean open circuit voltage
427
428 for n = 1:N_md % SCC limits power
429     for o = 1:length(t_S)
430         if(P_MPP(n,o) > P_MPP_max)
431             P_MPP(n,o) = P_MPP_max;
432             I_MPP(n,o) = P_MPP(n,o) / U_MPP(n,o);
433         end
434     end
435 end
436
437 for n = 1:N_md % PV voltage at SCC input terminal after cable losses
438     for o = 1:length(t_S)
439         U_in(n,o) = U_MPP(n,o) - 2 * (R_wires(1) + R_wires(2)) * ...
440             I_MPP(n,o);
441     end
442 end
443
444 [~,idx_SOC] = min(abs(SOC_ip - SOC_init)); % find closest index
445
446 for n = 1:N_md % calculating SOC and voltage of the battery ...
447     (improve in version 1.1)
448     for o = 1:length(t_S)

```

```
441     if(n == 1 && o < idx_mission_se(n,1)) % mission on the ...
442         first day has not started yet
443         thd = -1;
444     elseif(n == 1 && o == idx_mission_se(n,1)) % if the mission ...
445         day starts at 0:00
446         if(U_in(n,o) > (U_0(idx_SOC) + 5) && (thd == 0 || thd ...
447             == -1)) % I_MPP on
448             thd = 1;
449         elseif(U_in(n,o) < (U_0(idx_SOC) + 1) && thd == 1) % ...
450             I_MPP off;
451             thd = 0;
452         end
453     else
454         if(o - 1 == 0) % if a new day started, get U_B from the ...
455             last time entry from the previous day
456             if(U_in(n,o) > (U_B(n - 1,length(t_S)) + 5) && (thd ...
457                 == 0 || thd == -1)) % I_MPP on
458                 thd = 1;
459             elseif(U_in(n,o) < (U_B(n - 1,length(t_S)) + 1) && ...
460                 thd == 1) % I_MPP off;
461                 thd = 0;
462             end
463         end
464     end
465     if(thd == 1) % PV generator is connected (improve in ...
466         version 1.1)
467         I_B(n,o) = I_SCC - I_MPP(n,o) * eta_SCC + I_L(n,o);
468     elseif(thd == 0) % PV generator is disconnected
469         I_B(n,o) = I_SCC + I_L(n,o);
470     elseif(thd == -1) % before the mission starts on the first day
471         I_B(n,o) = 0;
472     end
473     if(I_B(n,o) > I_B_max)
474         I_B(n,o) = I_B_max;
475     elseif(I_B(n,o) < - I_B_max)
476         I_B(n,o) = - I_B_max;
477     end
478     if(I_B(n,o) > 0) % battery is discharging
479         Q_tot = Q_nom * (I_nom / I_B(n,o))^(k_P - 1);
480
481     if(n > 1 && o == 1) % get SOC from the end of the ...
482         previous day
483         SOC_curr(n,o) = SOC_curr(n - 1, length(t_S)) - (1 / ...
484             Q_tot) * I_B(n,o) * Δ_t_S;
485     else % get previous state of charge
```

```

485         SOC_curr(n,o) = SOC_curr(n,o - 1) - (1 / Q_tot) * ...
486             I_B(n,o) * Δ_t_S;
487     end
488
489     if(SOC_curr(n,o) > 1)
490         SOC_curr(n,o) = 1;
491     elseif(SOC_curr(n,o) < 0)
492         SOC_curr(n,o) = 0;
493     end
494
495     [~,idx_SOC] = min(abs(SOC_ip - SOC_curr(n,o))); % find ...
496         closest index
497     c_B = abs(U_0_C_ip(idx_SOC) - U_0_D_ip(idx_SOC)) / 2;
498     U_B(n,o) = U_0(idx_SOC) - c_B - R_e_D_ip(idx_SOC) * ...
499         I_B(n,o);
500
501     elseif(I_B(n,o) < 0) % battery is charging
502         Q_tot = Q_nom;
503
504     if(n > 1 && o == 1) % get SOC from the end of the ...
505         previous day
506         SOC_curr(n,o) = SOC_curr(n - 1, length(t_S)) - 1 / ...
507             Q_tot * I_B(n,o) * Δ_t_S;
508     else % get previous state of charge
509         SOC_curr(n,o) = SOC_curr(n,o - 1) - 1 / Q_tot * ...
510             I_B(n,o) * Δ_t_S;
511     end
512
513     if(SOC_curr(n,o) > 1)
514         SOC_curr(n,o) = 1;
515     elseif(SOC_curr(n,o) < 0)
516         SOC_curr(n,o) = 0;
517     end
518
519     [~,idx_SOC] = min(abs(SOC_ip - SOC_curr(n,o))); % find ...
520         closest index
521     c_B = abs(U_0_C_ip(idx_SOC) - U_0_D_ip(idx_SOC)) / 2;
522     U_B(n,o) = U_0(idx_SOC) + c_B - R_e_C_ip(idx_SOC) * ...
523         I_B(n,o);
524
525     elseif(I_B(n,o) == 0) % battery is in standby (SOC_init ...
526         stays the same)
527     if(n == 1 && o == 1)
528         SOC_curr(n,o) = SOC_init;
529     elseif(n > 1 && o == 1) % get SOC from the end of the ...
530         previous day
531         SOC_curr(n,o) = SOC_curr(n - 1, length(t_S));
532     else % get previous state of charge
533         SOC_curr(n,o) = SOC_curr(n,o - 1);
534     end
535
536     if(SOC_curr(n,o) > 1)
537         SOC_curr(n,o) = 1;
538     elseif(SOC_curr(n,o) < 0)
539         SOC_curr(n,o) = 0;
540     end

```

```
532     [~,idx_SOC] = min(abs(SOC_ip - SOC_curr(n,o))); % find ...
      closest index
533     U_B(n,o) = U_0(idx_SOC);
534 end
535
536     U_L(n,o) = U_B(n,o) - 2 * R_wires(3) * I_B(n,o); % voltage ...
      at repeater after cable losses
537 if(U_L(n,o) < U_L_min)
      error('Voltage at repeater radio system is too low!');
538 elseif(U_L(n,o) > U_L_max)
      error('Voltage at repeater radio system is too high!');
539 end
540
541 end
542 end
543 end
544
545 if(min(min(SOC_curr)) == 0) % battery got fully discharged
546     error('LiFePO_4 battery gets fully discharged! Use more PV ...
      generators in parallel!');
547 end
548
549 %% [OUTPUT] Command window and plots
550
551 fnct_cw_output(show_command_window_output, N_md, gamma_S, alpha_S, ...
552     date_array, beta, t_S, W_G_el, SOC_curr); % command window output
553
554 diary off
```

C.2 MAPLE source code for the Jacobian matrix

[> **restart;**

PV generator model

In this MAPLE worksheet, the Jacobian matrix is applied to the PV generator model to calculate the first ten iterations of the open-circuit voltage $U_{OC}(\vartheta_C, \Phi_G)$ in (V) and the reverse saturation current $I_S(\vartheta_C)$. The calculations were performed for different values of the PV cell temperature ϑ_C and the irradiance E_G . However, in this printout $\vartheta_C = 25^\circ\text{C}$ and $E_G = 200 \text{ Wm}^{-2} \cdot \text{s}$

Header

[Used mathematical packages:

[> **with(LinearAlgebra):**

[> **with(VectorCalculus, Jacobian):**

Parameters

[Specifications of the PV generator (AE Solar AE195SMM6-36):

[> **param := [I_SC_STC = 9.79, U_OC_STC = 24.27, m = 1, N_C = 36,**
E_STC = 1000, E_G = 200, k_B = -1.380649 * 10^(-23), e =
1.602176634 * 10^(-19), vartheta_C = 25, vartheta_STC = 25,
TC_I_SC = 0.05, TC_U_OC = -0.29];
param := [I_{SC}_STC = 9.79, U_{OC}_STC = 24.27, m = 1, N_C = 36, E_{STC} = 1000, E_G = 200, k_B (2.1)
 $= 1.380649000 10^{-23}, e = 1.602176634 10^{-19}, \vartheta_C = 25, \vartheta_{STC} = 25, TC_{I_SC} = 0.05,$
 $TC_{U_OC} = -0.29]$

Main calculation

[First, the necessary quantities for the model of the PV generator and then the starting values for the Jacobian matrix are calculated. Based on these the Jacobian matrix is determined and transformed, so that it can be used with the Newton-Raphson method. Finally, the first then iterations of said method are determined.

Necessary quantities

[Thermal voltage:

[> **U_T := k_B * (vartheta_C + 273.15) / e;**
 $U_T := \frac{k_B (\vartheta_C + 273.15)}{e}$ (3.1.1)

[Photocurrent:

[> **I_Ph := I_SC_STC * E_G/E_STC * (1 + TC_I_SC/100 * (vartheta_C - vartheta_STC));**
 $I_{Ph} := \frac{I_{SC_STC} E_G}{E_{STC}} \left(1 + \frac{TC_{I_SC} (\vartheta_C - \vartheta_{STC})}{100} \right)$ (3.1.2)

[Photocurrent with constant solar irradiance ($E_G = E_{STC}$):

$$> I_{\text{Ph_const_irr}} := \text{eval}(I_{\text{Ph}}, E_{\text{G}} = E_{\text{STC}}); \\ I_{\text{Ph_const_irr}} := I_{\text{SC_STC}} \left(1 + \frac{TC_{I_SC} (\vartheta_C - \vartheta_{\text{STC}})}{100} \right) \quad (3.1.3)$$

Open-circuit voltage with constant solar irradiance ($E_G = E_{\text{STC}}$):

$$> U_{\text{OC_STC_const_irr}} := U_{\text{OC_STC}} * (1 + TC_{U_OC} / 100 * (\vartheta_C - \vartheta_{\text{STC}})); \\ U_{\text{OC_STC_const_irr}} := U_{\text{OC_STC}} \left(1 + \frac{TC_{U_OC} (\vartheta_C - \vartheta_{\text{STC}})}{100} \right) \quad (3.1.4)$$

Starting values for the jacobian matrix

Starting value for the open-circuit voltage:

$$> U_{\text{OC_0}} := \text{evalf}(\text{eval}(U_{\text{OC_STC_const_irr}} + m * N_{\text{C}} * U_{\text{T}} * \ln(E_{\text{G}}/E_{\text{STC}}), \text{param}));$$

Starting value for the reverse saturation current:

$$> I_{\text{S_0}} := \text{evalf}(\text{eval}(I_{\text{Ph}} * \exp(-U_{\text{OC_0}} / (m * N_{\text{C}} * U_{\text{T}})), \text{param}));$$

Jacobian matrix

Preparing the vector of functions and zero crossings for the Jacobian matrix:

$$\begin{aligned} &> f_1 := \exp((U_{\text{OC_theta_phi}} - U_{\text{OC_STC_const_irr}})/(m * N_{\text{C}} * U_{\text{T}})) - (I_{\text{Ph}} - I_{\text{S_theta}})/(I_{\text{Ph_const_irr}} - I_{\text{S_theta}}) \\ &\quad : \\ &> f_2 := I_{\text{S_theta}} - I_{\text{Ph}} * (\exp(U_{\text{OC_theta_phi}}/(m * N_{\text{C}} * U_{\text{T}})) - 1)^{-1}; \\ &> f := \langle f_1, f_2 \rangle; \\ &> x_{\text{R}} := \langle I_{\text{S_theta}}, U_{\text{OC_theta_phi}} \rangle; \end{aligned}$$

Calculating the Jacobian matrix:

$$> J := \text{Jacobian}(\text{convert}(f, \text{list}), \text{convert}(x_{\text{R}}, \text{list}));$$

Preparing the Jacobian matrix for the Newton-Raphson method:

$$\begin{aligned} &> J_{\text{inv}} := \text{MatrixInverse}(J); \\ &> J_{\text{inv_num}} := \text{eval}(J_{\text{inv}}, \text{param}); \\ &> f_{\text{num}} := \text{eval}(f, \text{param}); \end{aligned}$$

Iterations (Newton-Raphson method)

$$> x_{\text{R_0}} := \langle I_{\text{S_0}}, U_{\text{OC_0}} \rangle; \\ x_{\text{R_0}} := \begin{bmatrix} 3.935566032 \cdot 10^{-11} \\ 22.78137801 \end{bmatrix} \quad (3.4.1)$$

$$\begin{aligned} &> x_{\text{R_1}} := \text{evalf}(x_{\text{R_0}} - \text{eval}(J_{\text{inv_num}} . f_{\text{num}}, [I_{\text{S_theta}} \\ &\quad = x_{\text{R_0}}(1), U_{\text{OC_theta_phi}} = x_{\text{R_0}}(2)])); \\ &\quad x_{\text{R_1}} := \begin{bmatrix} 3.93556604183892 \cdot 10^{-11} \\ 22.7813780076877 \end{bmatrix} \quad (3.4.2) \end{aligned}$$

$$\begin{aligned} &> x_{\text{R_2}} := \text{evalf}(x_{\text{R_1}} - \text{eval}(J_{\text{inv_num}} . f_{\text{num}}, [I_{\text{S_theta}} \\ &\quad = x_{\text{R_1}}(1), U_{\text{OC_theta_phi}} = x_{\text{R_1}}(2)])); \\ &\quad (3.4.3) \end{aligned}$$

$$x_{R_2} := \begin{bmatrix} 3.93556604183619 \cdot 10^{-11} \\ 22.7813780046823 \end{bmatrix} \quad (3.4.3)$$

$$> x_{R_3} := \text{evalf}(x_{R_2} - \text{eval}(J_{\text{inv_num}} \cdot f_{\text{num}}, [I_S_{\text{theta}} = x_{R_2}(1), U_{OC_{\text{theta_phi}}} = x_{R_2}(2)]));$$

$$x_{R_3} := \begin{bmatrix} 3.93556604183619 \cdot 10^{-11} \\ 22.7813780046823 \end{bmatrix} \quad (3.4.4)$$

$$> x_{R_4} := \text{evalf}(x_{R_3} - \text{eval}(J_{\text{inv_num}} \cdot f_{\text{num}}, [I_S_{\text{theta}} = x_{R_3}(1), U_{OC_{\text{theta_phi}}} = x_{R_3}(2)]));$$

$$x_{R_4} := \begin{bmatrix} 3.93556604183619 \cdot 10^{-11} \\ 22.7813780046823 \end{bmatrix} \quad (3.4.5)$$

$$> x_{R_5} := \text{evalf}(x_{R_4} - \text{eval}(J_{\text{inv_num}} \cdot f_{\text{num}}, [I_S_{\text{theta}} = x_{R_4}(1), U_{OC_{\text{theta_phi}}} = x_{R_4}(2)]));$$

$$x_{R_5} := \begin{bmatrix} 3.93556604183619 \cdot 10^{-11} \\ 22.7813780046823 \end{bmatrix} \quad (3.4.6)$$

$$> x_{R_6} := \text{evalf}(x_{R_5} - \text{eval}(J_{\text{inv_num}} \cdot f_{\text{num}}, [I_S_{\text{theta}} = x_{R_5}(1), U_{OC_{\text{theta_phi}}} = x_{R_5}(2)]));$$

$$x_{R_6} := \begin{bmatrix} 3.93556604183619 \cdot 10^{-11} \\ 22.7813780046823 \end{bmatrix} \quad (3.4.7)$$

$$> x_{R_7} := \text{evalf}(x_{R_6} - \text{eval}(J_{\text{inv_num}} \cdot f_{\text{num}}, [I_S_{\text{theta}} = x_{R_6}(1), U_{OC_{\text{theta_phi}}} = x_{R_6}(2)]));$$

$$x_{R_7} := \begin{bmatrix} 3.93556604183619 \cdot 10^{-11} \\ 22.7813780046823 \end{bmatrix} \quad (3.4.8)$$

$$> x_{R_8} := \text{evalf}(x_{R_7} - \text{eval}(J_{\text{inv_num}} \cdot f_{\text{num}}, [I_S_{\text{theta}} = x_{R_7}(1), U_{OC_{\text{theta_phi}}} = x_{R_7}(2)]));$$

$$x_{R_8} := \begin{bmatrix} 3.93556604183619 \cdot 10^{-11} \\ 22.7813780046823 \end{bmatrix} \quad (3.4.9)$$

$$> x_{R_9} := \text{evalf}(x_{R_8} - \text{eval}(J_{\text{inv_num}} \cdot f_{\text{num}}, [I_S_{\text{theta}} = x_{R_8}(1), U_{OC_{\text{theta_phi}}} = x_{R_8}(2)]));$$

$$x_{R_9} := \begin{bmatrix} 3.93556604183619 \cdot 10^{-11} \\ 22.7813780046823 \end{bmatrix} \quad (3.4.10)$$

$$> x_{R_10} := \text{evalf}(x_{R_9} - \text{eval}(J_{\text{inv_num}} \cdot f_{\text{num}}, [I_S_{\text{theta}} = x_{R_9}(1), U_{OC_{\text{theta_phi}}} = x_{R_9}(2)]));$$

$$x_{R_10} := \begin{bmatrix} 3.93556604183619 \cdot 10^{-11} \\ 22.7813780046823 \end{bmatrix} \quad (3.4.11)$$

References

- [1] A. Christian, W. Jungbauer, H. Kähler, *et al.*, *Biologie Heute SII*. Braunschweig, Germany: Bildungshaus Schulbuchverlage Westermann Schroedel Diesterweg Schöningh Winklers GmbH, Braunschweig, 2004, vol. Druck A7 / Jahr 2011.
- [2] I. A. Glover and P. M. Grant, *Digital Communications*, 3rd ed. Essex, England: Prentice Education Limited, 2010.
- [3] G. Groemer, *Aouda system handbook*, V4.7.5, Austrian Space Forum, Mar. 2020.
- [4] K. Lange and K.-H. Löcherer, Eds., *Taschenbuch der Hochfrequenztechnik*. New York: Springer-Verlag Berlin Heidelberg, 1992, vol. 2.
- [5] J. D. Parsons, *The mobile Radio Propagation Channel*, 2nd ed. Sussex, England: John wiley & Sons, Ltd, 2000.
- [6] A. M. J. Goiser, *Telekommunikation*, V 1.1b. Vienna, Austria: Institute of Telecommunications, 2019.
- [7] C. Mecklenbräuker, *Wellenausbreitung*, 14th ed. Vienna, Austria: Institute for Telecommunications, 2017.
- [8] *The link budget and fade margin*, Campbell Scientific Inc., Sep. 2016.
- [9] E. Rebhan, Ed., *Energiehandbuch*. New York: Springer-Verlag Berlin Heidelberg, 2002.
- [10] W. Gawlik, *Energieversorgung*. Vienna, Austria: Institut of Energy Systems and Electrical Drivers, 2018.
- [11] K. Mertens, *Photovoltaik*, 3rd ed. Munich: Carl Hanser Verlag, 2015.
- [12] E. Hau, *Windkraftanlagen*, 6th ed. Berlin: Springer-Verlag GmbH Deutschland, 2016.
- [13] A. Wagner, *Photovoltaik Engineering*, 5th ed. Berlin: Springer-Verlag GmbH Deutschland, 2018.
- [14] M. Sterner and I. Stadler, Eds., *Energiespeicher*, 2nd ed. Berlin: Springer-Verlag GmbH Deutschland, 2017.
- [15] P. Kurzweil and O. K. Dietlmeier, *Elektrochemische Speicher*, 2, Ed. Wiesbaden, Germany: Springer Fachmedien Wiesbaden GmbH, 2018.
- [16] J. Appelbaum and D. J. Flood, “Solar radiation on mars,” *NASA Technical Memorandum*, no. 102299, pp. 1–31, 1989.
- [17] J. Appelbaum and G. Landis, “Photovoltaic array for martian surface power,” *NASA Technical Memorandum*, no. 105827, pp. 1–21, Aug. 1992.

- [18] J. Appelbaum, I. Sherman, and G. Landis, “Solar radiation on mars: Stationary photovoltaic array,” *NASA Technical Memorandum*, no. 106321, pp. 1–19, 1993.
- [19] C. Ho, N. Golshan, and A. Kliore, “Radio wave propagation handbook for communication on and around mars,” *NASA Jet Propulsion Laboratory California Institute of Technology*, vol. JPL Publication 02-5, Mar. 2002.
- [20] N. Bertol, *Photovoltaic Systems*. Saarbrücken, Germany: VDM Verlag Dr. Müller GmbH and Co. KG, 2011.
- [21] R. Flosdorff and G. Hilgarth, *Elektrische Energieverteilung*, 9th ed. Wiesbaden, Germany: Vieweg+Teubner Verlag | GWV Fachverlag GmbH, 2008.
- [22] Global Wind Atlas, *Global wind atlas*, 2021. [Online]. Available: <https://globalwindatlas.info/area/India> (visited on 04/13/2021).
- [23] D. R. Williams, *Mars fact sheet*, Nov. 2020. [Online]. Available: <https://nssdc.gsfc.nasa.gov/planetary/factsheet/marsfact.html> (visited on 04/13/2021).
- [24] ——, *Earth fact sheet*, Nov. 2020. [Online]. Available: <https://nssdc.gsfc.nasa.gov/planetary/factsheet/earthfact.html> (visited on 04/13/2021).
- [25] H. Karttunen, P. Kröger, H. Oja, et al., Eds., *Fundamental Astronomy*, 5th ed. New York: Springer-Verlag Berlin Heidelberg, 2007.
- [26] W. Ley, K. Wittmann, and W. Hallmann, Eds., *Handbuch der Raumfahrttechnik*, 4th ed. Munich: Carl Hanser Verlag, 2011.
- [27] Solargis, *Solar resource maps and gis data for 200+ countries*, 2021. [Online]. Available: <https://solargis.com/maps-and-gis-data/overview> (visited on 04/13/2021).
- [28] Global Solar Atlas, *Global solar atlas*, 2021. [Online]. Available: <https://globalsolaratlas.info/map> (visited on 04/13/2021).
- [29] European Comission, *Photovoltaic geographical information system (pvgis)*, Mar. 2021. [Online]. Available: <https://ec.europa.eu/jrc/en/pvgis> (visited on 04/13/2021).
- [30] M. H. Babikir, D. Njomo, M. Barka, et al., “Modeling the incident solar radiation of the city of n’djamena (chad) by the capderou method,” *International Journal of Photoenergy*, vol. 2020, pp. 1–10, 2020.
- [31] Solargis, *Meteorological models and post-processing*, 2021. [Online]. Available: <https://solargis.com/docs/methodology/meteo-data> (visited on 04/13/2021).
- [32] ——, *Methodology - solar radiation modeling*, 2021. [Online]. Available: <https://solargis.com/docs/methodology/solar-radiation-modeling> (visited on 04/13/2021).
- [33] ——, *Solar data behind the maps*, 2021. [Online]. Available: <https://solargis.com/maps-and-gis-data/tech-specs> (visited on 04/13/2021).
- [34] ——, *Weather data and software for solar power investments*, 2021. [Online]. Available: <https://solargis.com/> (visited on 04/13/2021).

- [35] J. Bennett, M. Donahue, N. Schneider, *et al.*, *Astronomie*, 5th ed., H. Lesch, Ed. Hallbergmoos, Germany: Pearson Deutschland GmbH, 2010.
- [36] T. Bralower and D. Bice, *Albedo*. [Online]. Available: <https://www.e-education.psu.edu/earth103/node/1002> (visited on 04/13/2021).
- [37] E. Dobos, “Albedo,” *Encyclopedia of Soil Science, Second Edition*, pp. 3–5, 2011.
- [38] A. Karafil, H. Ozbay, M. Kesler, *et al.*, “Calculation of optimum fixed tilt angle of pv panels depending on solar angles and comparison of the results with experimental study conducted in summer in bilecik, turkey,” *ELECO 2015 - 9th International Conference on Electrical and Electronics Engineering*, pp. 971–976, 2016.
- [39] A. Prechtel, *Vorlesungen über die Grundlagen der Elektrotechnik*, 2nd ed. Vienna, Austria: Springer-Verlag, 2006, vol. 1.
- [40] ———, *Vorlesungen über die Grundlagen der Elektrotechnik*, 2nd ed. Vienna, Austria: Springer-Verlag, 2008, vol. 2.
- [41] E. Schrüfer, L. Reindl, and B. Zagar, *Elektrische Messtechnik*, 11th ed. Munich: Carl Hanser Verlag, 2014.
- [42] I. Al-Nahhal, O. A. Dobre, E. Basar, *et al.*, “A fast, accurate, and separable method for fitting a gaussian function,” *IEEE Signal Processing Magazine*, vol. 36, p. 157, 2019.
- [43] Z. Guo, “Daily variation law of solar radiation flux density incident on the horizontal surface,” *Journal of Astrophysics & Aerospace Technology*, vol. 8, pp. 10–14, 2017.
- [44] D. P. N. Nguyen and J. Lauwaert, “Calculating the energy yield of si-based solar cells for belgium and vietnam regions at arbitrary tilt and orientation under actual weather conditions,” *Energies*, vol. 13, pp. 1–17, Jun. 2020.
- [45] C. Balafas, M. Athanassopoulou, T. Argyropoulos, *et al.*, “Effect of the diffuse solar radiation on photovoltaic inverter output,” *Proceedings of the Mediterranean Electrotechnical Conference - MELECON*, pp. 58–63, 2010.
- [46] G. Koudouris, P. Dimitriadis, T. Iliopoulos, *et al.*, “Investigation on the stochastic nature of the solar radiation process,” *Energy Procedia*, vol. 125, pp. 398–404, 2017.
- [47] U. Tietze, C. Schenk, and E. Gamm, *Halbleiter Schaltungstechnik*, 15th ed. New York: Springer-Verlag Berlin Heidelberg, 2016.
- [48] G. Elert, *Physical constants*, 2021. [Online]. Available: <https://physics.info/constants/> (visited on 04/13/2021).
- [49] E. Hering, K. Bressler, and J. Gutekunst, Eds., *Elektronik für Ingenieure und Naturwissenschaftler*, 7th ed. Berlin: Springer-Verlag GmbH Deutschland, 2017.
- [50] H. R. Schwarz and N. Köckler, *Numerische Mathematik*, 8th ed. Wiesbaden, Germany: Vieweg+Teubner Verlag | Springer Fachmedien Wiesbade GmbH, 2011.

- [51] R. Taschner, *Anwendungsorientierte Mathematik für ingenieurwissenschaftliche Fachrichtungen*. Munich: Carl Hanser Verlag, 2014, vol. 2.
- [52] ——, *Anwendungsorientierte Mathematik für ingenieurwissenschaftliche Fachrichtungen*. Munich: Carl Hanser Verlag, 2014, vol. 1.
- [53] A. Kugi, *Automatisierung*. Vienna, Austria: Institut fuer Automatisierungs- und Regelungstechnik, TU Wien, 2021.
- [54] L. Zepner, P. Karrash, F. Wiemann, et al., *An interactive climate analysis web platform*, 2020. [Online]. Available: <https://climatecharts.net/> (visited on 04/13/2021).
- [55] A. Hausmann and C. Depcik, “Expanding the peukert equation for battery capacity modeling through inclusion of a temperature dependency,” *Journal of Power Sources*, vol. 235, pp. 148–158, 2013.
- [56] J. Wehbe and N. Karami, “Battery equivalent circuits and brief summary of components value determination of lithium ion: A review,” *2015 3rd International Conference on Technological Advances in Electrical, Electronics and Computer Engineering, TAECEC 2015*, pp. 45–49, 2015.
- [57] A. A. Hussein, “Experimental modeling and analysis of lithium-ion battery temperature dependence,” *Conference Proceedings - IEEE Applied Power Electronics Conference and Exposition - APEC*, vol. 2015-May, 2015.
- [58] S. Nejad, D. T. Gladwin, and D. A. Stone, “A systematic review of lumped-parameter equivalent circuit models for real-time estimation of lithium-ion battery states,” *Journal of Power Sources*, vol. 316, pp. 183–196, 2016.
- [59] C. S. Chin, Z. Gao, J. H. K. Chiew, et al., “Nonlinear temperature-dependent state model of cylindrical lifepo4 battery for open-circuit voltage, terminal voltage and state-of-charge estimation with extended kalman filter,” *Energies*, vol. 11, pp. 1–28, 2018.
- [60] J. Li, F. Gao, G. Yan, et al., “Modeling and soc estimation of lithium iron phosphate battery considering capacity loss,” *Protection and Control of Modern Power Systems*, vol. 3, pp. 3–11, 2018.
- [61] H. Hinz, “Comparison of lithium-ion battery models for simulating storage systems in distributed power generation,” *Inventions*, vol. 4, pp. 1–22, 2019.
- [62] M. Hossain, S. Saha, M. E. Haque, et al., “A parameter extraction method for the thevenin equivalent circuit model of li-ion batteries,” *2019 IEEE Industry Applications Society Annual Meeting, IAS 2019*, pp. 1–7, 2019.
- [63] Offgridtec smart-pro 12,8v 50ah/100ah/150ah/200ah, Offgridtec GmbH, 2020.
- [64] H. He, R. Xiong, and J. Fan, “Evaluation of lithium-ion battery equivalent circuit models for state of charge estimation by an experimental approach,” *Energies*, vol. 4, pp. 582–598, 2011.
- [65] A. Hentunen, T. Lehmuspelto, and J. Suomela, “Time-domain parameter extraction method for thévenin-equivalent circuit battery models,” *IEEE Transactions on Energy Conversion*, vol. 29, pp. 558–566, 2014.

- [66] L. Gurjer, P. Chaudhary, and H. K. Verma, "Detailed modelling procedure for lithium-ion battery using thevenin equivalent," *Proceedings of 2019 3rd IEEE International Conference on Electrical, Computer and Communication Technologies, ICECCT 2019*, pp. 1–5, 2019.
- [67] G. Saldaña, J. I. S. Martín, I. Zamora, et al., "Analysis of the current electric battery models for electric vehicle simulation," *Energies*, vol. 12, pp. 1–27, 2019.
- [68] K. Thirugnanam, E. R. J. T. P., M. Singh, et al., "Mathematical modeling of li-ion battery using genetic algorithm approach for v2g applications," *IEEE Transactions on Energy Conversion*, vol. 29, pp. 332–343, 2014.
- [69] A. Rahmoun and H. Biechl, "Modelling of li-ion batteries using equivalent circuit diagrams," *Przeglad Elektrotechniczny (Electrical Review)*, vol. 88, pp. 152–156, 2012.
- [70] P. Notten, J. O. het Veld, and J. van Beck, "Boostcharging li-ion batteries: A challenging new charging concept," *Journal of Power Sources*, vol. 145, pp. 89–94, 2005.
- [71] H. Liu, I. H. Naqiv, F. Li, et al., "An analytical model for the cc-cv charge of li-ion batteries with application to degradation analysis," *Journal of Energy Storage*, vol. 29, pp. 1–11, 2020.
- [72] G. Fasching, *Werkstoffe für die Elektrotechnik*, 4th ed. Vienna, Austria: Springer-Verlag, 2005.
- [73] W. Kemmetmüller and A. Kugi, *Modellbildung*. Vienna, Austria: Institut fuer Automatisierungs- und Regelungstechnik, TU Wien, 2021.
- [74] Mototrbo system planner, System Release 2.9.5, Motorola Solutions Inc., 2018.
- [75] Mototrbo dm 2600, EMEA version 1, Motorola Solutions Inc., Aug. 2013.
- [76] Mototrbo slr 1000, EMEA version 2, Motorola Solutions Inc., Mar. 2019.
- [77] Instruction manual cross needle swr & power meter cn-501 series, No.201606, Daiwa industry co. Ltd., Jun. 2016.
- [78] R. P. Company, *Sp1000 lightning arrester*, 2020. [Online]. Available: <https://www.diamondantenna.net/sp1000.html> (visited on 04/13/2021).
- [79] Diamond Antenna Corp., *V/uhf fixed station antenna*. [Online]. Available: http://www.diamond-ant.co.jp/english/commercial/com_3fix.html (visited on 04/13/2021).
- [80] *M & p ultraflexflex 7*, Messi & Paoloni, 2021.
- [81] Mototrbo sl 2600, EMEA version 1, Motorola Solutions Inc., Sep. 2017.
- [82] G. Hinker, *Excerpt of the NASA STD-3000 Standard*, V1.0. Innsbruck, Austria: OeWF, Aug. 2007.
- [83] *Push switch r13-527a2-02*, C8\R13\R13-527A-02(1830627)_1, Shin Chin Industrial Co., Ltd., May 2011.
- [84] *Ep900w*, 02-2021, Motorola Solutions Inc., Feb. 2021.
- [85] National Aeronautics and Space Administration, *3 anthropometry and biomechanics*, Aug. 2020. [Online]. Available: <https://msis.jsc.nasa.gov/sections/section03.htm> (visited on 04/13/2021).

- [86] *Mototrbo dp 3600/dp 3601/dp 3400/dp 3401*, AC3-04-029, Motorola Solutions Inc., Apr. 2010.
- [87] *Ae smart hot-spot free monocrystalline pv modules ae m6-36 series 180w-195w*, AES-DSH2019 V.002, AE Solar GmbH, 2019.
- [88] *Lightweight flexible photovoltaic module*, 11/2017/EN/DAS Energy GmbH, DAS Energy GmbH, Nov. 2017.
- [89] *Enc programmable smart charger instruction manual*, 1JJ8ENC-R2, Mean Well.
- [90] *Bluesolar charge controllers mppt 75/10, 75/15, 100/15*, 5th ed., Victron Energy B.V., Jul. 2018.
- [91] Austrian Space Forum, *Once upon a time...* 2021. [Online]. Available: <https://oewf.org/en/about-the-oewf/history/> (visited on 04/13/2021).
- [92] E. Salas, W. Abbey, R. Bhartia, et al., “The mojave desert: A martian analog site for future astrobiology themed missions.” pp. 1–3, 2011.
- [93] L. Preston, M. Grady, and S. Barber, “Cafe concepts for activities in the field for exploration,” *The Open University*, vol. Final Version, pp. 1–170, 2012.
- [94] L. J. Preston and L. R. Dartell, “Planetary habitability: Lessons learned from terrestrial analogues,” *International Journal of Astrobiology*, vol. 13, pp. 81–98, 2014.
- [95] National Aeronautics and Space Administration, *Rock spire in 'spirit of st. louis crater' on mars*, Aug. 2017. [Online]. Available: <https://www.nasa.gov/jpl/mer/pia19393/rock-spire-in-spirit-of-st-louis-crater-on-mars> (visited on 04/13/2021).
- [96] Austrian Space Forum, *Portfolio category “field simulations/expeditions”*, 2021. [Online]. Available: <https://oewf.org/en/portfolioCat/field-simulations-expeditions/> (visited on 04/13/2021).
- [97] ——, *Austrian space forum postpones mars analog mission by one year to october 2021*, Aug. 2020. [Online]. Available: <https://oewf.org/en/2020/08/countdown-for-mars-simulation-halted/> (visited on 04/13/2021).
- [98] NASA’s Open Data Portal, *Eva suitport*, Jan. 2021. [Online]. Available: <https://data.nasa.gov/dataset/EVA-Suitport/ivcm-2xim> (visited on 04/13/2021).
- [99] R. Taschner, *Anwendungsorientierte Mathematik für ingenieurwissenschaftliche Fachrichtungen*. Munich: Carl Hanser Verlag, 2015, vol. 3.